Developmental Dynamics of the Mouse Retinocollicular Projection
A Quantitative Characterisation

Lyngholm, Daniel

Awarding institution:
King's College London

Title: Developmental Dynamics of the Mouse Retinocollicular Projection

A Quantitative Characterisation

Author: Daniel Lyngholm

Developmental Dynamics of the Mouse Retinocollicular Projection

A Quantitative Characterisation

Thesis for the Degree of
Doctor of Philosophy

By:
Daniel Lyngholm

Supervisors:
Prof. Ian D. Thompson (Primary Supervisor)
Dr. Robert Hindges (Secondary Supervisor)

Submitted: **September 2012**

Pages: **195** Words: **41,106**

KING'S College LONDON

MRC Centre for Developmental Neurobiology,
King's College London,
London, UK

Table of Contents:

Figures:

Tables

Equations

Abstract

Development of retinotopy is an area of longstanding investigation, and it is clear that this development is influenced by both molecular and activity-based cues. The interaction between these different cues, however, is unclear: conventionally molecular guidance cues set the basic topography, which is then refined by activity-based mechanisms. A number of computational models have investigated this interaction. However, due to the limited availability of quantitative data it has not been possible to test whether the models can account for the precise developmental sequence of retinotopic map formation. This thesis provides such quantitative anatomical data about the spatiotemporal sequence of development of precision in the retinocollicular projection in the mouse. This characterisation has been done by utilising retrograde transport of fluorescent microspheres administered by discrete injections into the SC and recovered from retinal flat-mounts. To enable quantification of topographic precision, retinae are standardised using an algorithm that permits retinal outlines to be stitched back together into a sphere and cell locations plotted in spherical coordinates, which enables mapping across multiple animals and facilitates comparison between different age-points, genotypes and potentially different species.

The anatomical description reveals the precise dynamics of retinocollicular projection refinement, as projection refines from having almost no precision along the SC AP axis at birth to having topographically accurate, albeit imprecise, but symmetrical precision by the end of the first postnatal week. The data, moreover, reveals that the period of refinement extends significant beyond the first postnatal week and refinement is even seen after the third postnatal week. It is also found that the early refinement is crucially dependent on specific patterns of spontaneous retinal activity, since altering the activity-patterns by removing the nAChR-β2 subunit completely disrupts the refinement normally seen in the first postnatal week. Furthermore, it is found that refinement does occur in these animals after the first postnatal week, but it does not rescue the phenotype.

Keywords


retina
projection
label
development
retinal
visual
cells
SC
injections
using
contour
waves
axis
RGCs
projections
Equation
nAChR-β2
analysis
activity
animals
isodensity
injection
contours
also
different
size
refinement
mouse
data
nearest
retinae
retinocollicular
axons
AP
P0
P8
P6
P4
P2
P12
P22
order
plotted
However
adult
sites
area
across
cortex
Neuron
maps
mechanisms
entire
fitted
guidance
spontaneous
meridian
mice
curves
value
fits
distribution
significant
inflection
changes
Karcher
ages
difference
line
red
period
plot
labelled
separated
separation
precision
optic
Development
coordinates
central
space
birth
result
type
map
orientation
although
cell
role
segregated
P22
neighbour
function
along
possible
density
system
Dräger
colliculus
axon
angle
age
model
ganglion
knockout
mean
anatomical
blue
point
topographic
fit
studies
patterns
RGC
field
wild
location
may
slope
green
topography
similar
eye
ML
plots
superior
used
less
segregation
example
Yellow

Acknowledgements

Firstly, I would like to thank my supervisor Ian Thompson for taking me on as a naïve undergraduate and guiding me into the field of visual system neuroscience, while keeping me firmly grounded in anatomy. Thanks to Marcus Leiwe for all the discussions and to Andrew Lowe for persistently and quietly being encouraging, sarcastic and critical about everything. I'm also grateful especially to the Burrone, Meyer, Andreae, Grubb and Keck labs for creating a great atmosphere in which to do a PhD.

Special thanks should go to David Sterratt (University of Edinburgh), firstly for putting up with all my questions, but mostly for giving considerable computational assistance with the analysis by creating the retinal folding algorithms (Sterratt et al., n.d.) and helping with the associated analysis (especially the isodensity contour analysis). Likewise, Johannes Hjorth (University of Cambridge) has provided invaluable advise on the limits and possibilities of developmental modelling and assisted by creating a modelling framework to compare and extend the scope and understanding derived from the studies in this thesis. Thanks also to Uwe Drescher and Kate Marler (King's College London) for providing mouse lines and advised on molecular biology techniques.

Lest but certainly nae leest, cheers tae looise fur bein' understandin' an' supportin' me while writin' an' in general. nae sure hoo Ah woods hae coped withit th' backgroond twitterings. Finally, to the dog that is currently sitting on my lap where she's been for the past months when she's not been throwing balls at me in annoyance that I'm just looking at that stupid screen instead of playing: *"ned!"*

Funding Sources:

During this work, I have been funded by a studentship from the Medical Research Council (UK). The work was made possible by a programme grant from the Wellcome Trust (G083305) to Ian Thompson, Uwe Drescher, David Willshaw & Stephen Eglen.

Abbreviations

SC	Superior Colliculus
dLGN	dorsal Lateral Geniculate Nucleus
SO	Stratum Opticum
SGZ	Stratum Griseum Zonale
OD	Optic Disc
OA	Optic Axis
KDE	Kernel Density Estimate
KRE	Kernel Regression Estimate
NN	Nearest Neighbour
SSE	Sum of Squared Errors
SD	Standard Deviation
SEM	Standard Error of the Mean
nAChR	nicotinic acetylcholine receptor
Eph	Erythropoietin-Producing human Hepatocellular carcinoma Protein
ephrin	Eph family Receptor Interacting Proteins
NT	Nasal-Temporal
AP	Anterior-Posterior
DV	Dorsal-Ventral
ML	Medial-Lateral
E0	Embryonic day 0
P0	Postnatal day 0

Chapter 1 Introduction

The vertebrate visual system is a highly organised structure that allows the spatiotemporal changes of light intensities on the photoreceptors to be perceived as moving interacting three-dimensional images. Underlying this processing is the retinotopic projections to sub-cortical and cortical structures. But how do the retinotopic mappings interact to form connectivity with multiple levels of parallel connectivity, such as ocularity, multiple retinal ganglion cell classes and cortical orientation maps? These are big questions that all assume we understand the basic rules governing retinotopic map formation.

The development of this system long perplexed science and experiments of rotating the frog eye and studying the altered behaviour suggested that there may be intrinsic mechanisms involved in the formation of such circuits (Sperry, 1943). With the advent of tracing techniques, Sperry could finally show in 1963 that the axons projected to the appropriate location in the tectum even when the eye was rotated (Sperry, 1963). Sperry proposed that intrinsic guidance cues are essential for the guidance of retinal axons to their correct targets to form topographic maps (Sperry, 1963). This was accompanied by the discovery that in the cat dLGN, extrinsic visual experience could play a role in developing the different pathways of visual processing in cortex (Wiesel and Hubel, 1963). Combined with the hypothesis that neighbouring retinal cells will be more co-active (Willshaw and Malsburg, 1976) and therefore be more likely to connect to the same target (Hebb, 1949). Interestingly, it was later shown that transplanted axolotl RGCs that were silenced by endogenous tetrodotoxin in the newt could still form appropriate projections, even in the presence of competing active endogenous axons (Harris, 1980). However, when tetrodotoxin was used to silence activity in one eye of the cat, it prevented the formation of cortical ocular dominance columns (Stryker and Harris, 1986) and prevented the refinement of inputs in the hamster SC (Thompson and Holt, 1989). Taken together, these studies suggested that the initial guidance was dependent on intrinsic molecular cues, whereas the subsequent refinement was activity-

dependent. These observations and models have formed the basis for much of our understanding of the development of neural circuits.

Topography has been studied using a variety of techniques, but the majority of early studies mapping the inputs from the retina to its central targets were done by inserting electrodes into the structures and mapping the responses to visual stimuli, usually bars of varying size and orientation or spots of light in different positions of visual space. These studies were looking at postsynaptic responses in cortex (Hubel and Wiesel, 1963; Dräger, 1975), dLGN (Wiesel and Hubel, 1963) and SC (Dräger and Hubel, 1976). In addition to the physiological studies of the adult, the development of the retinal projection was also characterised anatomically by looking initially at the entire projection by filling the eye or target with tracer (Bunt et al., 1983; Thompson and Holt, 1989). Later studies looked at the topographic organisation of the projection by doing focal injections of tracer into the retina (Nakamura and O'Leary, 1989; Simon and O'Leary, 1992). Only a handful of studies have used focal retrograde tracing as the main method for investigating the development of the retinocollicular projection (Upton et al., 2007).

This section of the introduction focuses on the organisation and development of the mammalian retinofugal projection, especially that of the rodent. It starts by describing the mature visual system, focussing on the retinal projections to the image-forming circuits and in particular the role of the superior colliculus. Next it discusses methods for studying topography and precision in these projections, before moving on to introduce some of the mechanisms involved in the development of topographic precision in subcortical visual projections, namely the interplay of molecular guidance and activity. The intention is to follow a similar path as the results and thereby set the scene for the results.

1.1 Mature visual system

The mammalian visual system handles a profusion of tasks that are key to the behaving animal. Besides the image-forming circuits in the visual cortex and Superior Colliculus, the visual system also incorporates circuits that regulate circadian rhythms and reflexes.

1.1.1 Retinorecipient areas

The main primary retinal targets traditionally each have distinct functionality and are responsible for interpreting different aspects of visual stimuli. For this reason, many of them receive input from distinct populations of RGCs (Rodieck, 1979). The targets of the RGCs are largely conserved across most species. These targets comprise: 1) the dorsal Lateral Geniculate Nucleus of the thalamus (dLGN); 2) the Optic Tectum (OT) or Superior Colliculus (SC); 3) the Accessory Optic Nuclei (AON); 4) the ventral Lateral Geniculate Nucleus of the thalamus (vLGN); 5) the pretectum; 6) the Suprachiasmatic Nucleus of the hypothalamus (SCN); (Rodieck, 1979)

The dLGN (1) transmits information to primary visual cortex for processing of visual input and communication with higher cortical areas for conscious perception of visual stimuli. (Van Essen, 1979; Nicol et al., 2007). The SC (2) is key for coordinating motion in response to visual stimuli, while maintaining eye-gaze (Gandhi and Katnani, 2011). The AON (3) prefers slow movement and is involved in coordinating head and eye-movements to maintain gaze. The vLGN (4) is involved in circadian rhythms. The pretectum (5) controls optokinetic nystagmus and pupil dilation in response to light-changes (Rodieck, 1979). The SN (6) is involved in entrainment of circadian rhythms. As a result of their roles in regulating light-sensitive aspects of behaviour, the latter 3 all receive projections from intrinsically light-sensitive melanopsin-expressing RGCs (Ecker et al., 2010).

The projections can be divided roughly into image-forming (1-3) and non-image-forming areas (4-6). The projections from the retina to the image-forming areas in the mouse are illustrated in Figure 1-1. In rodents the vast majority of RGCs project to the superior colliculus with a proportion of them also branching into the dLGN (Perry et al., 1983). From the dLGN, the projection to primary visual cortex to convey information for further cortical processing. Additionally, there is also a projection from V1 to the SC (Thong and Dreher, 1986). These interconnections of the image-forming circuits are illustrated in Figure 1-1.

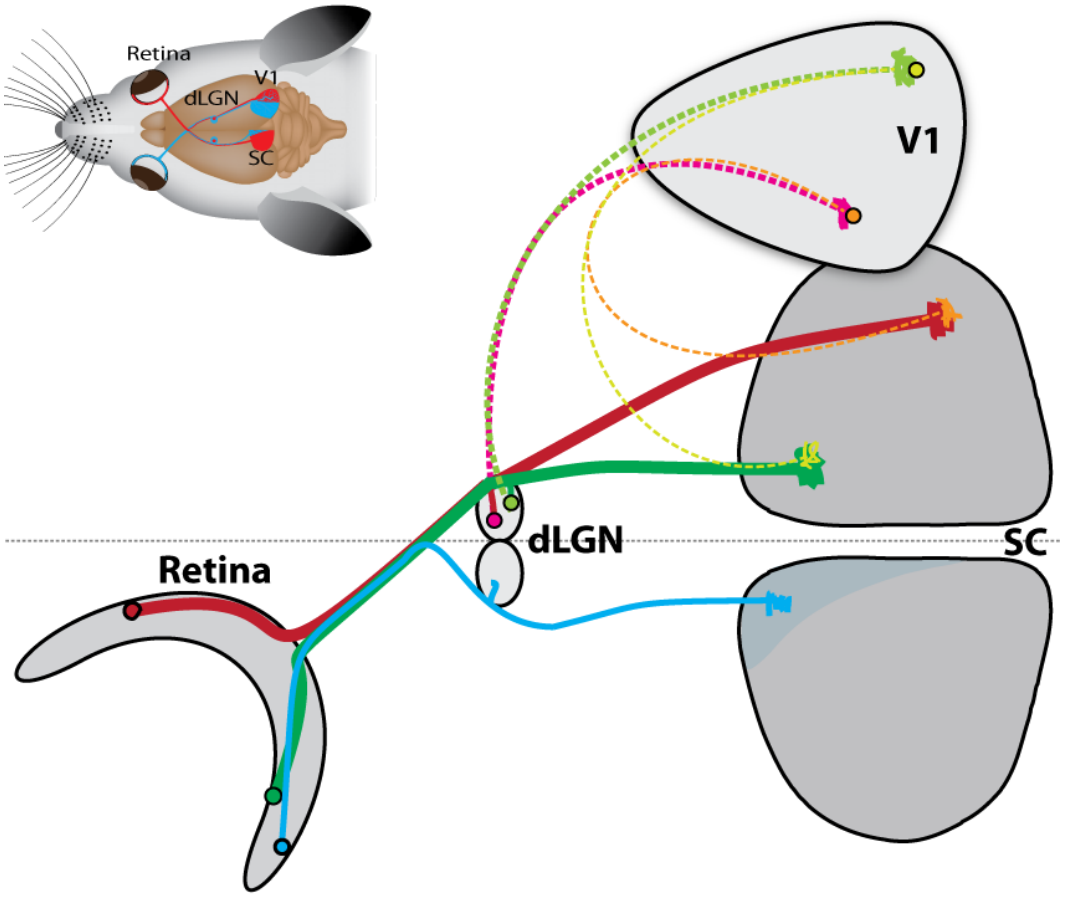

Figure 1-1: Selected Visual Connections in the mouse

Schematic of central image-forming connections, showing two contralaterally projecting retinal ganglion cell axon projections from nasal-dorsal retina (red) and temporal-ventral retina (green), respectively. These axons project across the midline, past the dorsal lateral Geniculate Nucleus (dLGN) and into the Superior Colliculus (SC) (thick solid lines), where they terminate in a topographically appropriate location and lamina. On the way, a significant number of RGC axons branch into the dLGN, where they synapse onto geniculo-cortically projecting cells (pink and light-green, respectively). These cells project to the Primary Visual Cortex (V1) (thick dashed lines). Another loop providing feedback from V1 to SC is also present. These cells project to the topographical location of their input origin (thin dashed lines). Also shown is an ipsilaterally projecting RGC (blue), which projects. Inset of mouse head shows the anatomical locations of the areas and projections in schematic (inset adapted from Levelt and Hübener, 2012)

1.1.2 Retinal circuits

The adult retina is organised into distinct laminae (fig 1B), with outer nuclear layer (ONL) containing the photoreceptors: rods for low luminance, black & white, vision and cones for colour vision. The next layer, the inner nuclear layer (INL) contains the cell bodies of first the horizontal cells, which integrate the signals from surrounding photoreceptors to enhance the contrast, next are the bipolar cells, which convey the signals from mainly photoreceptors onto the retinal ganglion cells and the amacrine cells. In the innermost part of the INL are the amacrine cells, which synapse onto the retinal ganglion cells.

The bipolar and amacrine cells of the INL project into the inner plexiform layer (IPL), where they synapse with the ganglion cells. Within the IPL the signal is further refined by segregating input from ON and OFF bipolar cells and is therefore further laminated into the inner IPL, where ON bipolar cells synapse, and the outer IPL, where OFF bipolar cells synapse. The RGCs can also chiefly be subdivided into ON, OFF subtypes corresponding to which layer their dendrites project to. As an additional complication, the arbours of some RGCs are bistratified and therefore project to both laminas in the IPL; these are ON-OFF RGCs and respond both when light is switched on and off. The RGC cell bodies lie in the ganglion cell layer and project their axons into the nerve fibre layer, where they turn and grow towards the optic disc and into the optic nerve.

Retinal Ganglion Cell subtypes

Although there is some disagreement about exactly how many retinal ganglion cell types there are in the mouse, it is clear that it is a highly diverse group of cells, with both morphology and central projections varying widely. The number of subtypes ranges from 15 to 21, depending on the method used for classification (Badea and Nathans, 2004; Coombs et al., 2006; Völgyi et al., 2009; Yoo et al., 2011). The dendritic arbours range in size from diameters of 55µm to 440µm. The largest RGCs being the intrinsically light-sensitive melanopsin cells (Ecker et al., 2010; Wilks et al., 2010).

Of these RGCs 12 subtypes have been shown to project to the SC (Marquardt et al., 2005; Hong et al., 2011). It is, however, likely that many more do so. The great variability in dendritic arbour sizes is also reflected in this group of RGC subtypes. As the largest RGCs projecting to the SC have dendritic arbours spanning up to 400µm whereas the smallest RCGs span just 55µm. However, while the dendritic arbours vary greatly, the axonal arbours seem to be less variable and with no apparent correlation between the retinal dendritic arbour size and the size of the collicular axonal arbour. The smallest RGC axonal arbours have a diameter of around 100 µm and the largest around 200 µm with a mean size of 135 µm (Carvalho et al., 2006; Hong et al., 2011). It is, however, possible that these do not reflect the full range of arbours, as they only sample a subset of RGC axons. Interestingly, in addition to the presumed tiling within retinal ganglion cell subtypes, some types have also been shown to project in a columnar pattern (Huberman et al., 2009) and project to specific laminae of the SC SGS (Huberman et al., 2009; Kim et al., 2010; Hong et al., 2011)

It has, moreover, been demonstrated that RGCs are connected via gap-junctions to other RGC of the same subtype (Völgyi et al., 2005; Lim et al., 2008b; Völgyi et al., 2009) and that this is dependent on light-exposure, at least for α-ganglion cells (Hu et al., 2010). It is hypothesised that such inter-connectivity aids in effective transmission along the optic nerve by synchronising the base-level of activity within RGC subtypes (Völgyi et al., 2009).

1.1.3 SC circuits and connections

For the purposes of this thesis, the SC is considered primarily as a visual area. It is, however, a truly multi-modal area as it receives visual input as well as input from auditory and somatosensory systems (Edwards et al., 1979).
The superior layers of the SC receive visual input and mainly project to the deeper layers, but also send a projection to the *lateralis posterior* and several thalamic nuclei, including the vLGN(Dean et al., 1989). Along with the input from the retinorecipient layers, the deep layers also receive input from the auditory and somatosensory systems, the contralateral SC and non-visual areas of the cortex. Consequently, the SC has been

shown to be involved in many systems-level functions, such as multi-modal sensory processing (Dräger and Hubel, 1975), motor preparation of saccades (Dorris et al., 1997), and emergent properties such as covert visual spatial attention (Müller et al., 2005; Lovejoy and Krauzlis, 2010; Zénon and Krauzlis, 2012), reward-related modulation (Ikeda and Hikosaka, 2003) and flight responses (Dean et al., 1989).

1.2 Studying maps

The majority of studies of topography in the visual system employ either physiological measures, such as electrode-based multi-unit receptive fields (MURF) or local field potential (LFP) recordings (Dräger and Hubel, 1976; Cang et al., 2008a; e.g. Wang et al., 2010b); intrinsic optical imaging (Mrsic-Flogel et al., 2005; Cang et al., 2008a; e.g. 2008b) and recently, confocal or 2-photon calcium imaging (for review see Scanziani and Häusser, 2009; Smith and Häusser, 2010; e.g. Hofer et al., 2011) or anatomical anterograde tracing methods (Simon and O'Leary, 1992) and retrograde tracing methods (Upton et al., 2007). While there is a solid body of literature regarding the physiological topography and organisation of the SC, the precision and topographic organisation of the anatomical projection is not as well documented. Apart from a few studies quantifying single axon arbour projections (Dhande et al., 2011), most anatomical studies rely on bulk anterograde transport and the label is therefore hard to quantify. An additional problem with this approach is that it is largely restricted to examining peripheral retina.

A further complication is how to compare detailed positional information from physiological experiments with the anatomical data. The problem arises from the fact that the stimuli in physiological experiments is mostly presented on a flat screen that is tangential to the visual field of the mouse and when transformed into visual field coordinates of the mouse is expressed in degrees of azimuth and elevation. In contrast to this, the anatomical studies rely on physical features and markers on the retina and in the targets to convey positional information, which is expressed in terms of distances relative to these markers. Additionally, even between anatomical studies no consistent markers exist to enable comparison of data between studies. These divergent coordinate systems make it hard to directly compare datasets.

1.2.1 Types of neural maps

Arising from the problems of the nervous system having to handle many different types of information, several different methods of segregating information is employed

throughout the nervous system. In the visual system, there are three main types of maps. 1) Continuous maps (Figure 1-2A) convey positional information by maintaining neighbour relationships, so that neighbouring cells in the source (e.g. the retina) also connect to neighbouring cells in the target (e.g. the SC). This type of map is found throughout the sensory and motor systems. 2) Discrete maps (Figure 1-2B) are key for segregating divergent inputs from separate types of cells into functional units, thereby enabling processing of different types of input irrespective of neighbour relationships. Discrete maps are particularly prominent in the olfactory system, where spatial information is not as important. Consequently, the example of lamination in Figure 1-2B is arguably not a true discrete map, but serves to illustrate the complexity that can be conveyed by having several maps on top of each other. 3) The last type of map, exemplified by the ocular dominance columns in the binocular primary visual cortex of e.g. primates (Figure 1-2C) is actually a pseudo-discrete map, where inputs from the separate eyes is arranged in columns to create functional units representing each of the eyes and thereby enabling binocular vision. Key to understanding the complexities of neuronal maps is that all of these maps are present in the same areas and thereby enables simultaneous complex parallel processing of multiple aspects of a signal (Dräger and Hubel, 1976; Cang et al., 2008a; e.g. Wang et al., 2010b). It is important to note that although such anatomical maps are present throughout the nervous system, some spatial relationships are also represented by functional maps that arise through local inhibitory circuits that enable neural coding of information from a subset of specialised neurons, e.g. the emergence of direction-selective cortical cells getting input from specialised intrinsically direction selective retinal ganglion cells (Elstrott and Feller, 2009)

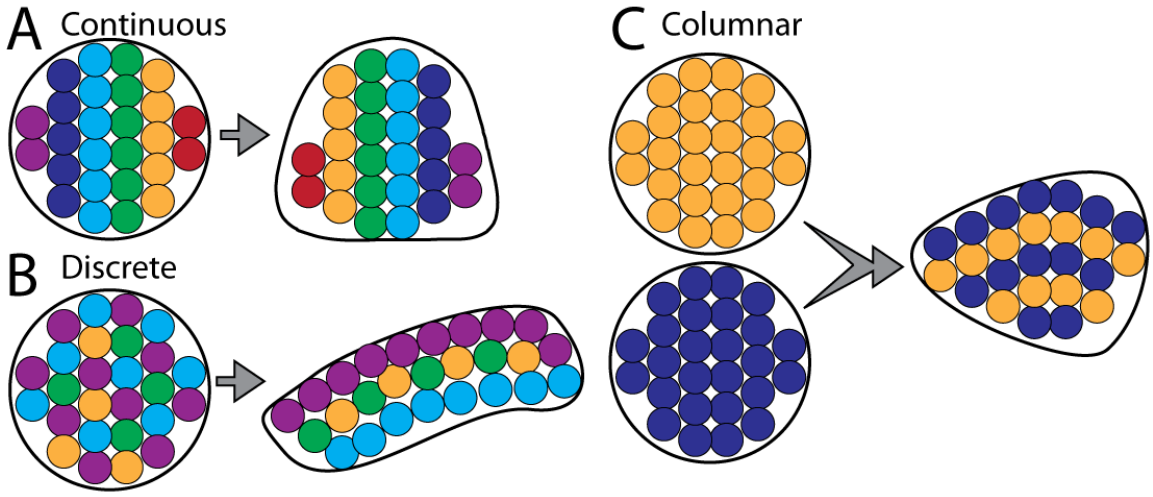

Figure 1-2 Neural mapping strategies

A, A continuous map conveys spatial information and is thus characterised by two neighbouring points in the source are also next to each other in the target. A good example of a continuous map is the topographic mapping of the retina onto the SC. Although only one axis is represented, continuous maps of course represent both axes. **B,** Discrete maps is where cells that are functionally similar, but not necessarily spatially close, project to the same areas. Although it may be arguable whether the example with SC lamination represents a true discrete map, it does show many characteristics of discrete maps. **C,** Columnar maps are common where input from distinct sources needs to be separated spatially. A good example of this is in visual cortex where each eye is represented in separate columns.

1.2.2 Methods used to study maps

In order to study such divergent and complex projections, a multitude of different techniques have been employed. As mentioned previously, there are a several well-established techniques for studying both anatomy and physiology.

Studying Topography using Electrophysiology

Electrophysiological recordings have been used extensively to map out topography in visual structures. Since the electrodes used record changes in electrical potentials of the cells in the targeted area, the data is essentially about the output of the system and arguably local processing may affect the excitation of the cells being recorded from. It is therefore possible that the information gleaned from such recordings is not always directly representative of the actual inputs. Another major factor is that these techniques also rely on using the optimal stimuli to drive the system and may therefore be biased towards certain cell-types depending on the stimuli used, although this can be overcome by using a variety of stimuli, patterned noise or even deconvolved natural scenes. For these reasons, electrophysiological methods cannot be used to investigate precision but are better suited for examining topography (Dräger and Hubel, 1976; Cang et al., 2008a; e.g. Wang et al., 2010b)

Studying Function using Electrophysiology

Another use for such electrophysiological methods relies precisely on different stimuli driving distinct classes of RGCs separately, which causes biases in the topographic population studies. By selecting the stimuli that optimally drives particular cell types, it is possible to investigate the distribution of individual classes of cells and start to tease apart the effects of that type of cell on the target circuit. The stimuli used are generally in the form of: drifting gratings of varying speeds, orientations and sizes; moving bars of different orientations; or moving spots of varying sizes and intensities.

Studying topography using Intrinsic Optical Imaging

Intrinsic optical imaging uses the changes in refraction by oxygenated and de-oxygenated blood to gage the amount of oxygen used by the tissue, which can be used as a proxy for activity and thereby it is possible to functionally map neuronal networks, such as visual cortex (Grinvald et al., 1986). Although more useful than electrode recordings at giving information about the activity of a whole structure, intrinsic optical imaging is still restricted by the stimuli used. More recently, intrinsic optical imaging using a vertical and horizontal moving bar (Kalatsky and Stryker, 2003) has been used to look at topography of the visual cortex and the SC (Mrsic-Flogel et al., 2005; Cang et al., 2008a; e.g. 2008b).

Studying networks using 2-photon imaging

The ability to label cells genetically and the appearance of more reliable activity markers has enabled the study of both inputs to and outputs of circuits, thereby overcoming a lot of the caveats of both electrical recordings and intrinsic optical imaging. Since these techniques enable the labelling of individual identified cells using multiple markers, it can give insights into the processing and resultant functions of neural networks. However, due to the optical nature of these techniques they are, as yet just like intrinsic optical imaging, restricted to studying superficial structures, such as cortex (Kerr et al., 2005; Kerr and Denk, 2008; Scanziani and Häusser, 2009).

Studying Precision using anatomical techniques

Anatomical anterograde tracing methods (e.g. Simon and O'Leary, 1992) have been used extensively to study precision. However, due to the limitations of reliably making small discrete injections of label, the absolute quantitative information of precision gained from such experiments is limited. Moreover, in the visual system, due to difficulties with injecting the central retina, the use of anterograde tracing to investigate topography is limited. For these reasons, while there is a solid body of literature regarding the physiological topography and organisation of the SC, the precision of the anatomical projection is not as well documented. This apart from a few recent studies

that have started quantifying single axon arbour projections and thereby looking at the precision of individual cells (Dhande et al., 2011; Hong et al., 2011). Retrograde tracing methods overcome the problem of not being able to access the central visual field and can sample the entire projection. Moreover, using tracers that have limited diffusion (e.g. Katz et al., 1984; Katz and Iarovici, 1990), it is also possible to examine precision (Upton et al., 2007). Recently, with the advent of genetically modified mice it is now possible to label specific cell-types and thereby study the projections of a single sub-type of cells, e.g. the labelling of a specific ON-OFF DS-RGCs (Huberman et al., 2009). Moreover, by using advanced genetic labelling techniques combined with viral vectors that can label specific connected neurons (e.g. Lo and Anderson, 2011) it would be possible to not only trace the projections of specific ganglion cell projections, but also map their post-synaptic connections.

1.3 The Developing Rodent Visual System

During development, the sequence of neurogenesis and synaptogenesis provides a clue about what mechanisms enable the formation of this intricate circuitry, since the temporal overlap of events, as summarised in table 2.1, could indicate that they may be linked. In the retina, RGCs are the first cells to be born and they are born in a circular fashion, where the first RGCs are born in central retina at around embryonic day (E)11 and the most lateral RGCs are born around E19 (Dräger, 1985). The RGCs immediately send their projections out of the retina through the optic disc around E10-11, after which, contralaterally projecting retinal efferent axons are found by the optic chiasm at E12 and in the dorsal lateral geniculate nucleus (dLGN) and superior colliculus (SC) by E16 (Sernagor et al., 2001). The ipsilaterally projecting RGCs from the ventral-temporal crescent are delayed, reaching the optic chiasm at E16 and only innervating the dLGN and SC between E18 and birth (at E20) (Godement et al., 1984).

In the meantime, the components of the retinal machinery are formed. Coincident with the RGCs, the amacrine cells are born around between E11 and E17 (Cepko et al., 1996) in the outer INL from where they migrate to the INL/IPL border and extend horizontal dendritic branches into the IPL around E17. At the same time RGCs also extend branches into the IPL and synapse with the amacrine cells. Since this is coincident with the onset of early gap-junction mediated correlated bursting between amacrine cells (Cook and Becker, 2009), it is likely that this is one of the mechanisms mediating synaptogenesis between RGCs and amacrine cells. The branches, however, remain highly dynamic and span most of the IPL (Morgan et al., 2008).

Coincident with amacrine neurogenesis, cone photoreceptor precursors and horizontal cells are born in the ONL just before birth. Genesis of rod photoreceptor precursors peaks around the time of birth, followed by the formation of Müller glial cells. Interestingly, the bipolar cells, which convey most of the signals from the outer layers to the inner layers of the retina are mainly born after birth, with peak neurogenesis around postnatal day (P) 3-4 (Cepko et al., 1996). Moreover, the bipolar cells only

synapse onto the RGCs in the IPL several days after birth, indicating that the initial activity-dependent topographical organisation of RGC projections must be due to interactions with amacrine cells. Moreover, since photoreceptors are unable to respond to light until shortly before eye opening (Wong et al., 1995; Wong and Ghosh, 2002), it indicates a crucial role for molecular and intrinsic cues in forming the retinal circuitry

Event	Age
RGC Genesis	E11-19
RGC axons first entering SC	E15
RGC dendrites forming IPL	E17
Amacrine correlated bursting (Stage I)	E17-19/20
Birth	E19-20/P0
Cholinergic activity waves (Stage II)	P0-8
Peak RGC cell death	P2-5
Glutamatergic activity waves (Stage III)	P7-17
Eye opening	P12-15

Table 1-1: Key timings of mouse visual system development

During retinal development, the timings of events are crucial to the proper development of circuitry and projections. The table represents dates from the literature (Sernagor et al., 2001)

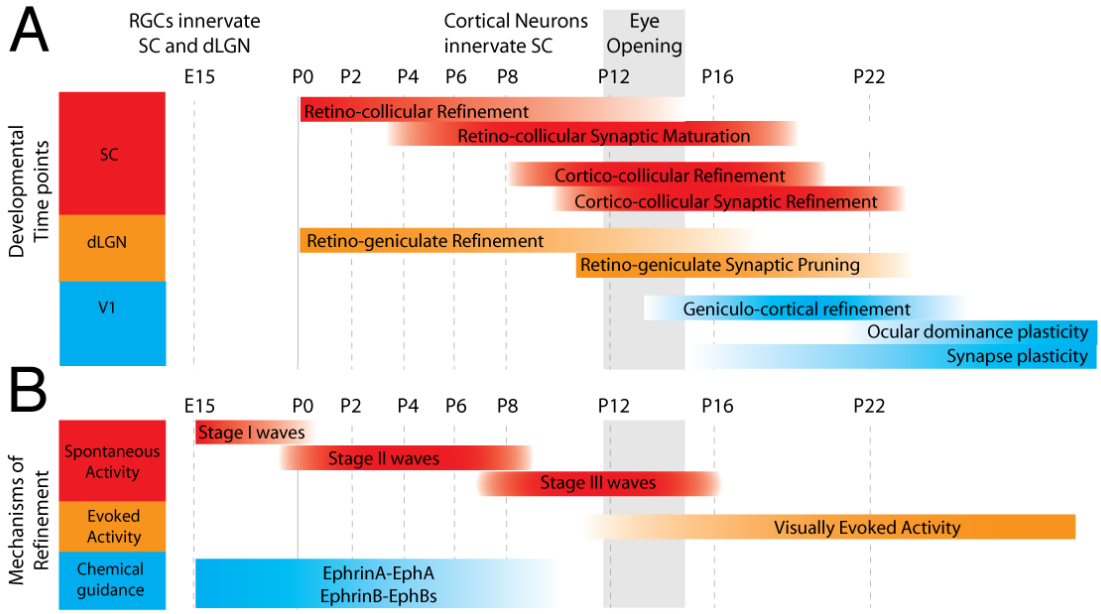

Figure 1-3 Timescale for development of selected mouse retinal projections

A, Schematic summarising phases in the development of the SC, dLGN and V1 during the first 4 postnatal weeks. **B,** The different mechanisms that have been shown to be involved in establishing the visual circuits during the developmental phases in A (Figure adapted from: Huberman et al., 2008a)

1.3.1 Development of the Retino-Collicular projection

Immediately after leaving the retina, RGC axons are organised according to their retinal position (Chan & Guillery, 1994; Jeffery, 2001). As axons grow further along the optic nerve, this sorting seems to disappear and just before the chiasm, at least in rodents, the distribution of axons appears random. After the chiasm, in the optic tract, some measures of order reappear and the axons are segregated along the ML axis of the optic tract according to their approximate dorsal-ventral (DV) retinal position (Chan & Guillery, 1994). The DV segregation just after the chiasm is maintained up to the brachium of the SC (Plas *et al.*, 2005) and is roughly representative of the eventual ML position of the termination zone in the SC (Hindges *et al.*, 2002). It is, therefore possible that this DV segregation plays a role in the initial rough development ML topographic mapping.

It is well established that the formation of the nasal-temporal (NT) retinotopic map consists of two distinct phases of growth. First the axons grow rapidly, with about 2mm/day, through the entire length of the SC until stopping at the border of the Superior Colliculus and the Inferior Colliculus while extending only sparse, simple, branches (Frisen et al., 1998). Then after reaching border the axons start forming more elaborate arbours (Jhaveri *et al.*, 1991), which will eventually constitute their terminal zone. However, since some ML order exists from the tracts (Plas *et al.*, 2005), a level of ML topography develops prior to Anteroposterior (AP) topography (Hindges *et al.*, 2002; Upton *et al.*, 2007), which is dependent on branching (Hindges *et al.*, 2002(Yates et al., 2001)) and pruning of the axon overshoot (Nakamura and O'Leary, 1989).

It is well understood that it is a combination of molecular guidance, mainly facilitated by the Eph/ephrin system and different activity-dependent mechanisms (as detailed in Figure 1-4) that enable the development of collicular retinotopy. The subsequent sections first describes the mechanisms involved in the Eph/ephrin system and then proceeds to describe some of the patterns of spontaneous and evoked activity and how these influence the targeting and refinement of RGC axonal projections.

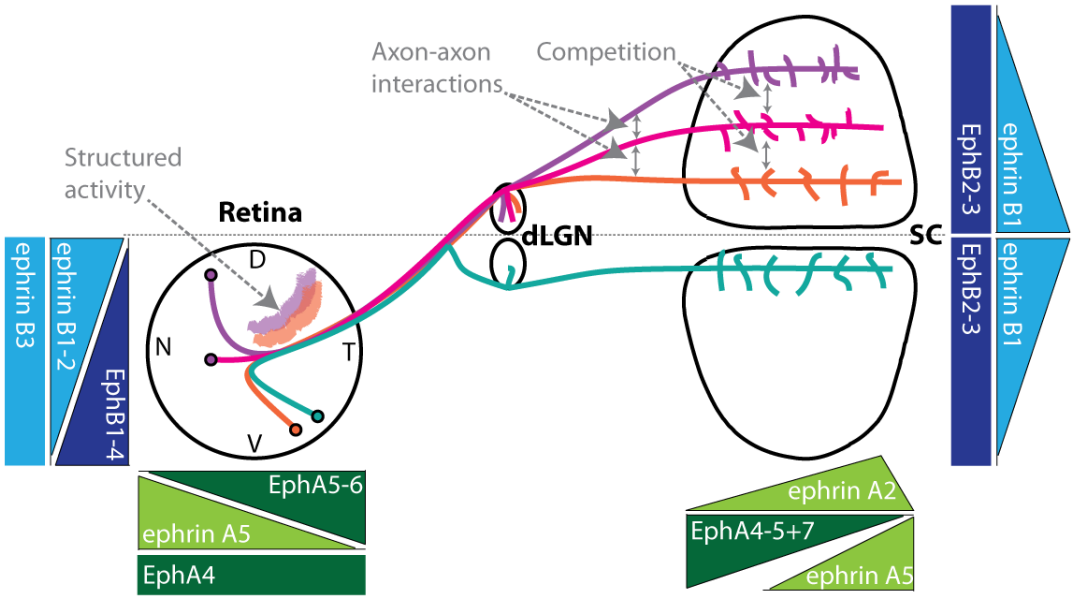

Figure 1-4 Early development of the mouse retinocollicular projection

The diagram illustrates the projections of four RGC axons around the time of birth. Axons grow out of the retina, and apart from a population of ipsilaterally projecting cells in the ventral-temporal crescent (blue axon), project to the contralateral SC. These axons then grow to the posterior edge of the SC, branching all along. During the first week after birth, the overshoot is pruned back and branches are stabilised and elaborated preferentially in the topographically appropriate location (grey circles). Axons grow to the posterior SC due to the repulsive gradient of EphA (dark green) and the ephrin-A counter-gradient (light green) stops the axons at the posterior edge of the SC and allows the axons to branch in the appropriate location while the structured retinal activity and competition in the SC enables the refinement of the axonal branches to form a defined focus. The order in the brachium is thought to be due to the axon-axon interactions in the bundle and causes the axons to enter the SC in the approximately correct ML location with some correction due to branching facilitated by the ephrin-B1 gradient (light blue). For the purposes of clarity, only one eye is represented and the any laminations have been ignored.

1.3.2 The role of molecular guidance

Based on findings that nasal RGC axons exhibited different recognising capabilities from temporal ones and that nasal RGC axon growth cones could not grow on retinal tissue, Bonhoeffer and Huf (1982) initially proposed that a graded repulsive guidance signal in the SC was responsible for guiding temporal RGC axon growth cones directly to their termination zone along the AP axis in chick. It was, however, later shown that although this is the case in zebrafish (Stuermer, 1988) and xenopus (Holt and Harris, 1983), it is not the case in rodents(O'Leary et al., 1986; Jhaveri et al., 1991) or chick (Nakamura and O'Leary, 1989), where axons overshoot their termination zone and later refine their projections. It is possible that this difference arises as a result of the relative size of the tectum/SC in these species. The zebrafish tectum at 5dpf measures around 200μm (Martin Meyer, personal communication), whereas the mouse SC at birth at around 2000μm (see Table 2-4) is 10 times the size.

The retinotopic mapping along the AP axis of the SC has been shown to be largely due to the repulsive nature of Eph receptors and the branch-suppressing properties of ephrin ligands (Drescher et al., 1995). The Eph family is subdivided into nine EphAs (1-8 & 10) and five EphBs (1-4 & 6). The ligands to the Eph receptors are the ephrins, of which there are 5 ephrin As (1-5), which are glycosylphosphatidylinositol-linked proteins, and 3 Ephrin Bs (1-3), which have a transmembrane domain with a short cytoplasmic region. EphAs will generally bind to ephrin-A and EphBs bind to ephrin-Bs, with the exception of EphA4, which can bind both ephrin-As and ephrin-Bs (Klein, 2009).

The expression-pattern of Eph and ephrin is shown in Figure 1-4. In the mouse visual system EphA5, EphA6 & EphB1 receptors are expressed in a graded manner, high temporal to low nasal, across the retina, whereas ephrin-A5 is expressed in a high nasal to low temporal gradient (Cheng et al., 1995; Drescher et al., 1995). These retinal gradients are complemented by gradients in the SC, where EphA4, EphA5 & EphA7 are expressed in a high anterior to low posterior gradient. Ephrin-A2 is expressed in a high-

low posterior-anterior gradient, and ephrin-A5 has a similar graded expression but is restricted to the posterior half of the SC(Carvalho et al., 2006).

These opposing gradients are necessary for the formation of accurate maps, because axon branching then only occurs in the zone with optimal conditions for branching according to the concentrations of Eph & ephrin in the particular RGC (Yates et al., 2001). Observations that have been confirmed by observations that EphA7 at high levels suppress branching anterior to the termination zone (Rashid et al., 2005), while the high levels of ephrin-A5 posterior to the termination zone restricts branching in this region (Frisen et al., 1998; Sakurai et al., 2002), thus confining the branching to the correct area

Along the ML axis of the SC and the DV axis of the retina, a similar gradient to that of EphA/ephrin A is found of EphB/ephrin B. In the retina, EphB1, EphB2, EphB3, EphB4 & EphA6 are expressed in a low to high DV gradient (Holash et al., 1997; Birgbauer et al., 2000; 2001), while ephrin-B1 & ephrin-B2 are expressed in the opposite gradient (Nakagawa et al., 2000; Mann et al., 2002). In the SC, EphB2 & EphB3 are expressed in a low to high ML gradient and ephrin-B1 is expressed in a complementary high to low ML gradient (Marcus et al., 1996)

The mechanisms of molecular guidance cues.

Classically, Eph/ephrin-mediated axon guidance relies on repulsion along a gradient to reach the approximately correct location and competition is then responsible for refining the axon arbour to restrict it spatially. However, it was later found that this was insufficient for forming an accurate map and the mechanisms involved were more complex. Key to the mechanisms involved in the Eph/ephrin-mediated map formation is that the binding of Ephs to ephrins and vice-versa can cause attraction or repulsion and mediate branch promotion or inhibition depending on concentration (Brown et al., 2000) and cis-/trans-conformation of the proteins, which influences the binding properties and sensitivity of the growth cones (Hornberger et al., 1999; Carvalho et al., 2006; Kao and Kania, 2011; Dudanova et al., 2012). The reasons for this is that both

Ephs and ephrins are capable of bidirectional signalling which influences the cytoskeletal response of the growth cone to repulsive or attractive cues. As a result, ephrin-A expressing RGCs are capable of reverse signalling to limit the repulsive interactions with EphA7 in the anterior SC, thus enabling the navigation through the high concentrations in anterior SC (Rashid et al., 2005).

The co-expression and consequent interactions between EphA and ephrin-A within the axons are essential to the axon-guidance mechanisms of EphA & ephrin-A, as ephrin-As when co-expressed with EphA in RGC axons *in vitro* causes phosphorylation of the EphA receptors thus changing their conformation and consequently decreasing their sensitivity to ephrin-A (Hornberger et al., 1999). Another study by Marquardt et al. (2005) demonstrated that EphA and ephrin-A have opposing effects on growth-cone guidance. EphA causes growth cone collapse and consequently is involved in repulsion, whereas ephrin-A mediates attraction. They, furthermore, demonstrated that EphA and ephrin-A are localised in separate membrane domains and have opposing effects on growth-cone guidance, thereby enabling an individual axon growth cone to discriminate between cis- and trans-conformation of the target proteins and facilitating guidance using cues from both EphA and ephrin-A. The apparent discrepancy between direct cis-interactions of Ephs and ephrins influencing the sensitivity and them needing to be in separate compartments to interpret information by both Ephs and ephrins was recently addressed by Kao et al. (2011). They performed experiments on motor neurons, which demonstrated that at low levels of ephrin-A, EphA and ephrin-A are localised in separate cellular domains, whereas at high ephrin-A concentrations, ephrin-A and EphA colocalised within the same domain (Kao and Kania, 2011), thereby decreasing the sensitivity to ephrin-A. Assuming that the same is the case for RGC axons in the SC, then it would explain how nasal axons (with high ephrin-A5 concentration) navigate to the posterior SC and temporal axons (with low ephrin-A5 concentration) branch preferentially in anterior SC. Intriguingly, such compartment localisation could also be changed by other factors influencing the membrane composition and structure, such as activity.

It is well established that Eph receptors are transmembrane proteins with a kinase domain and a PDZ domain, enabling them to bind to intracellular scaffolding proteins and signal back to the soma. Ephrin-Bs are transmembrane proteins with just a PDZ domain, but since they do not have a kinase domain, they signal through intracellular kinases and phosphatases. When EphB receptors and ephrin-Bs bind, the mutual signalling capabilities enable a bidirectional signalling that is important in mediating the shift from attraction to repulsion to ephrin-Bs in axons expressing EphB (Kullander and Klein, 2002; McLaughlin et al., 2003a).

Ephrin-As, in contrast, are GPI-linked and don't have intracellular domains. Ephrin-As have, however, been shown to be localised to lipid rafts (Davy et al., 1999) where they form complexes with the two neurotrophic receptors p75 (Lim et al., 2008b) and TrkB (Marler et al., 2008). Both of which enable ephrin-As to influence the cell in a number of ways. It has been demonstrated that pro-BDNF causes binding of ephrin-A to P75, which causes branch-suppression by initiating reverse signalling (Lim et al., 2008b) and thereby facilitating endocytosis of the EphA/ephrin-A complex (Yoo et al., 2011). In contrast, when TrkB is activated by BDNF, it causes a shift from branch-suppression to branch-promotion by ephrin-A5 (Marler et al., 2008). Thereby indicating that local shifts of the properties of ephrin-A5 may be contributing to increased branching in the area around the termination zone, where the levels of the reverse gradient of EphA allows for it.

Additionally to enabling the formation of correct retinocollicular projections, the Eph/ephrin system also enables the alignment of convergent retinotopic maps, such as the cortico-collicular projection (Wilks et al., 2010). This was demonstrated by showing that removal of ephrin-A5 causes misalignment of the cortico-collicular projection to the retino-collicular projection. Importantly, this alignment of maps is not restricted to the visual system, but has also been shown to be essential for the alignment of multimodal input to the deep layers of the SC (Triplett et al., 2012)

Similar to the EphA/ephrin A system, Ephrin Bs can act as both chemo attractant (Mann et al., 2002) and chemo repellent (Birgbauer et al., 2001), dependent on low or high concentrations respectively, thus promoting axon branching in the ML direction of their correct termination zone (Hindges et al., 2002; McLaughlin et al., 2003a). Ephrin-Bs have, moreover, also been shown to be involved in stabilising synapses after mediating contact.

Roles of Eph/ephrin in synaptogenesis

The transmembrane structure and the bidirectional signalling capabilities of Eph receptors and the ephrins allow for the complex mechanisms of guidance by enabling shifts from chemorepulsion to chemoattraction dependent on concentration and activity (McLaughlin et al., 2003a; Hanson and Landmesser, 2004). But not only do the ephrins play an important role in development of large-scale topography by axon guidance and branching, Ephs and ephrins have also been shown to be implicated in forming the synaptic micro-topography (Klein, 2009).

The direct role of Ephs and ephrins in synaptogenesis in the visual system has not yet been fully elucidated, but it is likely that they play a role in regulating these events, since evidence looking at the function of EphB2 forward signalling in hippocampus suggest that they play a role in spine formation through their cell adhesion properties (Henkemeyer et al., 2003); and in the regulation of subsequent stabilisation and synaptogenesis (Kayser et al., 2008) of Glutamatergic synapses through causing decreased motility and a higher rate of postsynaptically induced synaptogenesis during critical period. EphBs have, moreover, also been shown to directly interact with NMDA receptors and stabilise synapses, as perturbed EphB activity causes a reduction of specialised synapses in hippocampal cultures (Dalva et al., 2000). Moreover, EphB has been shown to be directly implicated in synaptic plasticity of the xenopus tectum (Lim et al., 2008a)through Wnt-dependent signalling (Lim et al., 2010).

Another aspect that remains to be fully established is the role of ephrin-A5 in synaptogenesis. As already mentioned, ephrin-A5 has been shown to bind to and

activate TrkB and cause increased branching (Marler et al., 2008). So since both TrkB and Ephrin As are in lipid rafts together and can bind PSD-95 through their PDZ domain (Davy et al., 1999), and since TrkB activation directly affects synaptogenesis and NMDA clustering (Suzuki et al., 2004; Yoshii and Constantine-Paton, 2007), this may provide another mechanism of action for ephrin-A5 in SC synaptogenesis.

Another role of activity is that the function of the Eph/ephrin system may be activity-dependent, as demonstrated by Nicol et al. (2007) for Ephrin A5. They found the repulsive actions of EphAs on ephrin-As to be activity-dependent, as changes in activity in the form of cAMP oscillations are required for branch-retraction in vitro (Nicol et al., 2007).

1.3.3 The role of Activity

Information about position is key to enabling a reliable transmission of topographic signals from source to target. This is the case, not only in the visual system, but wherever positional information needs to be conveyed. The key to the process is maintaining neighbour relationships, so that neighbouring RGCs project to adjacent areas in the target. This information can be conveyed by structured neural activity, whereby neighbouring neurons exhibit correlated firing and therefore neighbours will be more coactive (Willshaw and Malsburg, 1976), which facilitates Hebbian plasticity and results in strengthening of connections from neighbouring RGC axons onto the same post-synaptic collicular cells (Hebb, 1949).

Early experiments showed that activity was important in eye segregation and the maintenance of ocular dominance columns in cortex since depriving one eye caused the ocular dominance columns representing that eye to be smaller than the open eye (Shatz and Stryker, 1978). Later experiments confirmed the requirement of activity in development of eye segregation by demonstrating that blocking retinal activity using tetrodotoxin (TTX), a potent Na^+ channel blocker, prevented the formation of ocular dominance columns in cortex (Stryker and Harris, 1986), disrupted the segregation of eye-specific inputs in the dLGN (Shatz and Stryker, 1988); and caused the ipsilateral

projection, which in the SC is normally confined to the anterior-medial SC, to be more diffuse and no longer segregated from the contralateral projection (Thompson and Holt, 1989)

In parallel to these observations of eye segregation, it was demonstrated using TTX that activity also was essential for forming appropriately sized axonal arbours (Sretavan et al., 1988), thus also implicating activity in the formation of retinotopic organisation. Around the same time, it was established that retinal ganglion cells are spontaneously active already during the initial guidance (Galli and Maffei, 1988). It was subsequently showed by the same group that the activity of neighbouring RGCs is correlated (Maffei and Galli-Resta, 1990). The feasibility of this was later confirmed by the demonstration that correlated activity in neighbouring RGCs caused a strengthening of connections onto tectal neurons (Zhang et al., 1998), thus providing a mechanism for formation of retinotopic maps according to Hebbian principles (Song et al., 2000).

It has subsequently been shown that such spontaneous intrinsic activity is present in many different forms throughout development of the visual system. The retinal circuitry that enables such spontaneous synchronised [Ca2+]-dependent activity in the mouse retina is developed over three main periods. E16-P0 (Stage I), P0-P9 (Stage II) and P9-P14 (Stage II) (Bansal et al., 2000). It is believed that since the various stages of activity are mediated by different mechanisms they provide a variety of activity-patterns that are involved in all aspects of axon guidance and refinement: Stage I activity relies on non-nicotinic gap-junction mediated transmission; Stage II is dependent on nicotinic acetylcholine transmission; and Stage III is mediated by ionotropic glutamate receptors (Huberman et al., 2008a).

Stage I waves are gap-junction dependent

The first signs of correlated activity appear in retinal amacrine cells around E16 and last until the time of birth (Bansal et al., 2000). Since this activity starts before the main stages of synapse formation it is initially mediated by gap-junctions, as the activity-patterns can be blocked by gap-junction blockers and adenosine receptor blockade, but

crucially are unaffected by nicotinic antagonists (Syed et al., 2004). This initial activity is chiefly characterised by small clusters of cells having correlated activity mediated by gap-junctions (Syed et al., 2004), which is believed to convey information to segregate eye-specific inputs. The second, smaller component are of large propagating waves mediated by nicotinic Acetylcholine Receptors (nAChR), but since these waves are too large to convey any spatiotemporal information, it is unlikely that they are involved in refinement and they are probably just a manifestation of the immature system for stage II waves (Bansal et al., 2000).

Stage II waves are Acetylcholine dependent

Around the time of birth, the early spontaneous activity in amacrine cells start being propagated across the retina in a more structured and tighter wavelike manner in both amacrine cells and RGCs (Wong et al., 1995). The waves spread across the retina with a speed of about 100μm/s and wave fronts of several hundred micrometres (Stafford et al., 2009). Properties that are appropriate to convey spatial and temporal information about RGCs to enable the sorting and refinement of axon arbour terminals in target zones (Meister et al., 1991). These waves persist throughout the first week after birth and have been shown to be dependent on nAChRs, as conditional knock-out of nAChRs in the retina completely abolishes the structured activity waves (Stacy et al., 2005) and even subtle changes, such as the lack of the β2 subunit of the nAChRs were initially thought to abolish the waves (Bansal et al., 2000). It has, however since been shown that structured waves, albeit with altered spatiotemporal properties, are present in animals lacking the nAChR-β2 subunit (Sun et al., 2008b; Stafford et al., 2009).

The significance of those waves, however, remain an open question, since the altered waves cause large-scale anatomical, but only small functional changes in dLGN (Grubb et al., 2003), along with grossly altered anatomical topography in the SC (McLaughlin et al., 2003b; Chandrasekaran et al., 2005), where the functional map of visual space also appears to be expanded in the anterior SC and compressed in the posterior SC (Mrsic-Flogel et al., 2005).

Additionally to their role in formation of retinotopy, the nAChR-β2-dependent waves are also thought to be implicated in the segregation of eye-specific inputs to the dLGN, as RGC axon arbours from the ipsilateral eye project to a larger area in the nAChR-β2 knockout than in the wild type (Sun et al., 2008b). Moreover, modelling has shown that the short period of the waves combined with the long inter-wave interval is ideal for desynchronising the outputs from the eyes and therefore support a Hebbian mechanism of refinement (Butts et al., 2007),

If the changes in wave-characteristics by Sun et al. (2008b) and Stafford et al. (2009) are taken into account it is then plausible that it is the precise structure and pattern of the waves that is important for the retinotopic mapping, which then opens the question of the role of the other nAChR subunits in generating the waves, since removing the α3-subunit also has been shown to alter the spatiotemporal properties of the waves (Bansal et al., 2000). However, retinotopic maps have not been studied in this mutant.

Moreover, some gap junction-mediated spontaneous activity persists in the amacrine cells of animals without any cholinergic activity due to the removal of choline acetyltransferase, which is solely responsible for synthesising Acetylcholine. The activity in these cells is, however, random, unstructured and of different amplitude and speed to wild type animals (Stacy et al., 2005). These findings have, furthermore, been corroborated by evidence that removal of Connexin 36 & 45, which are involved in gap-junction signalling in neonatal animals, affects the firing patterns of individual RGCs (Blankenship et al., 2011).

Interestingly, nAChR-β2 knockout animals have also been shown to exhibit altered expression of genes involved in cell adhesion and Ca2+ signalling along with increases in genes associated with degeneration using a gene-chip approach (Rubin et al., 2011). Considering the defects of axon guidance in the dLGN in the nAChR-β2 knockout mice (Grubb et al., 2003; Sun et al., 2008b), it may be of particular interest that the mutant shows decreased expression at P4 of mRNA coding for cell adhesion molecule Cadherin-1, along with SPP1 and LYPD2, all of which have been shown to be involved

in axon guidance (Rubin et al., 2011). Overall, it suggests that correlated activity may play as yet unknown roles by regulating expression of genes that are involved in axon guidance. It is probable that the mechanism of this effect acts through changes in Ca^{2+} concentration (Rubin et al., 2011). Finally, it is also worth noting that no changes were seen in Eph/ephrin expression.

Stage III waves are Glutamate dependent

Stage III waves start around P8-10 and persist for about 10 days, although this occurs earlier in the animals lacking the nAChR β2 subunit (Bansal et al., 2000), possibly as a compensatory mechanism. Since Stage III waves span the time of eye opening it is difficult to discern which aspects of development are attributable to the Glutamatergic waves and which are attributable to eye opening and resultant increase in visual stimulation. The waves are caused by release of glutamate from bipolar cells onto RGC dendrites in the IPL (Bansal et al., 2000; Wong et al., 2000). The waves have been shown to play a role in the lamination of the retinal inner plexiform layer (IPL) and the segregation of the RGC dendrites into ON (inner two-thirds of the IPL) and OFF (outer two-thirds of the IPL) (Morgan et al., 2008). The effects of the waves are, however, probably not restricted to the retina, but may also play a part in the ON/OFF segregation in the dLGN and SC. The reason being that since the frequencies of the waves differ significantly between the ON and OFF bipolar cells, OFF cells firing at a higher frequency than ON (Huberman et al., 2008b), and ON cells fire just before OFF cells (Kerschensteiner and Wong, 2008), it may enable segregation in targets, in accordance with Hebbian mechanisms (Willshaw and Malsburg, 1976).

It is, moreover, very likely that the Glutamatergic waves are responsible, not only for segregating ON and OFF RGCs, but also play a key instructive role in the differentiation of α-RGCs, β-RGCs & γ-RGCs and subsequent segregation of these in targets since these all exhibit specific firing patterns (Liets et al., 2003). This would also mean that they possibly play a role in determining which lamina in the SC the RGCs eventually project to, since the SC lamination appears to be sub-type specific (Hofbauer

and Dräger, 1985; Huberman et al., 2008b; Kim et al., 2010) although the mechanisms of this lamination remains unresolved.

As for the roles of synaptic transmission in development of collicular retinotopy during the period of the GluR-dependent waves, it has been demonstrated that the refinement during this period is dependent on synapse strengthening and elimination, both of which have been shown to be dependent on NMDAR activation, as NMDAR-blockade prevents refinement of ectopic arbours in the contralateral (Colonnese and Constantine-Paton, 2006), but not ipsilateral (Colonnese and Constantine-Paton, 2001), projection. These effects on synapse plasticity may also suggest a role for GluR-dependent waves in fine-scale refinements of projections.

Stage III waves have been reported to end around P15-20 in mouse, and since waves of spontaneous activity might affect the transmission, it has been hypothesised that visual experience following eye-opening might be linked to the disappearance of the waves. It has, however, been shown by Demas et al. (2003) that the waves end around P15 even when animals are reared in the dark.

Eye opening

Although most of the retinotopic refinement is mediated by intrinsic cues with some sensory input just prior to eye opening (Akerman et al., 2002; Colonnese et al., 2010), it has been shown that eye-opening at around P13 in mouse, causes a rapid, refinement and increased synaptogenesis in visual cortex (Hooks and Chen, 2008) along with maturation of local GABAergic cortical networks (Hensch et al., 1998). Such changes which would indicate that the increased visual input spurs an increase in activity, followed by increased plasticity in the visual targets (Lu and Constantine-Paton, 2004), higher levels of PSD-95 in dendritic spines (Yoshii et al., 2003). In these studies, it was observed that eye opening caused an initial increase in silent synapses featuring mostly NMDA receptors, followed by a slow activation, caused by the transition to AMPA receptor currents over the first 24 hours after eye opening. The results indicate a classical LTP mechanism in response to increased sensory input (Wu et al., 1996).

The consequences of such changes in synaptogenic dynamics are also thought to be involved in establishing the balance of ocular dominance in the binocular region of visual cortex during this critical period through Hebbian and homeostatic mechanisms (Mrsic-Flogel et al., 2007). The ocular dominance balance is further facilitated by a delayed shift in inhibitory GABAergic innervation, which potentiates the strengthening of excitatory inputs following monocular deprivation (Fagiolini and Hensch, 2000; Gandhi et al., 2008). Not only is input from each eye segregated during this period, but functionally cells are also matched up, e.g. according to preferred orientation (Wang et al., 2010a) during this same period. Together these mechanisms are believed to enable the improvement in visual acuity, which is observed from around P20 to P30 (Cancedda et al., 2004).

Concurrent with the critical period, eye opening, and the subsequent visual input has, moreover, been demonstrated to facilitate the alignment of the sensory maps between primary visual cortex (V1) and the SC by synchronising spatial information and thereby enabling the topographical order in the cortico-collicular projection (Phillips et al., 2011).

1.3.4 Cell death

The development of the nervous system includes a distinct phase of neuronal degeneration during which a substantial proportion of the neurons initially generated die in programmed cell death. Programmed cell death is a key mechanism in development and refinement of structures. In the visual system around 50% of RGCs die during the first postnatal week (see table 2.1). Using retrograde transport of fluorescent fast blue dye, it was initially demonstrated that a significant proportion of aberrantly projecting RGCs were removed between P2 and P12 (Cowan et al., 1984; O'Leary et al., 1986). The experiments, however, were rather crude, but were later substantiated by evidence from retrograde transport of fluorescent latex microspheres, where it was also shown that a higher proportion of ectopically projecting cells die. (Upton et al., 2007). Another finding of this study was, however, that the contribution of selective cell death has a very limited role in topographic refinement.

The mechanism of refinement by cell death is thought to be mainly competition-dependent, as cells require target derived neurotrophic factors, such as BDNF, to survive and since there is only a limited amount of neurotrophic factors, the cells that fail to make appropriate connections undergo programmed cell death. The specificity in the system comes from the formation of synapses being regulated by molecular guidance cues and structured activity, as reviewed earlier. In the SC, it is very likely that most of the programmed cell death is governed by the availability of BDNF, since this is present throughout the SC and it has been shown that RGCs express both TrkB and p75, which are the main receptors for BDNF. This is, moreover, substantiated by evidence that BDNF injection into the SC reduces cell death (Ma et al., 1998)

1.4 Aims

Both molecular and activity-based cues have been clearly shown to influence and direct the development of anatomical and functional retinotopic maps. Nevertheless, it has remained controversial whether activity is required for the read-out of molecular gradients. Recently, however, there is emerging evidence for the requirement of activity in retinotopic mapping. What remains to be established is what the roles of specific patterns of activity are in segregating the input into the SC and what role this structured activity plays in forming precise anatomical and functional topographically correct connections.

This thesis will focus on investigating anatomical precision in the projection from the retina to the superior colliculus. Initially (in Chapter 3), the focus is on establishing and verifying a model of standardised retinal space and thereby touching on points regarding the comparison of physiological and anatomical data and the importance of knowing the orientation of the head and eyes of the mouse. Following on from these observations, a description of anatomical precision is provided for two different mouse-strains (albino, CD-1; and black, C57BL6/J). Having established a standardised retinal space for comparing retinae of varying shapes and sizes, chapter 4 focuses on the post-natal development of precision in the retino-collicular projection. The main aim of this chapter is to provide a thorough quantitative description of the spatiotemporal dynamics of the postnatal development of precision by focusing on the first three postnatal weeks. Finally, in chapter 5, the emphasis shifts to answering questions about the role of spontaneous Acetylcholinergic activity in the first week after birth by examining the nAChR-β2 knockout mice. An investigation that is made possible by the standard retinal space established in chapter 3 and facilitated by comparison to the framework established in chapter 4.

Chapter 2 Materials and Methods

2.1 Animals

Wild type C57BL/6JOlaHsd (Harlan, UK) and C57BL/6J (Charles River, UK) mice (*mus musculus*) were used, as indicated. All mutants used are on the C57BL/6J background and controls for experiments with mutants were either heterozygous littermates or wild-type C57BL/6J. Albino mice used are CD-1 (Charles River, UK).

Most neonatal animals were bred in-house from above strains; a small number of animals came from pregnant females purchased from Harlan or Charles River. Animals were housed on 12-hour light/dark cycle and used at ages from postnatal day (P) 0 to P30 and adult (8-52 weeks).

All procedures were performed in accordance with the European Communities Council Directive of 24 November 1986 (86/609/EEC) under the Animals (Scientific Procedures) Act 1986.

2.1.1 nAChR-β2 mutant mice

The nAChR-$\beta2^{-/-}$ mice carry a null-mutation for the CHRNB2 gene (Picciotto et al., 1995).

Genotyping was done using primers for CHRNB2(Picciotto et al., 1995; Bansal et al., 2000):
forward: 5'-GCTTCGCCTCCGGGGCGGAGAC-3'
reverse: 5'-CCAAAGCTGAACAGCAGCGCCAT-3'
and primers for β-Gal:
forward: 5'-CGGGCAAATAATATCGGTGGCCGTGG-3'
reverse: 5'-CACTACGTCTGAACGTCGAAAACCCG-3'

The wild-type nAChR-β2 generates a product at 300bp and the β-Gal generates a product at 600bp. nAChR-$\beta2^{-/-}$ only has a band at 600bp; nAChR-$\beta2^{+/-}$ has bands at 300bp and 600bp; and nAChR-$\beta2^{+/+}$ only has a band at 300bp.

2.1.2 Anaesthetic Regimes:

Animals were anaesthetised either by intraperitoneal injection with a mixture of Ketamine Hydrochloride (100mg/ml; Vetalar V, Pfizer, UK) / Xylazine (2% w/v; Rompun, Bayer Healthcare, UK) using a dose appropriate for the age (see table 2.1) or by inhalation of Isoflurane-Vet (100% w/w; Merial Animal Health, UK) with medical oxygen at an appropriate concentration and flow-rate for the age (see Table 2-1).

Animals older than P4 were maintained at 37˚C for the duration of the experiment. Animals younger than P4 were maintained at 20˚C for the duration of the experiment to aid neuro-protection. All animals were allowed to recover fully at 37˚C before being returned to their original cage.

Age (days)	Anaesthetic	Dose
0-3	1:30 Ketamine (100mg/ml), 1:60 Xylazine (2% w/v)	0.025 ml/g (ket:170 / xyl:17 mg/kg)
4-22	1:15 Ketamine (100mg/ml), 1:30 Xylazine (2% w/v)	0.015ml/g
60+	1:1.5 Ketamine (100mg/ml), 1:3.0 Xylazine (2% w/v)	0.003ml/g
4-7	Isoflurane	2-2.5%; 0.7 litres/sec
8-19	Isoflurane	1.5-2%; 0.6 litres/sec
20-60+	Isoflurane	1.5-2%; 0.4 litres/sec

Table 2-1: Anaesthetic regimes

Ketamine/Xylazine was always used as anaesthetic for neonatal animals and was also used in some older animals, but for most animals older than P4, the most commonly used anaesthetic was Isoflurane

2.1.3 Perfusion Fixation

After a recovery period of 24 hours for neonatal animals and 48 hours for adults, the animals were terminally anaesthetised by intraperitoneal injection of 300mg/kg of pentobarbital sodium (200mg/ml; Euthatal, Merial Animal Health, UK). Animals were perfused with a transcardial injection of phosphate buffered saline (PBS; Dulbecco A) at 4˚C using a peristaltic pump until all blood was displaced. At this point the PBS was replaced by 4% paraformaldehyde (PFA; TAAB Laboratory Supplies, UK) in PBS at 4˚C and heart was perfused until limbs went stiff.

2.1.4 Retinal Dissections.

Initially a marker cut was aligned with the dorsal side of the forming eyelids and the eyes removed. However, due to variation in the eye-rotation and head shape between ages, this was changed to a cut that is aligned with the nictitating membrane, which was verified as being consistently nasal in the adult by the attachments of the eye muscles. During the flat mounting, typically 3 or 4 minor cuts were made at approximately 120˚ or 90˚ to enable flattening (see **Error! Reference source not found.**A for example). The retinae were subsequently dissected out in 1% PFA and flat mounted on Poly-l-lysine slides in Fluoromount (Sigma, UK) for retinae containing Retrobeads (Lumafluor, USA), as beads are dissolved by Glycerol, or Fluoromount-G (Cambridge Bioscience, UK) for other retinae and coverslipped using #0 coverslips.

2.1.5 Retinal Immunohistochemistry

Retinae were washed with PBS-Tx (PBS + 1% TritonX-100) followed by blocking in Normal Goat Serum (1:10; Cambridge Bioscience) in PBS-Tx for 2 hours. Retinae were then incubated in primary antibody (See Table 2-1 below for details of antibodies) diluted in NGS+PBS-Tx over night at 4˚C. Subsequently, retinae were washed with PBS and incubated with secondary antibody for 2 hours. After which the retinae were washed with PBS and mounted on Poly-l-lysine slides with Fluoromount-G (Cambridge Bioscience) and coverslipped with #0 coverslips.

Primary Antibodies						
Clone	**Host**	**Reactivity**	**Isotype**	**Conc.**	**Supplier**	**Part no.**
SMI-32	Mouse	Mouse	IgG1	1:1000	Cambridge Bioscience	SMI-32R
S-opsin	Rabbit	Mouse	IgG	1:200	Millipore	AB5407
Secondary Antibodies						
Conjugate	**Host**	**Reactivity**	**Isotype**	**Conc.**	**Supplier**	**Part no.**
AlexaFluor 488	Goat	Mouse	IgG1	1:1000	Invitrogen	A-21121
Fluorescein	Goat	Rabbit	IgG	1:1000	Millipore	AP132F

Table 2-2 List of Antibodies

2.2 Reconstructing retinae

2.2.1 Retinal reconstruction

To compensate for the variance in retinal dissections we have developed software in collaboration with David Sterratt (University of Edinburgh) to reconstruct the dissected retinae. The software joins up the edges of the cuts in the retina using Delaunay triangulation (Figure 2-1A) and plots retinal outline and retinal label locations onto a curtailed sphere (Figure 2-1B) of rim angle corresponding to the shape of the eye at a given age (see Table 2-3) and then using the following energy function to optimise the projection by adjusting the lengths of the sides of the triangles to be the same on the spherical and flattened retinae (See Figure 2-1C-D).

$$E_L = \frac{1}{2|C|\bar{L}} \sum_{i \in C} \frac{(l_i - L_i)^2}{L_i} + \beta \sum_{j \in \tau} \left(\frac{A_j}{\bar{A}}\right)^v f\left(\frac{a_j}{A_j}\right)$$

Equation 2-1 Length-energy function

Where L_i and l_i are lengths of corresponding connections $i \in C$ in flattened and spherical retina, respectively. $\bar{L}$ is the mean of L_i.

The penalty term in Equation 2-1 prevents triangles from flipping over. The lengths of l_i on the sphere are calculated by using the central angle formula for each of the vertices of l_i, as given by:

$$l(\varphi_1, \lambda_1, \varphi_2, \lambda_2) = R \arccos(\cos\varphi_1 \cos\varphi_2 \cos(\lambda_1 - \lambda_2) + \sin\varphi_1 \sin\varphi_2).$$

Equation 2-2 Central angle formula

The penalty term in Equation 2-1 is controlled by the parameter β, which controls the relative contribution of the area penalty and v, which determines how much more large triangles are penalised. A_j and a_j are signed areas of corresponding triangles $i \in \tau$ in flattened and spherical retina, respectively. Signed area is positive for triangles in

correct orientation, but negative for flipped triangles, thereby preventing flipping of triangles.

f is a piecewise smooth function that increases with negative arguments. However, since $x_0 = 0.5$, triangles are only penalised if size is halved when reconstructed, according to:

$$f(x) = \begin{cases} -(x - x_o)/2 & x < 0 \\ \frac{1}{2x_0}(x - x_0)^2 & -< x < x_0 \\ 0 & x > x_0 \end{cases}$$

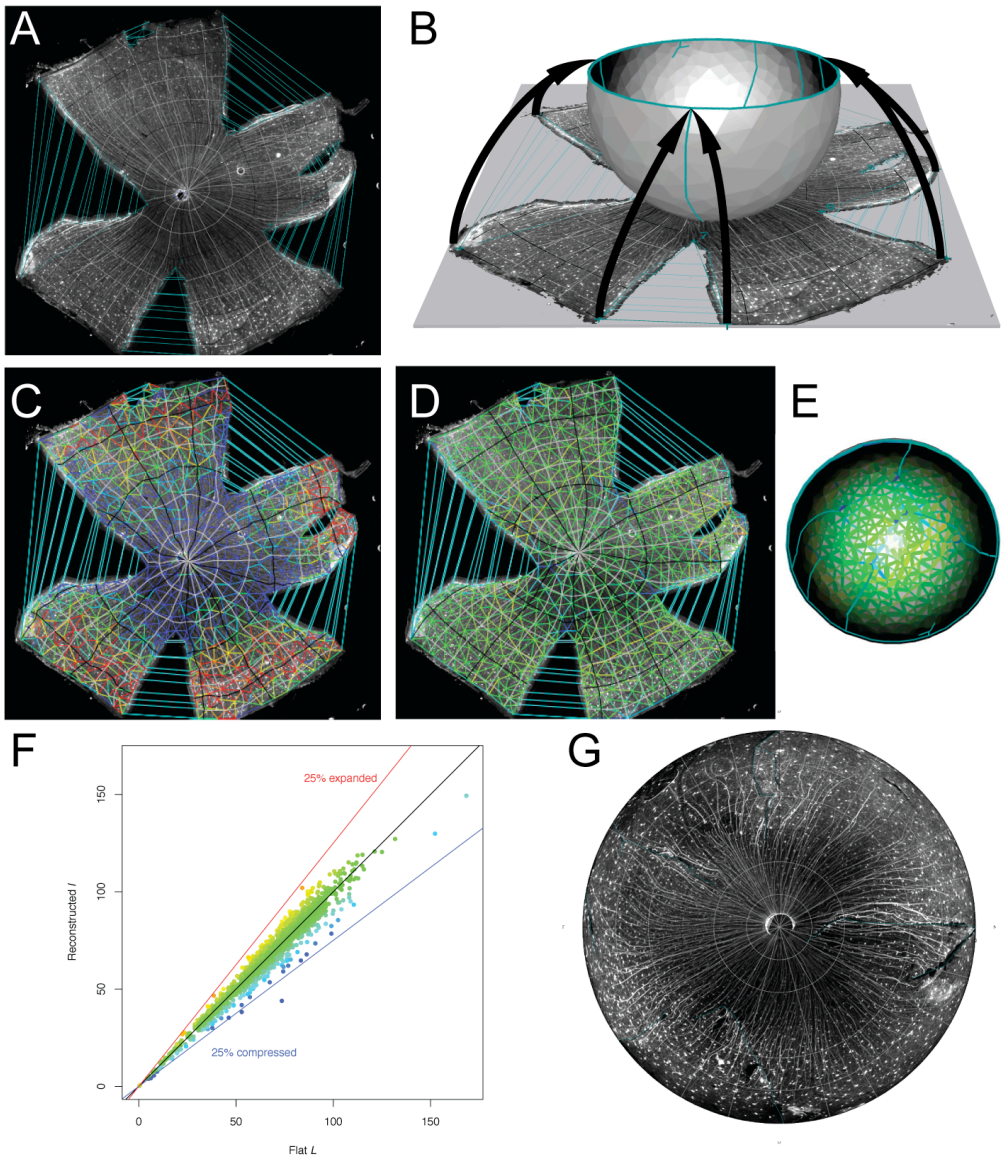

Figure 2-1 Legend: Reconstruction of Retinae (Next page)

A, Flat-mounted retina of adult animal stained for SMI-32 to label soma and axons of a subset of RGCs. Image consists of 12 images acquired at 5x and stitched together. Blue lines connect points that have been matched along rim. Nasal is on left. **B,** Diagram illustrating how the retinal outline in A is projected onto a sphere with rim-latitude of 111.6˚ (See Table 2-2). **C,** Initial distortions introduced by projecting the flat-mount onto the sphere without optimisation. Red lines are longer on sphere than on flat-mount and blue lines are shorter. Note that periphery is expanded, whereas centre is compressed. **D,** Distortions following 13 iterations of optimisation, reducing √EL from 0.027 to 0.0021.**E,** Distortions in D plotted onto the sphere in A, but viewed from front. **F,** Length of individual gridlines on sphere plotted against length on flat-mount. Red line indicates 25% expansion and blue line is 25% compression. **G,** Azimuthal equilateral polar projection of flat-mount in A. Note how axons now line up with grid lines.

2.2.2 Evaluation of the reconstruction algorithm

The deformations associated with a reconstructed retina can be estimated as the square root of the length energy function (Equation 2-1), as given by:

$$\sqrt{E_L} = \sqrt{\frac{1}{2|C|\bar{L}} \sum_{i \in C} \frac{(l_i - L_i)^2}{L_i}}$$

Equation 2-3 Distortion measure

The deformation of individual lines can thereby be visualised by plotting L_i against l_i, as in Figure 2-1F, or by colour-coding the flat-mount grid, so that compression ($L_i > l_i$) is blue, expansion ($L_i < l_i$) is red and equal length is green, as seen in Figure 2-1C-D to give a quick overview of the distortions involved in the reconstruction. The algorithm runs several iterations; first without the penalty term (in Equation 2-1) and then with the penalty term until $\sqrt{E_L}$ is constant for 3 iterations. The effect of the optimisation by the energy function can be visualised by comparing Figure 2-1C (distortions before optimisation) to Figure 2-1D (after optimisation). Generally deformations of $\sqrt{E_L} > 0.1$ were considered bad reconstructions and since these mostly reflect the bad nature of the dissection, the retinae in question were not used for further analysis. Although there is some scatter in the deformation measure across the entire dataset, the mean deformation is 0.07 and only 27 out of 288 retinae exceeded 0.1 (Figure 2-1E). Since neonatal tissue is more fragile, and thus harder to dissect cleanly, we found that the deformation decreases as a function of age (Figure 2-1D).

Another measure of the goodness of the reconstruction can be found from the displacement of the OD from the retinal pole inferred by the reconstruction. When doing a composite plot of OD locations from all the adult retinae in this study, we found that there was scatter in the location (see Figure 2-1A-B). Moreover, we found that there is a correlation between the OD displacement and $\sqrt{E_L}$ (see Figure 2-1C). The average OD location was found to be at 3.7˚ latitude and 95.4˚ longitude.

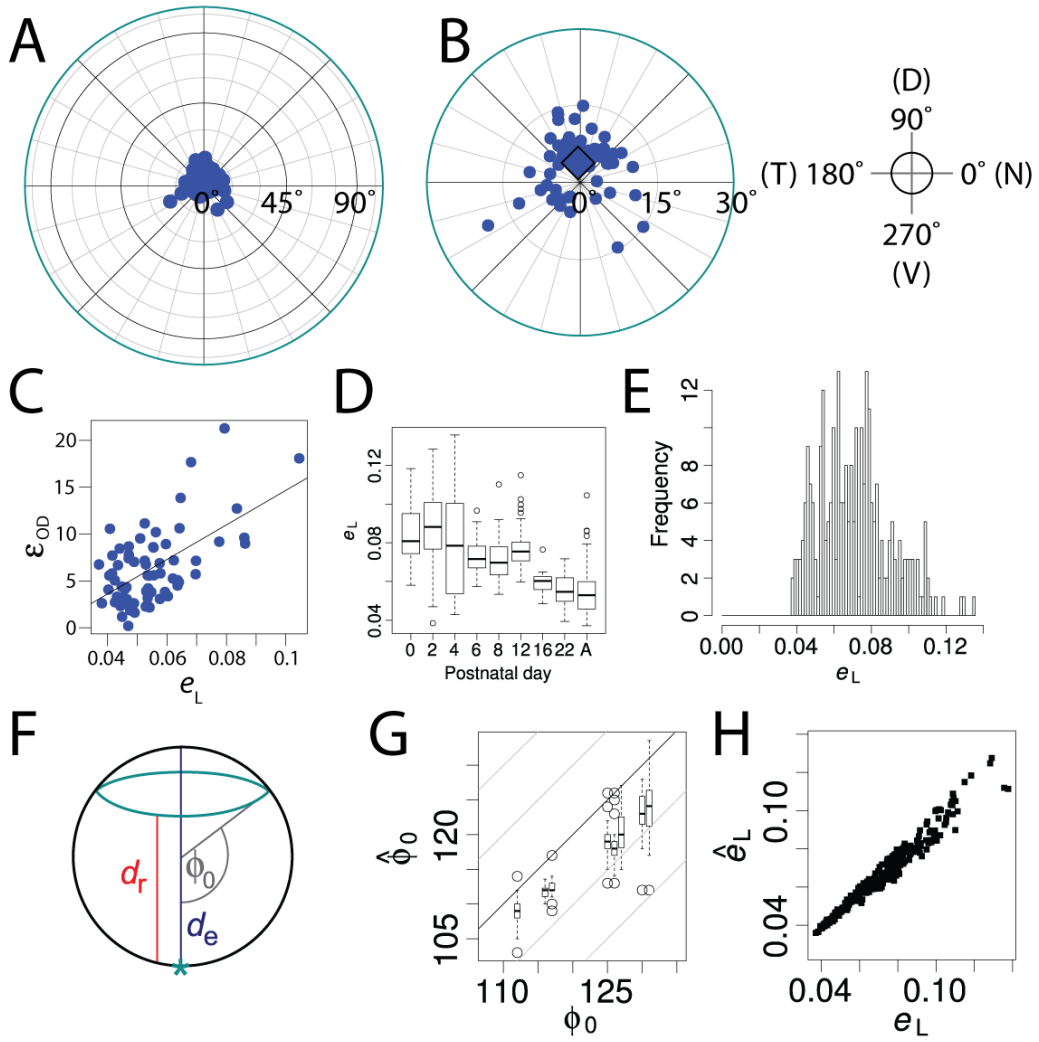

Figure 2-1: Evaluation of Retistruct algorithm

A, Azimuthal equilateral plot of ODs from 72 adult retinae. **B,** enlarged central region of plot in A to show the distribution of the ODs. Most are in the dorsal half. Diamond represents the Karcher mean (at 3.7˚ colatitude, 95.4˚ longitude). **C,** OD displacement from mean plotted against deformation of reconstruction ($R^2 = 0.35$, $p < 0.01$). **D,** Deformation of reconstruction as a function of age. Note the trend for higher deformation measures in young animals. **E,** Frequency histogram of deformation measure of 288 reconstructed retinae of various ages. **F,** Schematic illustrating measurements of retinal rim angle. d_r is distance from OD (*) to rim. d_e is diameter of eye ball. ϕ_0 is the angle of the rim (values for all ages are in Table 2-2). **G,** Rim angle inferred from optimising for lowest deformation measure ($\hat{\phi}_0$) relative to rim angle measured experimentally (ϕ_0). Inferred angle tends to be smaller than experimental value. **H,** Minimum deformation from optimised rim angle ($\hat{e}_L$) relative to deformation from experimentally determined rim angle (e_L). The analysis for this figure was done by David Sterratt and figures have been adapted from Sterratt, Lyngholm *et al.* (n.d.)

2.2.3 Measuring the shape of the retina

The shape and size of the retina varies significantly with age (Schmucker and Schaeffel, 2004), we therefore decided to measure the extent of the retina. I did this by measuring the distance from the retinal pole by the optic nerve head to the edge of the retina (see Figure 2-1F above for schematic and Table 2-3 below for values). Along with the diameter of the retina, this enables us to determine the rim-angle (φ_0) by calculating $\varphi_0 = \arccos(1 - 2d_r/d_e)$. An alternative to measuring the rim-angle is to calculate the optimal rim-angle by varying the rim-angle and using the value for φ_0 that has the lowest value for $\sqrt{E_L}$. This was done using the Retistruct software (Sterratt et al., n.d.) and when plotting the optimal values against the measured values (Figure 2-1G), we see that on average, the optimal value is slightly lower than the measured value. However, since the difference is small and consistent across ages, it is verifying that the measured value is reliable. Moreover, when the $\sqrt{E_L}$ from the optimal φ_0 is compared to the $\sqrt{E_L}$ from the measured φ_0 (Figure 2-1H), we found that the mean improvement in $\sqrt{E_L}$ by using the optimal φ_0 was 7.2%, with the biggest improvement being 19.1%.

Age	d_e (µm)	d_r (µm)	φ_0 (deg)	A (deg^2)
P0	1632 ± 17	1308 ± 17	127.1 ± 1.9	33,069
P2	2146 ± 13	1780 ± 29	131.2 ± 2.2	34,213
P4	2250 ± 9	1857 ± 20	130.6 ± 1.4	34,050
P6	2450 ± 41	1963 ± 25	127.0 ± 2.4	33,040
P8	2646 ± 1	2088 ± 34	125.3 ± 1.8	32,546
P12	2786 ± 15	2212 ± 65	126.0 ± 3.4	32,750
P16	2808 ± 17	2043 ± 16	117.1 ± 1.0	30,023
P22	2958 ± 35	2117 ± 44	115.6 ± 2.2	29,539
Adult	3160 ± 56	2161 ± 30	111.6 ± 1.9	28,220

Table 2-3 Measurements of eye diameters at different ages.

The distance from the back of the eye to the front edge of the cornea (d_e), the distance from the back of the eye to the rim of the retina (d_r) and the angle (φ_0) inferred from these measurements (see schematic in Figure 2-1F for clarification). n = 4 for each age (2 animals). A is calculated using Equation 2-11

2.2.4 Projection of retinal spherical coordinates to polar plots

Having reconstructed retinae into spherical coordinates, the next problem is how best to represent these. We have chosen to use three different methods of projecting the spherical retina to polar plots. Labelled cells in reconstructed retinae were plotted either in Azimuthal equidistant (Figure 2-2A) or area-preserving (Figure 2-2B) polar projections, depending on the measurements done.

The Azimuthal equidistant projection preserves distances, but not areas and is therefore useful in representing distances between objects on the retina, e.g. to measure distances between two foci of label. The transformations to an Azimuthal equidistant projection with φ_1 and λ_0 as the pole is given by (Yang et al., 1999; Weisstein, 2012a):

$$x = k' \cos\varphi \sin(\lambda - \lambda_0)$$
$$y = k'[\cos\varphi_1 \sin\varphi - \sin\varphi_1 \cos\varphi \cos(\lambda - \lambda_0)]$$

where $k' = \frac{c}{\sin c}$

and $\cos c = \sin\varphi_1 \sin\varphi + \cos\varphi_1 \cos\varphi \cos(\lambda - \lambda_0)$

Where c is the angular distance from the centre.

Equation 2-4 Azimuthal equidistant transformation

The Azimuthal (Lambert) equal-area projection is useful where relative areas are more important than the absolute distances, e.g. when representing isodensity contours on the retina. The transformation to an Azimuthal equal area projection with φ_1 and λ_0 as the pole is given by (Yang et al., 1999; Weisstein, 2012b):

$$x = k' \cos\varphi \sin(\lambda - \lambda_0)$$
$$y = k'[\cos\varphi_1 \sin\varphi - \sin\varphi_1 \cos\varphi \cos(\lambda - \lambda_0)]$$

where $k' = \sqrt{\frac{2}{\sin\varphi_1 \sin\varphi + \cos\varphi_1 \cos\varphi \cos(\lambda - \lambda_0)}}$

Equation 2-5 Azimuthal equal-area transformation

2.2.5 Projection to visual space

In order to project the spherical retinal coordinates to visuotopic space, or vice versa, it is necessary to have a good understanding of the shape and optics of the eye, specifically how light is refracted through the lens. Although there are several models of the mouse eye available (Remtulla and Hallett, 1985; Schmucker and Schaeffel, 2004), none of them account for the refraction of the full spectrum of light through the lens. We therefore approximated the path of the ray, such that a ray aligned with the optic axis will pass straight through the lens without being refracted, whereas a ray that has a 90˚ incidence angle with the lens will be refracted to the edge of the retina for any shape of retina in such manner that an angle φ on the retina is equivalent to the angle γ in visual space, independent of φ_0 (See Figure 2-2E). Using these approximations, the locations of the points on the retina at the optic axis are first projected to equivalent points through the centre of the eye and then the rest of the retina is projected onto a notional large concentric sphere about the eye representing visual space. Following these coordinate transformations, points on this "celestial" sphere are measured in terms of elevation, the angle above the horizontal and azimuth, the angle made between the point's meridian plane and the zero meridian plane, i.e. the vertical plane containing the long axis of the mouse. By convention, projections of visual space are presented as though the mouse is sitting facing the observer, so that the azimuth angle is positive in the left visual field (Dräger, 1978; Dräger and Olsen, 1980; Coleman et al., 2009).

In order to represent this "celestial" hemisphere in front of the mouse, we chose to use an Orthographic projection, as this is useful for representing a hemisphere (Figure 2-2C).

The Orthographic projection preserves distances quite well. Areas, however, are not preserved. The transformation from spherical coordinates is given by (Yang et al., 1999; Weisstein, 2012c):

$$x = \cos\varphi \sin(\lambda - \lambda_0)$$
$$y = \cos\varphi_1 \sin\varphi - \sin\varphi_1 \cos\varphi \cos(\lambda - \lambda_0)$$

Equation 2-6 Orthographic projection transformation

Where φ is latitude and λ is the longitude. φ_1& λ_0 are the reference latitude and longitude for the centre of the projection.

The sinusoidal projection is an equal-area projection of an entire globe, which means that the areal distortions are minimised. However, this is at the compromise of angular accuracy and increased distortions in distance measurements away from the equator and central meridian, as can also be seen in Figure 2-2D. The transformations of this projection are given by (Yang et al., 1999; Weisstein, 2012d):

$$x = (\lambda - \lambda_0)\cos\varphi$$
$$y = \varphi$$

Equation 2-7 Sinusoidal projection transformation

Where φ is latitude, λ is the longitude and λ_0 is the central meridian.

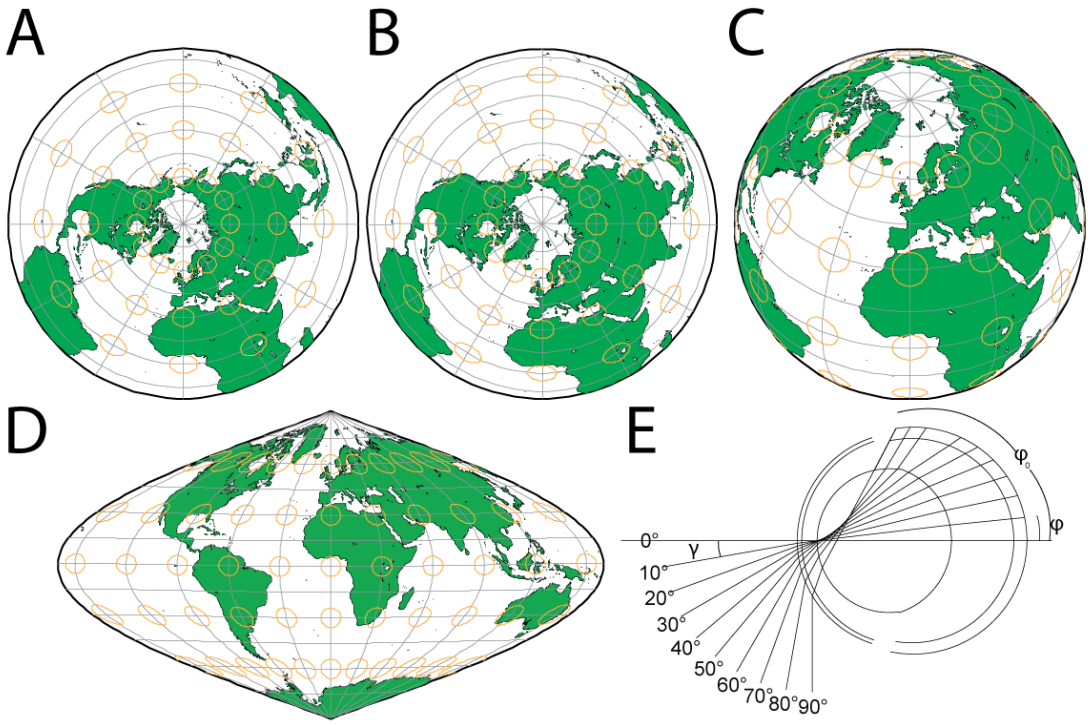

Figure 2-2: Map projections for retinotopic and visuotopic coordinates

A-B, Azimuthal (polar) plots are used to represent the reconstructed retina on a flat surface, as these facilitate the projection of a more than a hemisphere. Plots here have a φ_0 of 22˚ (equivalent to an adult retina). However, using this projection method, it is only possible to preserve either distance, by using an equidistant plot (A), or area, by using an equal-area plot (B), but not both. As can be seen by the size of the orange circles, which are of identical shape and size on the sphere. **C,** For representing a hemisphere of visual space, the plot with the least distortions is the orthographic plot, which here is rotated to show the area above the pole. The downside of this projection method is that it cannot be used to represent more than a hemisphere, and can therefore not be used for retinal plots. **D,** The sinusoidal projection is useful for representing a full sphere, such as that of the entire visual field, but does introduce some distortions around the periphery. This example is plotted for the 310˚ of mouse vision (notice that New Zealand is missing as it's behind the mouse). **E,** Schematic of a standard adult eye, illustrating how the lens refracts rays reaching the retina, so that the angle ϕ on the retina represents the angle γ in visuotopic coordinates. ϕ_0 in this example represents the colatitude of the retinal rim. I.e. for an adult retina this means that it is possible to project a visual field of 180˚ to the 224˚ of the retina.

2.3 Analysing the Retina

Although the transformations above are essential for representing the retina in print, all of the analysis was done using the original spherical coordinates and the distortions involved in the transformations will therefore not impact on the analysis, but merely influence the appearance of the examples. The mean location of the data points on the retina was established by using the Karcher mean, which finds the point with latitude $\bar{\varphi}$ and longitude $\bar{\lambda}$ that has the lowest sum of squared distances to a group of points (φ_i, λ_i) on the surface of a sphere as given by:

$$(\bar{\varphi}, \bar{\lambda}) = \arg\min_{(\varphi,\lambda)} \sum_{i=1}^{N} l^2(\varphi, \lambda, \varphi_i, \lambda_i)$$

Equation 2-8 Karcher mean

2.3.1 Isodensity Contour analysis

To plot isodensity contours to different levels of the density distribution, we must first find the densest area of label. For the retinae that are completely sampled, the density was found by using Kernel density estimation (KDE) for data points on a sphere by using the following kernel function:

$$F_{(\varphi,\lambda,\varphi_0,\lambda_0;\,\kappa)} = \frac{\kappa}{4\pi \cosh \kappa} \exp(\kappa \cos l(\varphi, \lambda, \varphi_0, \lambda_0)) = \frac{\kappa}{4\pi \cosh \kappa} \exp(\kappa \vec{r} \cdot \vec{r}_0)$$

Equation 2-9 Kernel Density Estimate

And $\hat{f}_{(\varphi,\lambda;\kappa)} = \frac{1}{n}\sum_{i=1}^{n} F((\varphi, \lambda, \varphi_i, \lambda_i; \kappa)$

where κ *is the density parameter with* $\vec{r}$ *and* $\vec{r}_0$ *representing the Cartesian coordinates of the spherical coordinates* (φ, λ) *and* (φ_0, λ_0) *on the sphere. The density at the point* (φ, λ) *is found by using the function* $\hat{f}_{(\varphi,\lambda;\kappa)}$

To calculate the density measures for plotting contours on partially sampled retinae (see section 2.5.3), we have had to use a Kernel Regression Estimation (KRE) method that interpolates the missing data points from unsampled areas by using a modified Nadaraya-Watson estimator, according to:

$$\hat{y}_{(\varphi,\lambda;\kappa)} = \frac{\sum_{i=1}^{n} F((\varphi,\lambda,\varphi_i,\lambda_i;\kappa) y_i}{\sum_{i=1}^{n} F((\varphi,\lambda,\varphi_i,\lambda_i;\kappa)}$$

Equation 2-10 Kernel Regression Estimate

κ is set as the minimal summed squared error $\sum_{i=1}^{n}\left(y_i - \hat{y}_i(\varphi_i,\lambda_i;\kappa)\right)^2$,
where $\hat{y}_{\iota(\varphi_i,\lambda_i;\kappa)}$ *is the KRE of* y_i

Having density estimates for the entire retina, we can plot isodensity contours by excluding 5%, 15%, 25%, 50%, 75% & 95% of the least dense cells, which enables us to calculate the size of the isodensity contours in degrees squared. However, as the size of the retina changes with age, the area contained within each contour is then normalised to the size of the retina, which is calculated by using:

$$A = 2\pi(1 - \cos\varphi_0\pi/180)) \times (180/\pi)^2$$

Equation 2-11 Retinal area

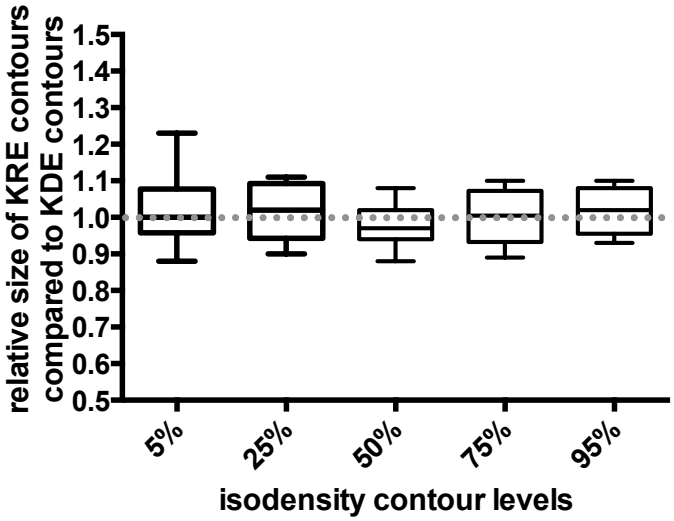

Figure 2-3: Comparison of contouring methods

To verify that there is no difference between the partial and complete sampling strategies and no discernible difference between the contouring methods, 10 retinae were sampled using both strategies and the respective contouring algorithm was used to plot isodensity contours. Next the size of the partially sampled KRE contours was normalised to the fully sampled KDE contours and plotted. Bar represents the mean and the boxes show Standard Deviation. The Error bars represent the spread of the data. As can be seen from the plot, no bias is present in either direction.

2.4 Orienting the Retina

2.4.1 Injection of Dextrans into the dLGN

To orient the retina we needed a way of labeling the entire ipsilateral projection in the ventral-temporal crescent (See Figure 3-3) and thereby establishing the location of the vertical meridian by aligning the binocular zone in visual space (Figure 3-4).
Animals were anaesthetized using Ketamine/Xylazine (for doses, see Table 2-1). For injections into the dLGN, a skull flap was drilled and cortex was aspirated using suction to reveal the thalamus either unilateral or bilaterally. Once the thalamus was revealed, Fluorescein-conjugated dextran (Fluoro-Emerald) or tetramethylrhodamine-conjugated dextran (Fluoro-Ruby) (5% w/v; 10,000MW; D1820, D1817; Invitrogen) was pressure-injected into right and left thalamus, respectively (for schematic see Figure 3-3A). Glass pipettes used for injection had a 120 µm internal diameter and tip diameters of 30-100 µm. Multiple injections were made into the thalamus with total volumes injected into one thalamus ranging between 50 nl and 250 nl. Following surgery, the cavity from aspiration was filled with absorbable gelatine sponge, the skull-flap replaced and the skin sutured. Animals were allowed to recover and left for 24-48 hours before perfusion fixation

2.4.2 Marking of muscle insertions onto the eye

To investigate the orientation of the eye, the insertions of the superior, inferior and lateral rectus muscles were marked onto the retina (Figure 3-1) by passing a needle coated with Fluoro-Emerald or Fluoro-Ruby (5% w/v) through the sclera into the retina at the centre of the muscle-insertion prior to dissecting the retina, as described above in section 2.1.5

2.5 Investigating topography using retrograde tracing from the SC

2.5.1 Injection of Fluorescent Microspheres.

5-10nl of red or green fluorescent latex microspheres (RetroBeads; Lumafluor, USA), diluted 1 in 2 with saline solution, was injected using a glass pipette with an inner diameter of 120 μm and an outer diameter of 800 μm (Plowden & Thompson, UK) with a 10-20μm diameter tip size, pulled on a Flaming/Brown micropipette puller (Sutter Instruments, USA). The red and green beads were pressure-injected into the left superior colliculus at varying ML and AP positions with reference to medial and posterior edge of the superior colliculus and were of varying AP or ML separations of between 50μm and 2000μm. All injections were made using pressure and performed through an epifluorescent microscope (Leica Microsystems, Germany) to visualise the injection sites. In P0 and P2 animals, injections were made transcranially. In animals between P4 and P22, a craniotomy was performed and injections were made through the dura into the superior colliculus. For adult animals and for anterior injections in older neonatal animals (P8-P22), a craniotomy was performed and the cortex was aspirated to reveal the surface of the superior colliculus. All injections were placed with reference to the vasculature at the midline and posterior border of the SC and injections were angled to be perpendicular to the surface of the SC. One assumption of the bead injection analysis is that the beads are taken up equally by all cell types and without spatial bias. Procedures may have been performed with a variation of ±8 hours.

The fluorescent microspheres are taken up by the axon terminals and transported to the cell soma in the retina, where the microspheres fill up the soma, which can therefore be visualised using epifluorescence microscopy (Katz et al., 1984; Katz and Iarovici, 1990). The weakness of this method is that there is a possibility of the microspheres being taken up by axons passing through the area (Katz et al., 1984). To prevent this injections were limited the superficial layers of the SC as not to penetrate into the stratum opticum (SO), where there is a possibility that the beads might be taken up by fibres damaged by the injection. Injections that extended through the SO were not used in the analysis. The label in the superficial layers should therefore only be taken up by axons with branches into the area of the injection site.

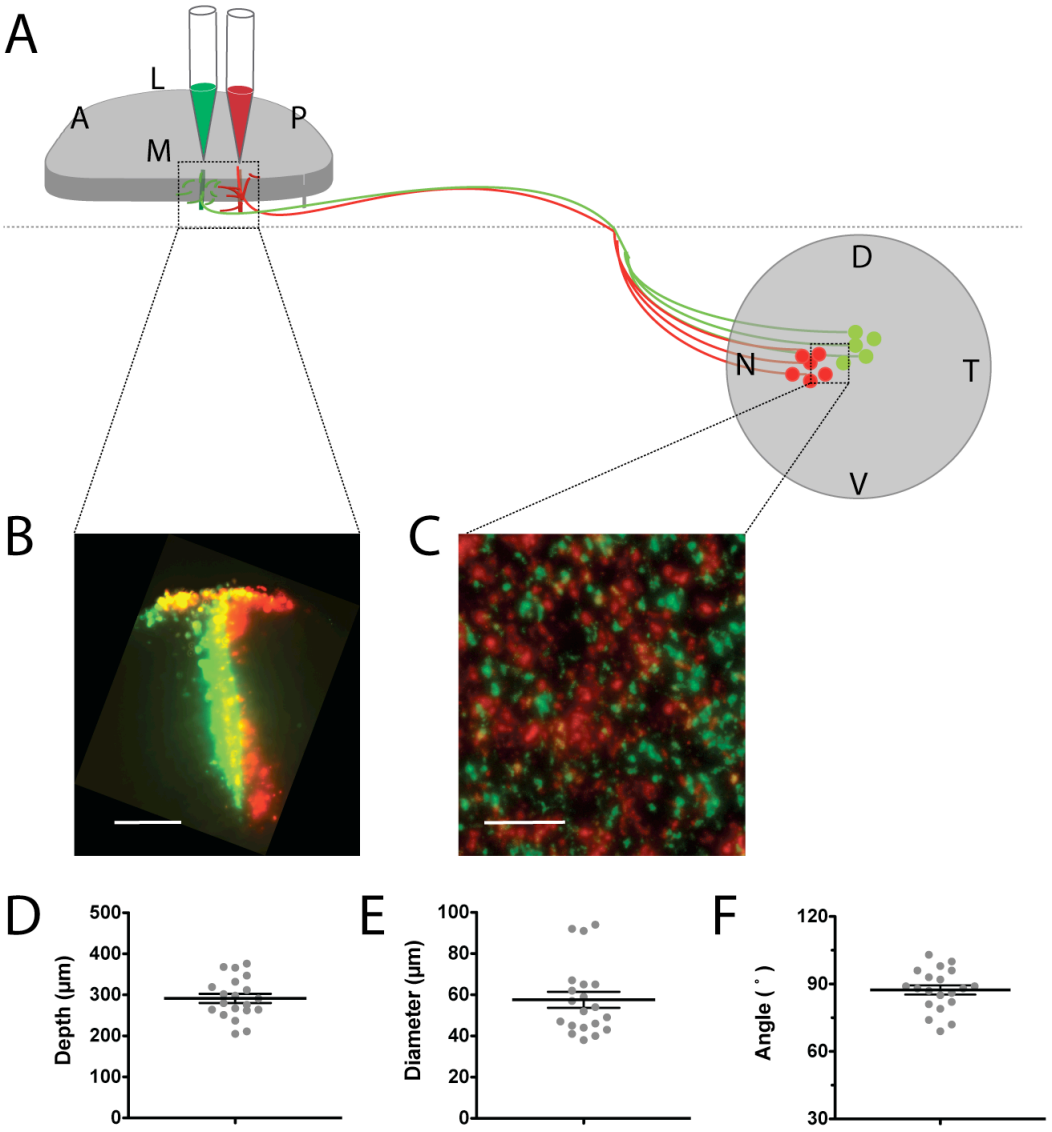

Figure 2-4: SC bead injections

A, Schematic of injection procedure and resulting label. Red and green retrobeads are injected sequentially into the superficial layers of the SC with varying mediolateral or anteroposterior separations. **B,** Image of 150µm thick parasagittal section through the SC of an adult animal showing the paired injection sites through the depth of the SC SGS. Scale bar is 100µm. **C,** Image of resulting label in retina from injections in B. Scale bar is 100µm. **D-F,** Measurements of injection sites from sections as in B, showing depth (D) and diameter (E) of injections and the angle relative to the surface (F). Line is mean and error bars are SEM.

2.5.2 Collicular Analysis.

After having removed the eyes, the skull was cut open, the whole brain was carefully removed and the superior colliculus exposed by cutting away cortex or removing gelatine sponge if cortex was aspirated during surgery.

Brains were imaged at 4.6x using a Leica epifluorescence photomicroscope. The AP position of the injection site was determined by measuring the distance from the back of the SC and the ML position by measuring distance from the midline using ImageJ. Subsequently, a vector connecting the paired injections was drawn pointing toward the more posterior injection in animals with AP separations. Animals where there was a ML offset of more than 500μm were not used in the analysis of paired injections, but treated as single injections. Subsequent to being imaged, the brains were embedded in 2% gelatine; post fixed in 4% paraformaldehyde and sectioned in 150μm slices parasagittally for injections separated along the AP axis and coronally for injections separated along the ML axis. The slices were mounted in Fluoromount and imaged at 10x magnification using filters for TRITC and FITC to assess the angle, diameter and depth of the injections and to verify that the injections did not extend into the stratum opticum. This analysis was done for all the adult animals and for a subset of each age. For this purpose, some brains were also imaged whole using a 2-photon microscope (Prairie Technologies, USA). However, due to the depth and brightness of the injection sites, the most reliable way of determining the depth, diameter and angle of the injection was from sectioned material.

Age	AP size	± SD	ML size	± SD
0	1910	104	1800	140
2	1920	92	1860	105
4	2000	61	1800	93
6	1980	89	1850	160
8	1890	98	1840	91
12	1920	64	1890	109
16	1970	31	1880	70
22	1970	54	1860	71
60+	2072	42	1908	60

Table 2-4 Measurements of the size of the SC through development

Measurements were done from images of whole mount brains with the cortex removed. Because of the medial and posterior curvature of the SC, these measurements are probably a slight underestimate. The measurements represent the size at the widest (central) and longest (medial) part of the SC.

2.5.3 Retinal Analysis.

Retinae were examined using a Zeiss epifluorescence microscope with excitation filters for red (580nm) and green (510nm) wavelengths in a Camera Lucida setup using in-house software. To prevent emission of red in the green channel, a band-pass filter of 545nm was used to plot green label. For the sampling, a 200x200µm grid was superimposed onto the retina, which was used for aligning the high-power views across the retina. The outlines of red and green fluorescent cells were either traced using a 1 in 4 sampling strategy using a 200x200 µm sampling box, or sampling every grid point. The retinal outline was traced at low magnification (2.5x) and the cells were traced at high magnification (25x) using neofluor lenses.

The presence of double-labelled cells was defined as cells marked in both channels independently that are separated by no more than 10 pixels (~5µm). Once picked out by the software, the cells were visually verified to have similar cell morphologies. The retinae were initially analysed using Systat (Systat Software, USA) and Matlab (Mathworks, USA) to find the extent of label and the 10% and 20% isodensity contour lines using kernel density estimates. In sparsely sampled retinae, this was done by

interpolation between sampled grid points to simulate a fully analysed retina. Following the isodensity contour analysis, the centre of the 20% contour was found and used to plot the position of the label. The relative separation of the centres of gravity of the red and green label was also measured, for comparison with the corresponding separations in the SC. However, due to the variability in dissections this proved to not be the optimal way of determining the correct locations on the retina. As a result of this, we developed the Retistruct algorithm, as described in section 2.2.1 . One consequence of this was that all the analysis described above had to be done in spherical coordinates. The resulting analysis methods are described above in section 2.3.

2.5.4 Nearest-Neighbour Analysis.

The Nearest Neighbour analysis was performed using Matlab to determine the percentage probability that any two adjacent cells have the same colour. This probability is a good measure for order in the topographic projection, since in a fully ordered topographic map two adjacent cells in the retina would also be adjacent in the SC.

The distances from a cell to its neighbours are calculated using the great angle distance l_i (Equation 2-2) and its nearest one is found. $l_{min} = \arg\min(l_i)$. Next the proportion of cells that have the same and opposite colour as their nearest neighbour is calculated for each colour (NN_{same} and $NN_{opposite}$, respectively) and the nearest neighbour measure is the mean of the values for both colours, as given by:

$$\overline{NN} = \frac{NN_1 + NN_2}{2} \qquad \text{where} \qquad NN = 1 - \left(\frac{NN_{opposite}}{NN_{same}}\right)$$

Equation 2-12 Nearest Neighbour function

A nearest-neighbour (NN) value of 1 therefore signifies a fully ordered projection, whereas a value of 0.5 signifies an unordered projection. The measure, however, can be skewed if there are more labelled cells of one colour than the other, giving values of

<0.4 To solve this, data simulations of varying ratios of label were done to show that if the ratio of label from the two injections is less than 7 then the mean NN of the two injections is representative of the overall NN value of the retina. Therefore, retinae with a label ratio of >7 were not used for this analysis.

Curve fitting of Nearest Neighbour data

To quantify NN, data points were plotted as a function of the separation of the paired injection sites in the respective SC and fitted with the following logistic function, which was initially used to describe population growth (Weisstein, 2012e) and has since been widely used for description of both psychometric data and pharmacological dose-response curves.

$$y = 1 + \left(\frac{-0.5}{1 + \frac{x}{\tau^{\kappa}}} \right)$$

Equation 2-13 logistic curve

Where x is the injection site separation, $x_{y=0.9}$ is the value at which the label is 90% separate, τ is the inflection point and κ is the steepness of the function

This function will yield an S-shaped logistic curve that generally has an initial period with no increase (the minimum asymptote), which is followed by an exponential increase to an inflection point, from where the curve turns to start saturating before eventually stabilising at saturation (the maximum asymptote). In order to describe the data from the nearest neighbour analysis, the classical 4-parameter logistic curve has been modified to a 2-parameter function (Equation 2-13) by constraining the asymptotes so that the minimum asymptote is at 0.5 (complete overlap of label) and the maximum asymptote is at 1 (complete segregation of label). This also means that the inflection point is always at at the midpoint between the base level and saturation (y=0.75). A nearest neighbour (NN*)* value of 0.9 is defined as being two separate foci of label, as this value represents the saturation point of the fitted function (Equation 2-13) and thus signifying a precise projection.

2.6 Software Used for Analysis

Retinae were reconstructed and projected using custom-made software Retistruct (Sterratt et al., n.d.), which has been implemented in R (R-Project, available at http://www.R-project.org/). This software was developed by David Sterratt (the University of Edinburgh). The isodensity contour analysis described above was also performed using this software.

Retinal flat-mount images were acquired using a Zeiss AxioPhot2 microscope and initially processed using the associated AxioVision software (Zeiss). Collicular whole-mount images were acquired using a Leica stereoscope and initially processed using Volocity software (Perkin-Elmer). Following acquisition, images were further processed using the Fiji release of ImageJ (NIH, USA). Specifically, the stitching of high-power retinal images into retinal whole-mounts was performed using the MosaicJ plugin. Thresholding and detection of label was done using built-in functions for image adjustment and processing. ImageJ was also used for marking up the edges of the retina in images of flat-mounted retinae before parsing the images in png format and associated ImageJ ROI files to Retistruct.

Statistical analysis and graphs were mainly generated using Prism (v.5.0a; Graphpad Software) and Matlab (r2012a; Statistics Toolbox, Mathworks)

The Nearest Neighbour values were calculated using custom-made routines for finding nearest neighbours in spherical coordinates, which have been implemented in Matlab. These routines were partially based on code from the Mathworks repository (URL). Specifically code for finding nearest neighbours on a sphere (URL). The curve fitting and statistical analysis of the Nearest Neighbour data was also done using Matlab (r2012a; Curve Fitting Toolbox, Mathworks) with the equations in section 2.5.4.

Diagrams and figures were generated by using Illustrator and Photoshop (CS5; Adobe Systems).

2.7 Statistical Analysis

2.7.1 Comparing datasets

The data from isodensity contours was firstly tested for normality using a Kolmogorov-Smirnoff (KS) test and if the Dallal-Wilkinson-Lilliefor (DWL) *p*-value was larger than 0.05, then the dataset was deemed as being normally distributed around the mean. For normally distributed datasets the datasets were compared using One-way ANOVA with a Bonferroni post-hoc test with α=0.05. If p <0.05, then the datasets were deemed as being significantly different. Throughout this thesis, the levels of significance are defined as follows: p<0.05 = *; p<0.01 = **; p<0.001 = ***

In cases where datasets were not deemed as being normally distributed around the mean (KS-DWL p<0.05), then a non-parametric test is needed to be able to correctly compare the datasets. In these cases a Kruskal-Wallis (KW) test with a Dunn's post-hoc test was used to compare the datasets, as this test assume neither normal distribution of label nor assume equal variances.

2.7.2 Analysing NN Curve fits

Establishing the optimal function for describing a dataset is not straightforward. There are, however, several methods for evaluating the goodness of fit for any given function.

To evaluate the fits to the nearest neighbour data when plotted as a function of injection site separation using the logistic function described above (Equation 2-13).
Fits were generated using a bootstrap method (Foster and Bischof, 1987; 1997) implemented in Matlab (r2012a; Matlab Curve Fitting Toolbox, Mathworks).

The conventional way is to report the coefficient of determination (R^2). If R^2 is close to 1.0, then the fit is good and gives a reasonable description of the data that can be used to make predictions. If the fit is <0.5, then another fit should be considered. However, due to the constraints of this method not giving accurate values for functions with a slope close to 0, I have also opted for reporting the sum of squared errors (SSE) of the

residuals, which describes the spread of data around the fitted curve. Since the SSE represents the mean distance from any point to the fitted function, a perfect fit will have an SSE value of zero. In general, a reasonable fit, which can be used to make confident predictions from the function is one where SSE<0.1. One potential problem with both R^2 and SSE as measures of goodness of fit is that neither of them account for any asymmetries in the residuals of the fitted function. For this reason, the residuals are always showed next to any fits, so that the data can be assessed visually as well (For an example of these plots, see Figure 3-6J).

In order to compare the fits of different datasets, to establish whether there are any significant differences between the fits, I have used a two-tailed analysis of the slope using the 95% confidence intervals.

Chapter 3 Anatomy of the Adult Retinocollicular Projection

3.1 Introduction

The mature visual system features complex circuitry to convey and compute visual inputs. At the simplest level, the primary projections from the retina are essentially topographic in nature. Since the nature of this topography is so crucial for understanding vision, this chapter looks at the precision in the mature retinocollicular projection and how topography can be examined by using anatomical techniques.

In studying the visual system, there are inherent disparities between the coordinate systems used in physiological and anatomical studies. This disparity arises as physiological studies mostly rely on presenting stimuli on a flat screen that is tangential to the visual space of the mouse, whereas anatomical studies rely on anatomical markers and features. The ability to compare experimental data from physiological and anatomical studies is crucial in being able to determine the relation between the two and ultimately their relation to actual visual space. For these reasons we have developed algorithms for translating these anatomical coordinates onto visuotopic coordinates by reconstructing dissected and flat-mounted retinae into their original spherical shape. Not only does reconstructing retinae enable the translation into visuotopic coordinates, it also controls for changes in the shape of the retina with age and minimises variability of retinal dissections, thereby making it possible to standardise retinal space (Sterratt et al., n.d.).

In this chapter, I show data that verifies several aspects of the algorithms by relating them to previous studies and then proceed to use this software to firstly solve several problems relating to the orientation of the eye in visual space and secondly to create a standard retinal space. This standard retinal space is then used for mapping the topography of the retinocollicular projection in adult black C57BL6/J and white CD-1 mice. In this study we have used retrograde transport of fluorescent beads from discrete injections into the SC to study precision and topography in the retinocollicular

projection. This approach firstly enables thorough quantification of the projection and makes it possible to examine even the projections from across the whole retina.

3.2 Results: Orienting the retina

The mouse retina is remarkably uniform and, apart from the optic disc, lacking in distinguishing features. For this reason there is no obvious way of verifying the orientation of the retina. In the past, several ways of determining the orientation of the retina have been used. In adult animals, a good way of defining dorsal is to make a cut into the cornea orthogonal to the angle of the head, however, since the angle of the head changes significantly during development, this method is not reliable for developmental studies. Another method is to use the insertions of the extraocular rectus muscles into the globe of the eye (e.g. Plas et al., 2005), however, as I will demonstrate, this is neither an easy nor very reliable method. A further method is to assume that the orientation of the whisker-rows is nasal (Hindges et al., 2002), the problem here being that as the animals grows, this changes considerably. Moreover, since mice have their nose pointing down, this may represent anatomical nasal, but is not a reliable marker for establishing the visual axes of the mouse. Considering all the alternative methods, the method we chose is to make an orienting cut into the cornea at the centre of the nictitating membrane and define this as the nasal retina. The location is easy to identify at all postnatal ages and approximates the angle of the eyelids. Since all the measures vary slightly, the questions that remain to be answered are how this fiducial mark relates to the insertion of the eye muscles and to the visuotopic projection of the retina.

3.2.1 Muscle insertions

To examine the orientation of the eye and to verify the reliability of the nictitating membrane cut, we labelled the locations of the insertions of superior, lateral and inferior rectus into the globe of the eye onto the retina (Figure 3-1A; see Methods for procedure). The retinae were oriented by enlarging the initial nasal cut through the nictitating membrane towards the optic disc. Since the size and direction of this subsequent cut was variable, the initial peripheral incision was used as the nasal reference point. The retinae were then reconstructed and plotted in an azimuthal equidistant polar projection and the vectors connecting the insertion points and the optic disc were plotted (Figure 3-1B). Once in a standard space, the muscle insertion points (n=33) from all the retinae (n=17) were plotted in the same plot and the vectors connecting the Karcher mean of each muscle insertion and the Karcher mean for the optic disc location were plotted (Figure 3-1C) with the result that the mean angle of the lateral rectus vector, at 178˚, is directly opposite the nasal cut. The superior rectus is at 91˚ and the inferior rectus is at 277˚ (where nasal is at 0˚). The variability in muscle insertion locations is due to difficulties in determining the middle of the insertion, and as a result the longitudinal distribution of the label approximately reflects the width of the muscle (Shah and Crair, 2008a).

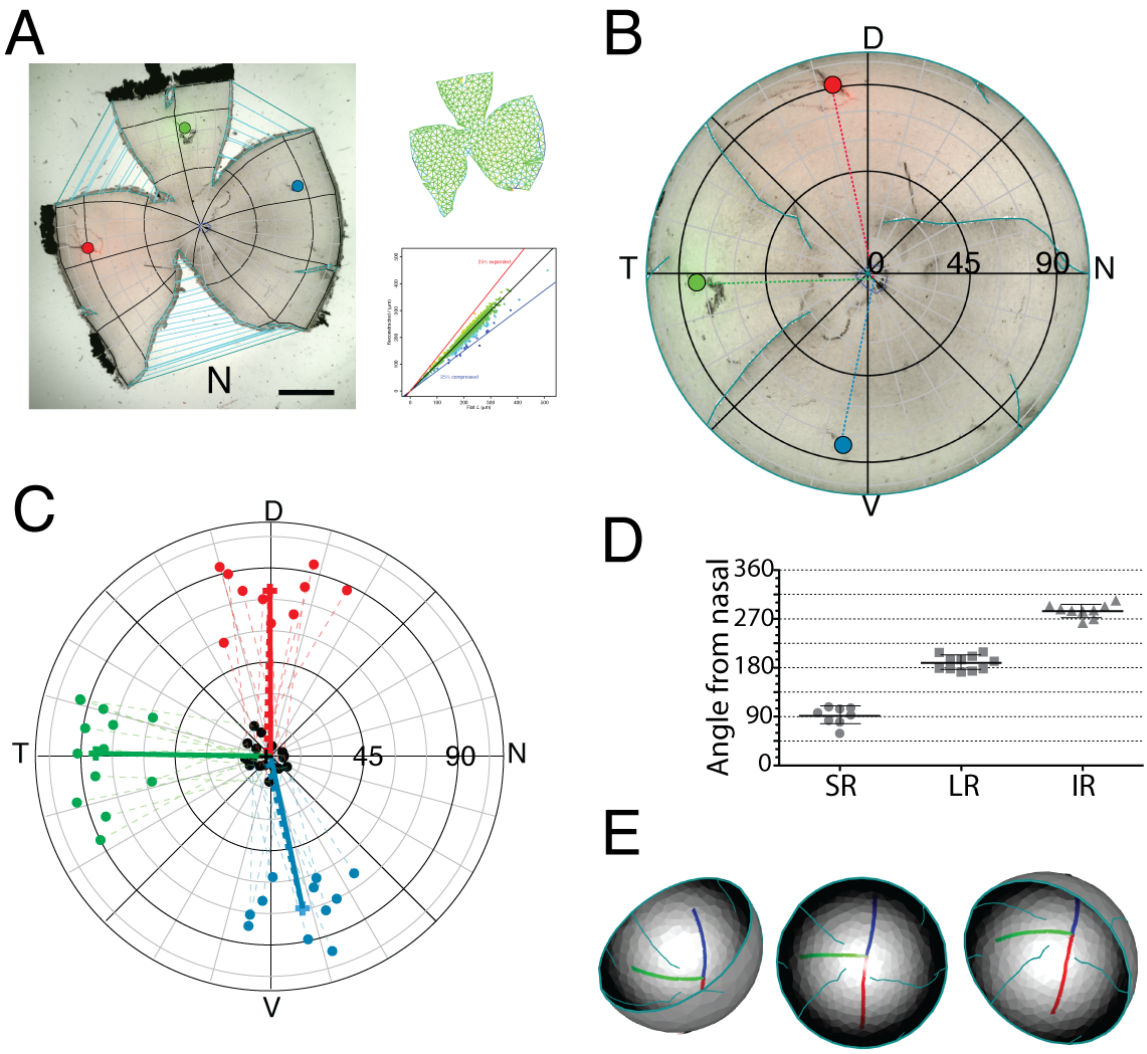

Figure 3-1: Muscle insertions

A, Retinal flat-mount with muscle-insertions for superior (red), lateral (green) and inferior (blue) rectus muscles labelled. Blue lines indicate the stitching of the cuts. N denotes nasal cut. Scale bar is 1 mm. Superior right plot is of the distortions introduced by stitching the retina and the inferior plot represents the expansion and contraction of all segments. (See methods Figure 2-1 for explanation) **B,** Azimuthal equilateral polar projection of flat-mount in A with vectors connecting muscle insertions to the optic disc. **C,** Composite polar plot of 12 retinae, reconstructed using same method as in B. Dashed lines are vectors for individual retinae and solid lines connect the Karcher mean insertion to the mean OD. **D,** Distribution of angles of muscle-insertion vectors for superior rectus (SR), lateral rectus (LR) and inferior rectus (IR). Line represents the mean and error bars are SD. **E,** Mean vectors in C represented on the surface of the retinal hemisphere.

3.2.2 S-Opsin expression

Another method of examining the orientation of the retina is to look at the distribution of different cell types. The different photoreceptor cones have been reported to have quite distinct distributions. For example, cones expressing only medium wavelength opsin have been reported to be located mainly in dorsal retina, whereas cones expressing short wavelength opsin (S-opsin) are more frequent in ventral retina (Szél et al., 1992; Applebury et al., 2000; Haverkamp et al., 2005). Therefore, in order to verify the orientation of our retinal dissection, retinae were stained with a polyclonal antibody against shortwave opsin (S-Opsin), and as can be seen from Figure 3-2E, S-opsin cones have a very distinct distribution pattern in the retina, with high density ventral, low density dorsal and an abrupt transition. The images in Figure 3-2A-B highlight some of the difficulties in obtaining consistent staining of large tissues, such as the retina. Especially when penetrance differs between peripheral and central retina (cf. the staining for heavy neurofilament (SMI-32) in Figure 2-1). However, when images are thresholded individually prior to stitching it is possible to consistently detect and quantify the label irrespective of bleaching and differences in staining intensity. Examples of this are shown in Figure 3-2C-D, where individual cone locations are plotted in blue. This method reasonably reliably detects individual cones based on thresholding. Although there are some slight inaccuracies, I find that using this method is consistent with measuring the density from individual high-power images, such as those in Figure 3-2E. Moreover, I find that the density is in the order of 10,000 cells/mm^2 in ventral retina and between 500-600 cells/mm^2 in dorsal retina, which is consistent with results from Haverkamp et al. (2005).

The S-opsin density transition has previously been shown to be at an angle to the retinal nasotemporal axis (Szél et al., 1992), which would make it a potential marker for orienting the retina, if this angle can be determined. When retinae are stained with this antibody and reconstructed, the transition from high to low density lies at an angle of 15.1±7.2˚ (*n=11*) to the nasotemporal axis with the transition being ventral to the level of the optic disc at the nasal pole and dorsal at the temporal pole. The transition is generally dorsal to the optic disc, but within the uncertainty involved in reconstructing the retina, it is coincident with the optic pole (offset: 4.3±2.2˚) (Figure 3-2 C-D), which is consistent with earlier reports by Szél et al. (1992) that this angle may correspond to the horizontal meridian (see Discussion).

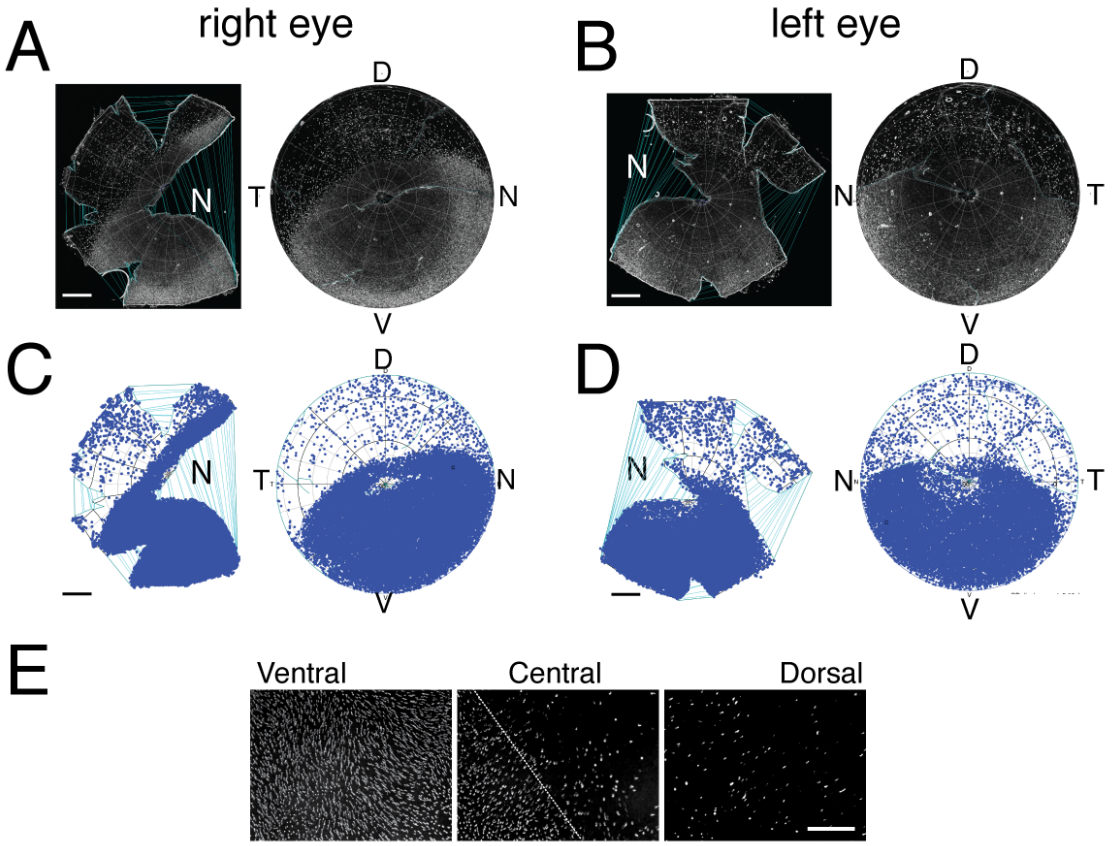

Figure 3-2 S-opsin distribution

A-B, Stitched images of retinal flat-mount and reconstructed azimuthal equidistant plots of left and right retina from the same animal stained with antibody against short wavelength opsin. **C-D,** Detection of label in A-B, to clearly show the transition from high ventral density to low dorsal density. Scale bars in A-D are 1 mm. **E,** High-power images of label from dorsal, central and ventral retina in A, to show the different distributions of staining. Dashed line is the line of the transition. Scale bar is 100µm.

3.2.3 Measurement of ipsi- and contralateral retinal projections

Reconstructing the retinae of individual animals that have had bulk unilateral injection of retrograde tracer injected into primary subcortical visual areas enables comparisons of decussation patterns across animals. The use of standard retinal space allows both the assessment of individually incomplete bulk injections and also the population averaging of such injections. The reconstruction method has been used to assess the crossed and uncrossed projection from the retina to the dLGN across multiple animals. To label the projection, the dLGN was filled with dextran-tetramethylrhodamine (Fluoro-Ruby) or dextran-fluorescein (Fluoro-Emerald), as illustrated in Figure 3-3A (see Methods for details). While most injections were unilateral, several bilateral injections were also made (e.g. Figure 3-3B). The retinae were dissected as described and the Retistruct program was used to reconstruct the retinae. Retinae were analysed either through the Camera Lucida based Scope program at 20x (e.g. Figure 3-3E) or following imaging at 10x using ImageJ (e.g. Figure 3-3B).

To quantify the distribution of label in the retinae, kernel density estimates (KDE) of the underlying probability of data points appearing at any point in the retina was calculated (Equation 2-9). These KDE measures are then represented by plotting isodensity contours excluding 5% of the points with the lowest density (Figure 3-3C-D; Methods). In cases where cells were only counted within defined boxes on the flattened retina, a different contouring approach, kernel regression (KR) (Equation 2-10) was used as the source for the contouring algorithm, but with the same isodensity contours plotted as for the KDE contours. As expected, this analysis shows that the label from the ipsilateral projection is restricted to the ventrotemporal crescent, whereas label from the contralateral projection is distributed across most of the retina.

To measure the extent of the ipsilateral projection, composite plots of data from 12 different animals were made, which shows that the average ipsilateral projection occupies a crescent, where the central edge of the 5% isodensity is 64.1±1.6 degrees of arc from the optic pole and spans 134.1±1.5˚ of the rim extending from 22.1±1.3˚ above

the temporal pole to 22.0±1.5˚ past the dorsal pole (Figure 3-3F). When a composite plot of the contralateral label was made, this picture is not as clear, but when measuring the peripheral edges of the 5% isodensity contour, and thereby examining the area with the least label in each retina there is a trend towards the ventrotemporal retina having a lower density of contralaterally projecting cells (Figure 3-3G). This less dense area is further from the retinal pole (81.0±2.5˚) and OD (81.5±3.9˚) (Figure 3-3H) and tends to span a larger fraction of the rim of 144.7±9.3˚. As can be seen from the scatter in the measurements in Figure 3-3I, the distribution is not as consistent as the ipsilateral projection and any inferences made from plots such as this are therefore highly speculative. With these considerations in mind, it still appears that the extent of the contralateral crescent extending above the temporal pole, at 18.9±6.6˚, is equivalent to that of the ipsilateral crescent, whereas the extent of the contralateral crescent beyond the ventral pole at 35.8±9.4˚ is larger than that of the ipsilateral crescent (p = 0.0035, unpaired t-test).

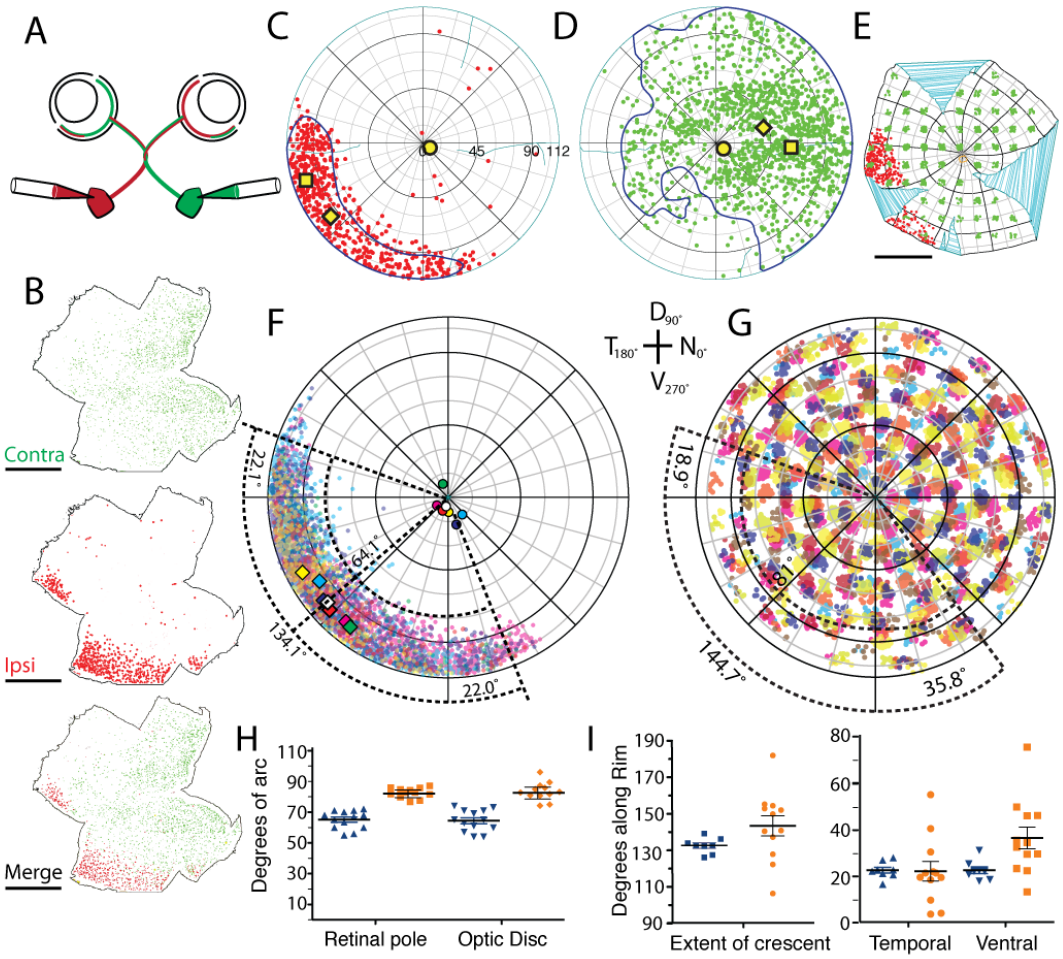

Figure 3-3: Measurements of the ipsilateral and contralateral projections

A, Schematic of the bilateral injections into the dLGN, which label both contralateral and ipsilateral projections in both eyes. **B,** Thresholded images of the ipsi- and contralateral label in one eye resulting from the injections illustrated in A. **C-D,** Azimuthal equidistant plots of the ipsilateral and contralateral label in B. Yellow diamonds represent the Karcher mean of all the label and the yellow squares are the peak density of the Kernel. Isodensity contours were plotted using kernel density estimates (KDE). Yellow circle is the OD. **E,** Flat-mount of left retina with both contralateral (green) and ipsilateral (red) label. The contralateral label was only partially sampled using a one-in-nine sampling strategy in a 150µm grid. The ipsilateral label was sampled fully. Scale bar is 1 mm. **F-G,** Composite of ipsilateral label (F) and contralateral label (G) (*n=12*). The angles plotted (dashed lines) represent the mean extent of the label, defined by the 5% KDE or KRE isodensity contour for fully or partially sampled retinae, respectively. **H,** Distance to the central edge of the ipsilateral crescent to the optic axis and the OD. **I,** Total extent of crescent and amount beyond temporal pole and dorsal pole for ipsilateral label (blue) and contralateral label (orange)

3.2.4 Transformation to visuotopic coordinates

Since the central edge of the region in the retina labelled by the projection to the ipsilateral dLGN is expected to correspond to the vertical meridian in the mouse's visual field (Dräger and Olsen, 1980; Coleman et al., 2009), we have mapped the retina onto visual space to test whether this holds true the observed orientations of the retina. The mapping of visual space onto the retina is determined by the orientation of the optic axis and since light is refracted as it passes through the lens, the optics of the eye are important as well. The shape of the eye and the lens have been described (Remtulla and Hallett, 1985; Schmucker and Schaeffel, 2004). However, since there are considerable complications associated with the calculations of refraction for the full spectrum of wavelengths of light, we have used the approximation that the visual field for each eye is 180˚. Therefore for the projections, we have set the optic axis as 0˚ and then projected the 112˚ of retinal space from there to the 90˚ of visual space in concentric circles (see Methods section 2.2.5 and Figure 2-2 for details).

The optic axis is close to but not coincident with the projection of the optic disc (See Figure 2-2A). Opthalmologically, the location of the optic disc in anaesthetised mice has been estimated to be projected to a point 60° lateral to the vertical and 35° above the horizontal meridian (Dräger, 1978). Alternatively, the optic axis has been reported to be 64˚ lateral to the vertical and 22˚ above the horizontal meridian in awake behaving mice (Oommen and Stahl, 2008). To evaluate these two projections, we have transformed retinal space into visuotopic space (Figure 3-4B; See Methods section 2.2.5 for details). In particular, we focus on how the retinal position of the ipsilateral decussation line (Figure 3-3F) maps onto the vertical meridian of visuotopic space (Bishop et al., 1962). An approximate diagram of this projection through the horizontal plane of the mouse's head is shown in Figure 3-4B. This diagram describes how the rays from the ventrotemporal crescent are refracted through the lens and due to the orientation of the optic axis of the eye (solid grey line), these rays are projected across the visual midline and thereby enable binocular vision. It is worth noting that this diagram is an approximation and varying the eye orientation and the distance of the "visual space"

circle will change the amount of overlap. This is also why the rays in the diagram are not evenly spaced on the "visual space" circle.

When plotting the decussation line to visuotopic space using the optic axis coordinates of 64˚ azimuth and 22˚ elevation (Oommen and Stahl, 2008), the decussation line lines up with the vertical meridian with only limited overlap in upper visual field (Figure 3-4C). If, in contrast, the decussation line is projected using the OD coordinates of 60˚ azimuth and 35˚ elevation (Dräger, 1978), there is a gap in the central visual field (Figure 3-4D). The decussation line can also be seen in the lower visual field if the contralateral label is projected with the optic axis at 64˚ azimuth and 22˚ elevation (Figure 3-4E), although there is a larger overlap of red and green label, as would be expected from the further distance of the contralateral crescent from the optic pole (Figure 3-3G).

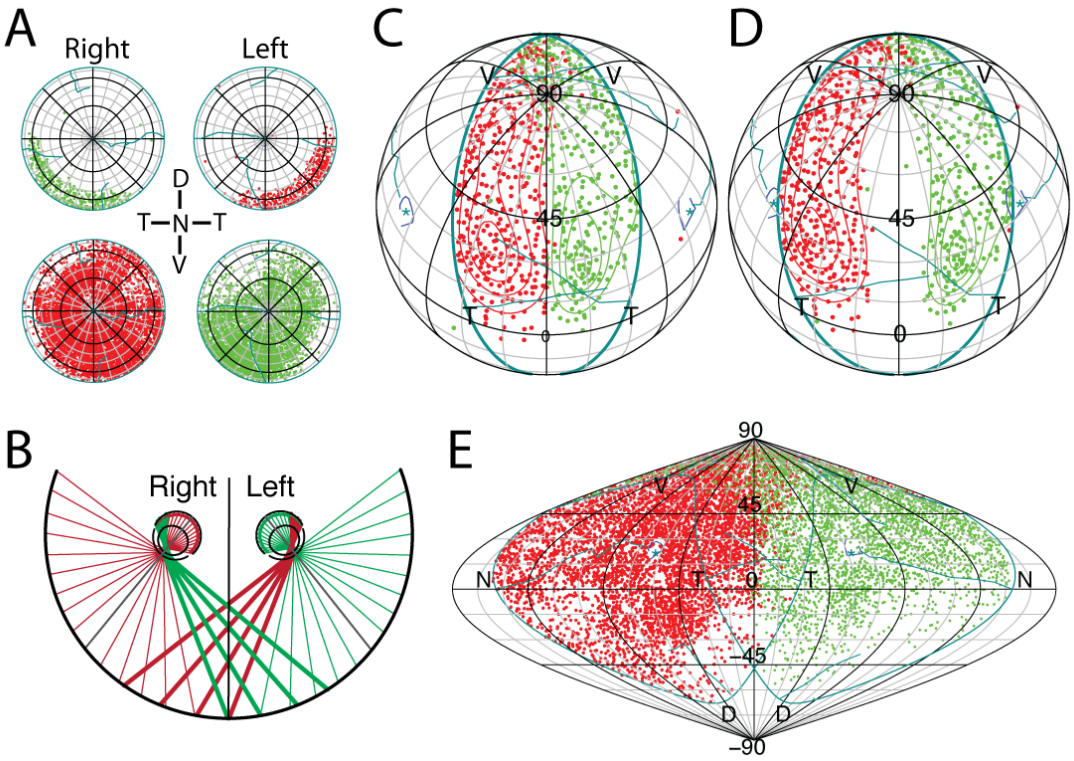

Figure 3-4: Binocularity of ipsi and contralateral label

A, Azimuthal equidistant projection of left and right retinae with ipsilateral (top) and contralateral (bottom) label from injections of red and green dextran into left and right SC respectively. **B,** Schematic illustrating how the label of the retinae in A is projected to visuotopic coordinates using an approximation of the optics of the eye and of the estimated projection of visual space onto the retina (see Figure 2-2E). The thick lines represent rays that are incident with the ventrotemporal crescent. Note that the binocular zone in this diagram is expanded slightly for emphasise and the "visual field" sphere has been shrunk for convenience (in reality the eyes are both closer to the centre of the sphere and smaller. **C-D**, Orthographic projections rotated to 50˚ elevation of the ipsilateral label in A. Projection in C is plotted with the optic axis (*) at 64˚ azimuth and 22˚ elevation, whereas projection in D is plotted with the optic disc at 60˚ azimuth and 35˚ elevation. **E,** Sinusoidal projection of contralateral label in A, with optic axis like that in C. In C-E, N T D V represent where the retinal poles are projected in visual space.

3.2.5 Orienting visuotopic space

Having verified the orientation of the optic axis, we wanted to examine the orientation of the eye in visual space. The mean muscle insertion vectors (Figure 3-1F) were therefore projected to visuotopic coordinates and plotted in an orthographic plot with the optic axis at 64˚ azimuth and 22˚ elevation (Oommen and Stahl, 2008) in Figure 3-5A. In this plot, the lateral rectus vector runs along the horizontal meridian, the superior rectus vector is projected along the vertical meridian in the lower visual field and the inferior rectus in the upper visual field is offset from the vertical meridian by 14˚ of longitude. When plotted as one hemisphere in the sinusoidal plot, it is more apparent where in visual space the muscle insertions are and in turn in which direction they are responsible for rotating the eye (Figure 3-5B).

When projecting the distribution of S-opsin from Figure 3-2 to visual space in a similar manner, we would expect the transition from high to low density to correspond to the horizontal meridian (Szél et al., 1992). Label was projected to visuotopic space and plotted in orthographic plots (Figure 3-5C) to measure the angle of the label relative to the horizontal meridian inferred from the optic axis position at 64˚ azimuth and 22˚ elevation. The transition is on average 6±1.6˚ above the horizontal meridian in central visual field and 7.8±2˚ below the horizontal meridian in peripheral visual field (Figure 3-5F). To establish whether the level of the transition was coincident with the horizontal meridian across the entire visual field, the label from both left and right retinae was also plotted in a sinusoidal projection (Figure 3-5E). In this plot it is clear that there is a symmetry across the two retinae, where the transition from both retinae are at the same level in central visual field and roughly the same level in peripheral visual field as well. The implications of this will be discussed later.

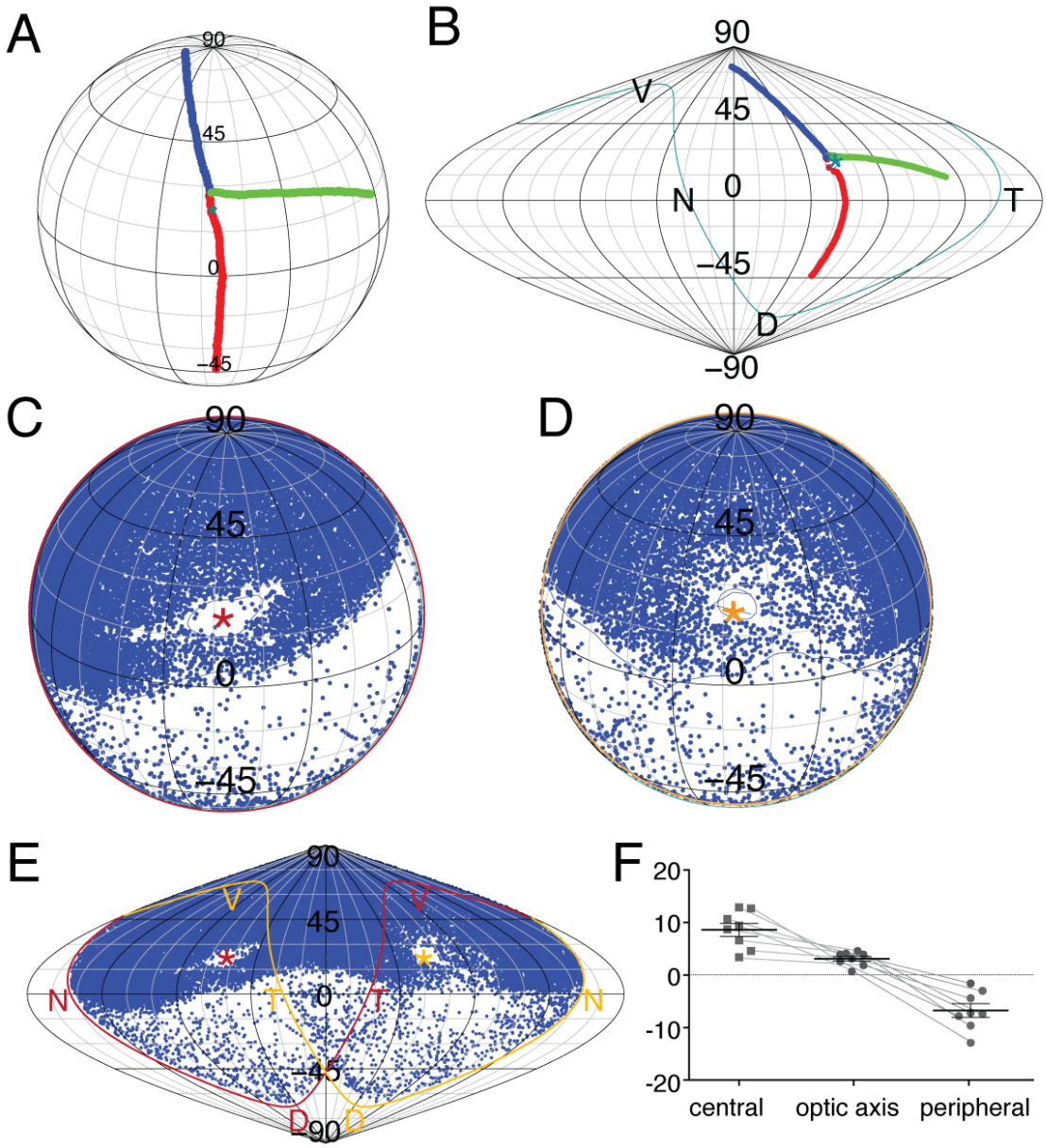

Figure 3-5 Orientation of visuotopic space

A-B, Orthographic plot (A) and sinusoidal plot (B) of the mean muscle insertion vectors from Figure 3-1C projected to visuotopic coordinates. **D-E,** Orthographic plot of S-opsin distribution in left and right retinae from Figure 3-2. Showing that the transition is almost coincident with the horizontal meridian at the level of the optic axis. **E,** Sinusoidal plot of visuotopic S-opsin distribution, showing the symmetry across the entire visual field, with the transition lower in peripheral visual field and higher in central visual field. All plots are centred on optic axis (*) at 64˚ azimuth and 22˚ elevation. **F,** Quantification of observations in C-D (*n*=9). Dashed line at 0˚ represents the horizontal meridian. Line is mean and error bars are SEM.

3.3 Results: Adult Retinocollicular topographic precision

In this section we move from discussing the reconstruction and orientation of the eye to applying these reconstructions of standard retinae to tackling the problem of quantifying the primary projection to the Superior Colliculus (SC). In order to proceed with examining the developmental system, it is necessary to have a handle on the anatomy of the mature system. To this means, we examined the topographic precision of the adult mouse (from 60 days to a year of age) in two different strains, both commonly used in visual research and as a background for many genetic modifications. Firstly we examined the topography in C57BL6/J mice. By using paired small (<10nl) discrete injections of red and green fluorescent latex beads, we could consistently get an almost complete (90%) segregation of label in the retina with injection sites that are separated by 98 μm or more (Figure 3-6E). We, moreover, found that a single injection in most of the SC resulted in a tight focus in the retina of 2.3±0.3% of the retina, as illustrated in Figure 3-6. We then compare these results to the precision in the CD-1 albino strain.

3.3.1 Measurement of precision in the retinocollicular projection

For quantifying the precision in the projection, we have firstly treated the data from each of the paired injections, mentioned above, independently to examine how much of the retina converges on a point in the SC. To do this, it is assumed that the injections can be treated as points on the surface of the SC. This is a reasonable assumption, since the injections span the entire depth of the retinorecipient Stratum Griseum Superficiale (SGS) of the SC (Figure 2-4D, see Figure 3-6B for example); and they are of relatively consistent and small size the mean injection diameter is 57±17μm (Figure 2-4E), which is 2.8% of either axis at the centre of the SC). Once the retinae have been dissected, flat-mounted, analysed and reconstructed, isodensity contours are plotted to exclude 5%, 25%, 50%, 75% & 95% of the least dense cells using a kernel density estimate (KDE; see Methods section 2.3.1 for details). This analysis reveals that for the mature projection, a mean injection covering 2.8% of the axes of the SC results in symmetric focus of label with a diameter of 19˚, which is 8.5% of the retina axes (using a value of $\varphi_0 = 111.6^{\circ}$ (Table 2-3), which means that in terms of diameter, there is a 1:3 ratio from SC to retina. The relative sizes of the other isodensity contours show that the mean

distribution of label is Gaussian in nature (Figure 3-6H), since the means for contours 5-75% form a straight line when plotted on a $\log_{10}$-scale (Figure 3-6I). Moreover, just looking qualitatively at the examples in Figure 3-6C-D, it is clear that the contours are mostly Gaussian and symmetric in all axes, which was confirmed by testing for normality using a Kolmogorov-Smirnoff normality test of the coordinates along the principal NT and DV axis with the result that $p > 0.1$ for all the retinae and the label can therefore be considered as normally distributed.

An example of typical paired injection sites can be seen as a dorsal view (Figure 3-6A) and in a 100µm thick parasagittal section (Figure 3-6B). From the parasagittal section, it is apparent that these injections span the entire depth of the SC SGS and since the average injection site is 291.4±49.5 µm deep (Figure 2-4D), these are typical injections. The diameter of the injection sites also reflects the average size, as the average injection has a diameter of 57.6±17.4 µm (Figure 2-4E). The retinal label resulting from the injections in Figure 3-6 A&B can be seen in Figure 3-6 C&D. Another factor that may influence the measurements is the angle of the injection site, because of this injections were done orthogonally to the surface and the average angle is 87.4µm (Figure 2-4F). It is worth noting that even though the injection sites are non-overlapping, there is still a band of double-labelled cells (yellow cells in Figure 3-6E) where the two foci of label overlap, indicating that there are several RGC axons that branch into both injection sites. Moreover, since the double-labelled cells are only present at the overlap of the red and green label, and as the distance between the edges of the two injection sites at 46µm approximates to the width of the injection sites, this must be the minimum span of the axonal arbour for these axons. Because the majority of axons are either red or green, it indicates that the average axon arbour spans in the order of 100µm, which is also consistent with previous measurements, measuring the average axonal arbour size for several different types of RGCs to 100µm (Hong et al., 2011).

In order to examine the order in the projection, we have used the data from paired injections in the same animal to calculate the probability of any cell having a neighbour of the same colour. If all cells in a retina have a neighbour of the same colour, then this

pair of injections has a nearest neighbour (*N*) value of 1, whereas if the distribution of label is random and the two foci of label are completely coincident, this will give an *N* value of 0.5 (See Methods section 2.5.4 for details). If there is significantly less of one kind of cells, it is possible to get values of less than 0.5 for that colour. However, since the quoted NN value is for a pair of injections the mean of the two colours will reflect the overall order of the projection at least for ratios of less than 1:5. These NN values are then plotted as a function of the separation of the centre of the SC injection sites.

The best-fit curve for this data is a 2-parameter logistic fit (Figure 3-6J), which is defined in the methods (Equation 2-13). Briefly, this function gives two principal measures of a curve, the inflection point (κ) and the slope of the tangent at this point (τ). Further measurements that are of interest is the point where the curve saturates, indicating that the label is completely segregated. Here I have used the value of NN=0.9 as this point. This curve offers an accurate fit for the mature dataset (Figure 3-6J) with an R^2 of 0.89 and the sum of squared errors of the residuals (SSE) of 0.066, which since R^2 is close to 1 and SSE < 0.1 and the residuals are symmetrical around the zero-line, constitutes a reasonable fit. Using this fit, to describe the data, we find that to get two foci that are 90% separate (NN=0.9), we need to separate the SC injection sites by at least 92.3±22µm, whereas any separation of less than 50µm will result in >90% overlap of the resulting label, often with double-labeled cells in the interface between green and red label (Figure 3-6E).

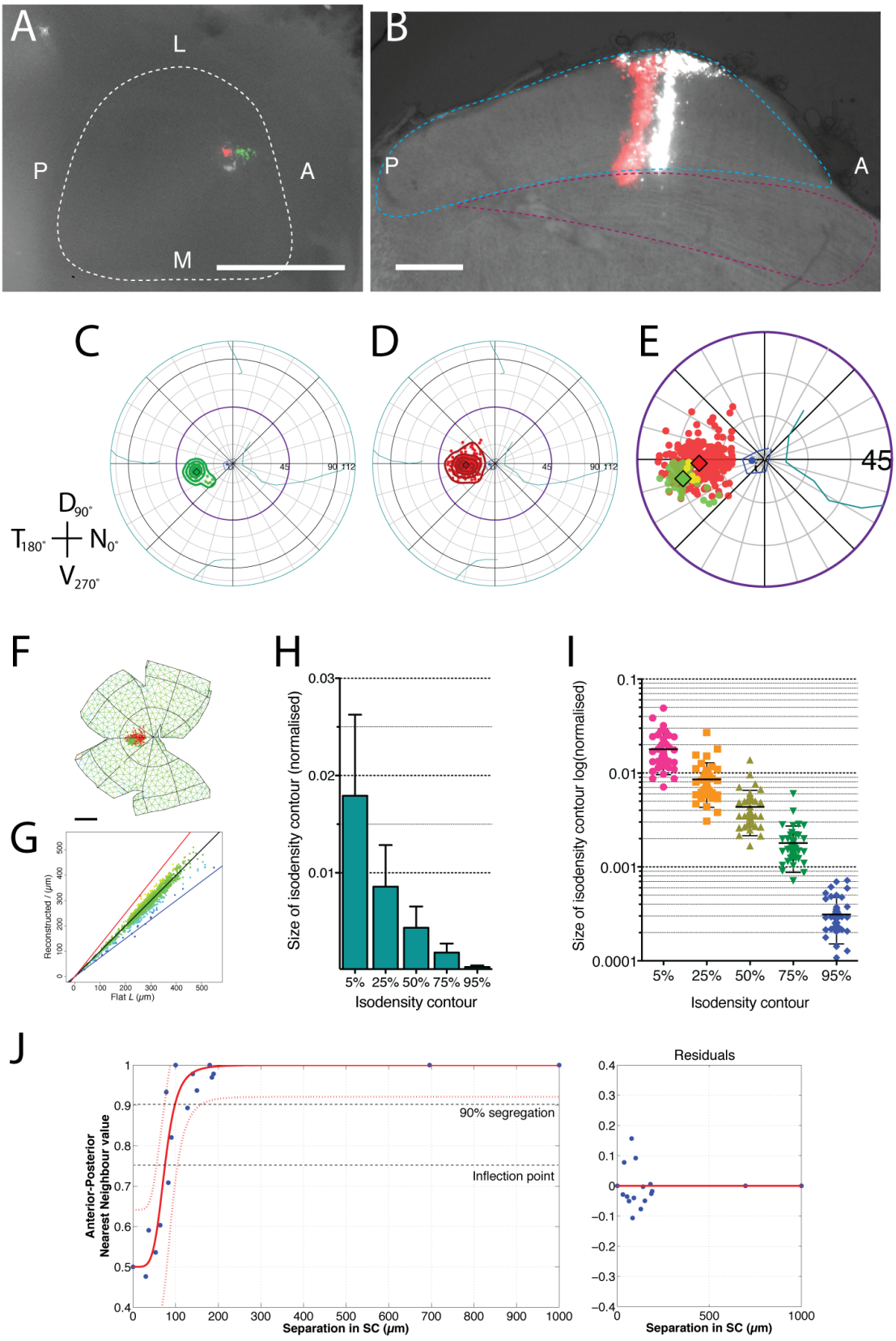

Figure 3-6: Retrograde tracing from SC

Figure 3-6 Legend: Retrograde Tracing from the SC (previous page)

A, Dorsal view of SC showing the paired injection sites of red and green retrobeads. Dashed line is the outline of the SC. Scale bar is 1 mm. **B,** Parasagittal section at the level of the injection sites in A. Injection sites span the entire SGS, the edges of which are shown by blue outline. Magenta outline is the edge of the SO. Scale bar is 200µm. **C,** Azimuthal equal-area projection of reconstructed retina with label resulting from injections in A-B. Top plots represent the entire retina with isodensity contour lines plotted to 5%, 25%, 50%, 75% & 95% of peak density (indicated by diamond). OD displacement in the reconstruction is 4.3˚ and **D,** Enlarged view of the central 45˚ of retina in C. Also note the band of double-labelled (yellow) cells between the red and green foci. **E,** Original flat-mount of retina in C & D. Grid is colour-coded to show compression (blue) and expansion (red). **G,** Plot of expansion/compression. $\sqrt{E_L} = 0.044$ **H,** Histogram of the mean amount of retina covered by each of the isodensity contours in C. Error bars are SD. **I,** Scatterplot of the data in H plotted on a $\log_{10}$ scale to illustrate the scatter of contour sizes for different injections. **J,** Overlap of the label by nearest neighbour segregation measure plotted against separation of injection sites along the AP axis of the SC. Line fits are logistic curves defined by Equation 2-13. The right hand plot represents the residuals associated with the fit, which as can be are symmetrical around the zero-line. Red dashed line indicates the 95% confidence interval for the fitted curves. For this fit the slope is 5.2±2.1; the inflection point is at 74.9±8.6µm and 90% segregation (y=0.9) is at 98±24µm; with R^2=0.89 & SSE=0.066, it is a reasonable fit.

3.3.2 Quantifying topography

One aim of reconstructing the retinae is to create a standard space, which would enable consistent comparison of data between animals, while not crucial for most of the analysis of the projection in Figure 3-6, it is crucial for examining the topography within the projection. Figure 3-7 shows a preliminary examination of topography. In this figure, the coordinates of the Karcher mean of the label (as indicated in Figure 3-6E) for each injection was plotted onto a standard spherical retina and projected in an Azimuthal equidistant plot. These points are then colour-coded according to the location of the injection site in the SC. The anterior-posterior topography is examined in Figure 3-7A, where anterior injection sites are red and posterior injection sites are blue. Likewise, in Figure 3-7B, where medial injection sites are blue and lateral injection sites are red. Figure 3-7A clearly shows a progression from red through green to blue when looking from temporal to nasal, which is consistent with the nasal retina projecting to the posterior SC and the temporal retina projecting to the posterior SC. In Figure 3-7B, the transition is less marked, as most of the medial and posterior SC is under sampled. There is also considerable scatter in the colours in the ventral-temporal retina, while some of this scatter is due to variance in determining the location of the injection site and the distortions associated with dissecting and reconstructing the retina, it could also reflect the compression of the map in the anterior-medial SC, as suggested by Dräger & Hubel (1976). From examining both axes, it is apparent that the map appears to be at a 15-20˚ angle to the axes of the retina, as defined here by the eyelids and the nictitating membrane. Which again is similar to the physiological orientation suggested by Dräger & Hubel (1976).

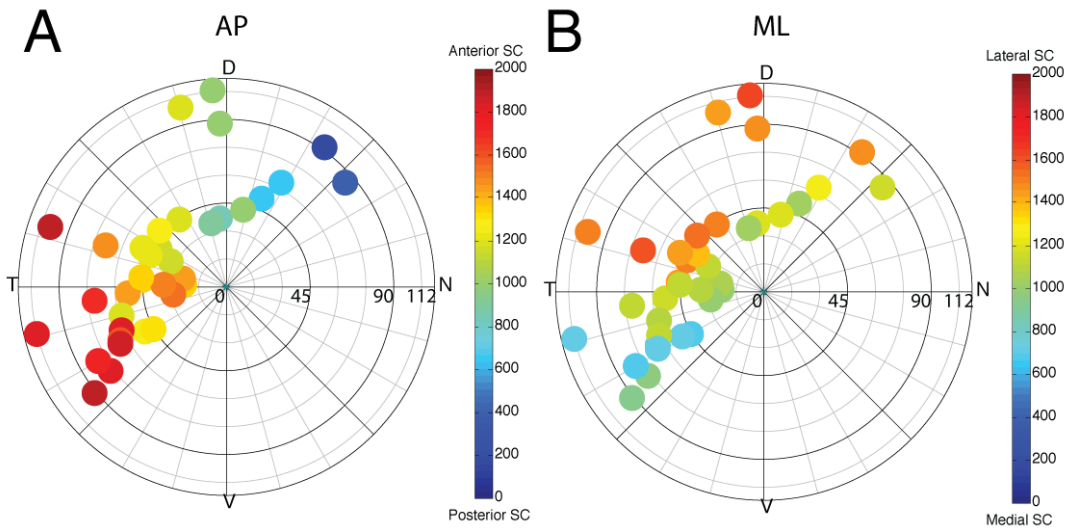

Figure 3-7: Retinocollicular topography

A-B, Composite plots of Karcher mean location of label from retrograde label in adult retinae (*n* = 32 animals). Locations are colour-coded according to the AP (A) or ML (B) position of the corresponding injection site, distances are in µm. Blue represents posterior (A) or medial (B) SC and red represents anterior (A) or lateral (B) SC. Under sampling in ventral-nasal retina is due to sinuses over medial and posterior SC making injections in this area difficult.

3.3.3 Precision in the Albino Mouse

Having a description of the wild-type, the next step was then to verify this technique in a different strain, so we decided to examine the commonly used outbred albino CD-1 strain, since some topographic defects have been reported in this strain (Dräger & Olsen, 1980). Repeating the same experiments as for the C57BL6/J (Figure 3-6) in this strain provided fairly similar results with the main difference being that there is a trend towards the projection being less precise.

For the contour analysis, we have quantified the area enclosed by the 5%, 25%, 50%, 75% and 95% kernel density isodensity contours, and there are no significant differences between the two strains (Figure 3-8C). A discrete injection of <10nl Retrobeads in an adult CD-1 mouse will result in 2.4±0.4% of the retina containing labelled cells (as defined by the 5% isodensity contour), against 2.3±0.2% in an adult C57BL6/J mouse. It is a similar story for the other contour levels, and no significant differences are found for any contours (see Table 3-1 for values).

Although similarly sized injections label approximately the same area of the retina, when measuring the order in the projection using the nearest neighbour measure, there appears to be a trend towards the projection in the CD-1 strain being less ordered. When plotting the nearest neighbour probability against separation of the collicular injection sites and fitting them with a logistic curve (Equation 2-13). It is apparent that although there is overlap of label, the differences in the optimal curve fits to the two populations indicate that they are subtly different. As can be seen in Figure 3-8F, the curve for the CD-1 data is not as steep as the curve for the C57BL6/J data. With slopes of 2.1±1.0 for CD-1 and 5.2±1.9 for C57BL6/J, according to the 95% confidence interval of the fits the slopes are different. However, due to the overlap of the label distributions, there is considerable overlap of the 95% confidence intervals at the inflection points of the curve, it being at 92.3±22 μm for CD-1 and at 74.9±8.6 μm for C57BL6/J mice. Although the inflection points are comparable, due to the differences in the slope, the distance at which we get 90% segregated label, and thus can say that the foci are

separate, is amplified to be at 178.5±63 μm for CD-1 and at 98±22 μm for C57BL6/J mice. Although the 95% CIs still overlap, largely due to the increased scatter in the CD-1 data, there is a trend towards the CD-1 strain having a less precise projection.

Strain	*n*	Contour	Mean size (%)	SEM	SD	Median size (%)
C57Bl6/J	61	5%	2.3	0.2	1.4	1.9
		25%	1.1	0.09	0.7	0.87
		50%	0.56	0.04	0.3	0.48
		75%	0.23	0.02	0.1	0.18
		95%	0.039	0.004	0.02	0.032
CD-1	36	5%	2.4	0.4	2.3	1.8
		25%	1.1	0.2	1.1	0.79
		50%	0.55	0.09	0.5	0.37
		75%	0.23	0.04	0.2	0.17
		95%	0.044	0.008	0.05	0.033

Table 3-1 Isodensity contour analysis of the mature projection

Data of the sizes of the isodensity contours of label in Figure 3-8 from individual injections in adult (P60+) C57BL6/J and CD-1 mice.

		Logistic fit (eqn. 2-13)				
Strain	***n***	**slope (κ)**	**inflection (τ)**	**$x_{(y=0.9)}$**	**SSE**	**R^2**
C57Bl6/J	16	5.17	74.9	98.0	0.066	0.89
CD-1	14	2.13	92.4	178.5	0.047	0.89

Table 3-2 Nearest neighbour analysis of the mature projection

Data regarding the fitting of the 2-parameter logistic function to nearest neighbour data from paired injections in adult C57BL6/J and CD-1 mice. SSE is the Sum of Squared Error, which reflects the mean distance of the residuals from the zero line. R^2 is the coefficient of determination and reflects the variability of the data that can be accounted for by the model (1 represents a perfect fit). Taken together, these two measures gives a good indication of the goodness of fit of the function.

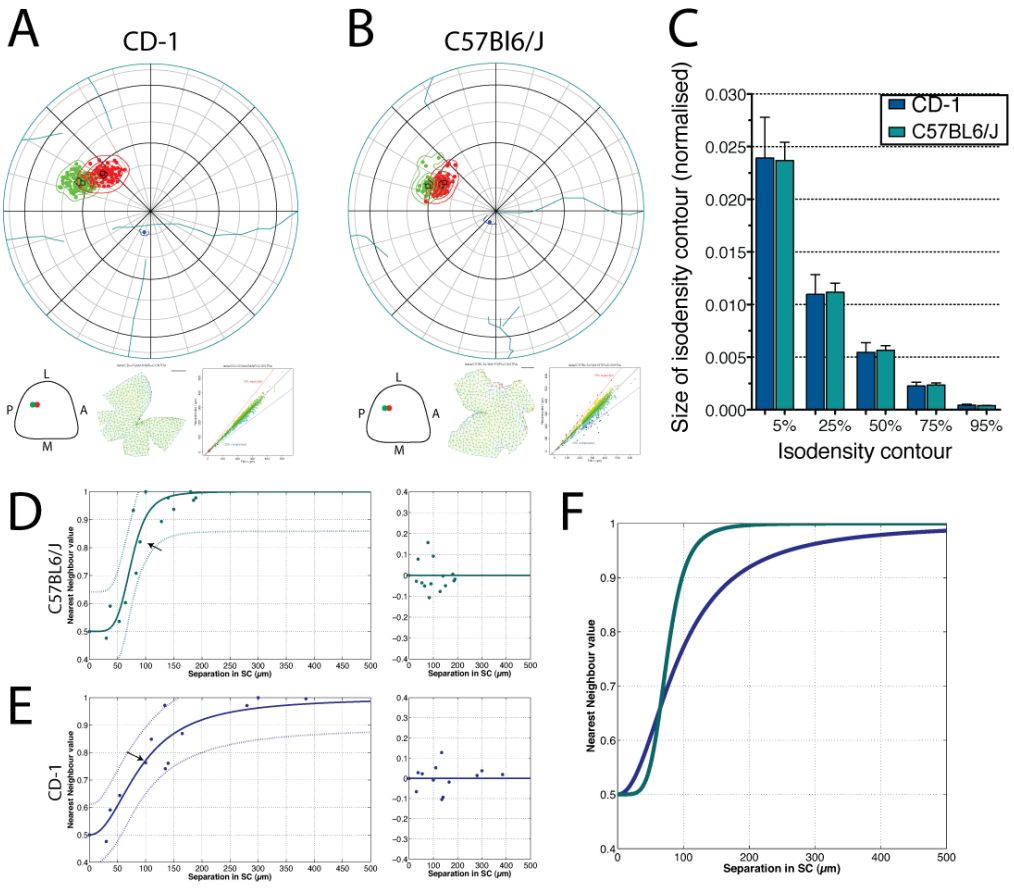

Figure 3-8: Comparing C57BL6/J and CD-1 mouse strains

A-B, Examples of label from paired injections in adult CD-1 (A) and C57Bl6/J (B) mice plotted in an equidistant azimuthal projection. Injections are of similar size and location in both examples. Isodensity contours a plotted to 5%, 25%, 50%, 75% & 95% of the KDE. Bottom plots from left to right show the location of the injections in the SC; the original flat-mount colour-coded for expansion (red) and compression (blue); and scatterplot of this expansion/compression. **C,** Histogram of the mean size of isodensity contours for C57BL6/J (green) (*n*=56 injections) and CD-1 (blue) (*n*=35 injections), showing no significant difference between the two strains in the size of the labelled projection. Error bars are SEM. **D-E,** Overlap of the label by nearest neighbour segregation measure plotted against separation of injection sites in SC with C57BL6/J in green (D) and CD-1 in blue (E). Line fits are logistic curves defined by Equation 2-13. The right hand plot represents the residuals associated with each fit, which as can be are symmetrical around the zero-line. Dashed line indicates the 95% confidence interval for the fitted curves. Arrow indicates the NN value of the examples shown in A & B. For the fit to C57BL/6J (D), the slope is 5.2±2.1; the inflection point is at 74.9±8.6 µm and 90% segregation (y=0.9) is at 98±22µm; with R^2=0.89 & SSE=0.066, it is a reasonable fit. For the fit to CD-1 (E), the slope is 2.1±1.0; the inflection point is at 92.3±22 µm and 90% segregation (y=0.9) is at 178.5±63µm; with R^2=0.89 & SSE=0.046, it is also a reasonable fit. **F,** Plot of both C57BL6/J (green) and CD-1 (blue) fits from D&E.

3.4 Discussion

3.4.1 Reconstructing and Orienting the Retina

The techniques for flat-mounting retinae are well established (Stone, 1981; Hess, 1987) and have been used extensively. Since the mouse retina is devoid of any obvious landmarks. This is unlike the avian retina, which has a ventral streak, the rabbit retina with the horizontal streak and the carnivore & primate retinae, which have either an area centralis or a fovea. The cut through the nictitating membrane, which has been used for this study, is an alternative way of orienting the retina.

Importantly, reconstructing retinae provides a standardised coordinate system, which enables the comparison of retinal features between multiple animals of different ages. Plotting features such as muscle-insertions, photoreceptor density and distribution of retinal ganglion cell subtypes in a standard framework means that more rigorous analyses of the variance between samples and across groups can be performed. Here we have provided several new insights that have been gained from the application of this method to the problems of understanding the orientation of the eye in relation to central connections and external visual space.

The plotting of the ipsilateral projections in standard retinal and visuotopic coordinates has enabled us to validate the position of the visual axes and by extension, the location of the optic nerve head. By plotting the crescent in visuotopic coordinates using the optic disc locations inferred from physiological recordings by Dräger & Hubel (1978), we found that the binocular zone from each retina does not line up along the vertical meridian, as would be expected (Figure 6D). However, when using the coordinates for the optic axis calculated by Oommen and Stahl (2008), we find that the binocular zone lines up perfectly with the vertical meridian (Figure 6C). Using these coordinates, the binocular zone in central visual field is 52˚ (Figure 3-4C-D), which is larger than the 30-40˚ estimated by Dräger & Hubel (1978), but comparable to the 50-60˚ estimated by Rice & Goldowitz (1995) and Coleman & Bear (2009) and significantly larger than that in many other lateral-eyed animals, e.g. 30˚ in rabbit (Hughes, 1971). This probably

reflects the very protruding eyes in the mouse and the relatively large field of view of each eye

Moreover, by comparing the “horizon” labelled by the staining of s-opsin (Figure 8) to the horizontal meridian in previous studies (Dräger and Olsen, 1980; Coleman et al., 2009), we see that our results suggest that the s-opsin “horizon” is lower in the visual field than the horizontal meridian suggested previously. Moreover, our data from antibody staining for s-opsin shows that the s-opsin “horizon” relative to the nictitating membrane is lower in peripheral visual field than in central visual field (Figure 8 D-E), which when taken together with the insertion of the lateral rectus muscle making a parallel vector with the horizontal meridian (Figure 3-5A) could indicate that if the s-opsin “horizon” is indeed parallel to the horizontal meridian (Szél et al., 1992), then the rotation of the eye must be at an angle of 13.8±3.6˚ relative to the horizon. If this is the case, then it could explain why the observations from plotting the retinocollicular topography based on the injection site locations (Figure3-7) give a similar value. This is also partly supported by data from physiological experiments, which show that in the superior colliculus, the input axes are indeed offset from the cardinal axes by 15˚ as well (Dräger and Hubel, 1976).

The transition of the S-opsin cones from high density to low density has been reported mostly as a gradient (Applebury et al., 2000; Haverkamp et al., 2005). In my hands, however, it not so much a gradient as a very sudden transition. Haverkamp et al. (2005) also report that while there is a high incidence of co-localisation of long wavelength opsin and S-opsin in ventral retina, "blue" bipolar cells contacted only cones with only S-opsin. Therefore, when just considering these cones, the difference between ventral-dorsal is less marked, but still represents a 3-fold increase in density. The S-cone pathway is traditionally ON (Haverkamp et al., 2005), but two recent papers (Chen and Li, 2012; Sher and DeVries, 2012) suggest that S-cones affect the OFF-pathway as well. This mechanism is mediated by specialised inhibitory amacrine cells, which means that although cones that express exclusively S-Opsin are contacted by ON-bipolar cells that synapse in the ON-lamina of the IPL (Haverkamp et al., 2005), these inhibitory

amacrine cells may facilitate an OFF pathway for short wavelength (blue) cones (Chen and Li, 2012; Sher and DeVries, 2012). As for the biological significance of this distribution, Haverkamp et al. (2005) suggested that the distribution of S-Opsin may reflect the fact that S-Opsin is more prone to light-damage, and a higher proportion is therefore needed in ventral retina. This taken together with the co-expression of long wavelength opsin and S-opsin could suggest a role for these wide field cones in predator detection (detecting dark objects against a light background), which since these are connected to W3 cells responsible for detecting features in ventral retina (Zhang et al., 2012), is probably the case. It also originally suggested that S-Opsin (or OS-2 positive) cone transition is coincident with the horizontal meridian or an (oblique) meridian (Szél et al., 1992). When the figures from that paper are reconstructed and plotted in visuotopic coordinates using Retistruct (Figure 3-9), the angle of incidence with the horizontal meridian is comparable with that seen with the S-Opsin staining in Figure 3-2. They also see that M-Opsin (COS-1 positive) is expressed exclusively in the dorsal retina. On an interesting sidenote, Szél et al. (1994) also looked at different mouse-like species (*Apodemus Sylvaticus*) and here they didn't see this distribution in S-opsin expression, so it may be specific to certain mouse-breeds.

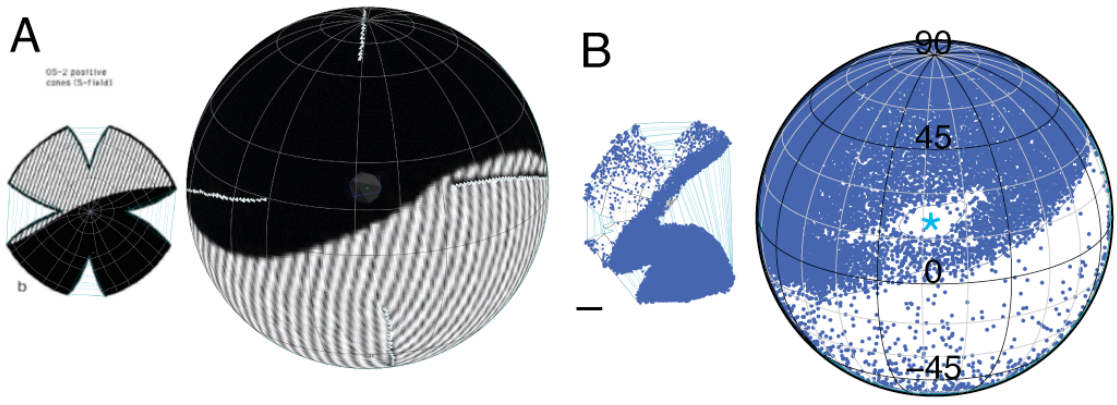

Figure 3-9 Comparison of S-opsin distribution with Literature

A-B, Comparison of S-opsin distributions from a previous paper (Szél et al., 1992) (A) and the staining from an S-opsin antibody (B) both shown as flat-mounts and projected to visual space and represented by an orthographic projection centred on the optic axis (*) at 64˚ azimuth and 22˚ elevation.

3.4.2 Precision in the Retinocollicular Projection

The precision of 98±22µm found when analysing the data from the paired injections closely resembles the physiological precision from observations that it is possible to resolve single receptive fields when doing recordings using a multi-electrode with electrode-spacings of 120µm (Andrew Lowe, unpublished observations). Such coherence between physiology and anatomy could suggest that the size of functional units of collicular neurons approximately resembles the size of the input from the retina

It is, furthermore, interesting to note that according to the isodensity contour analysis of individual injections in the central SC, there is a 1:3 ratio between the relative spread of the injections and the relative spread of the label. If we project the retinal label to visuotopic space, we find that the 25% isodensity contour (assuming that the least dense RGCs don't contribute significantly to the receptive field) occupies 15˚ of visual space, which means that 2.8% of the AP collicular axis will receive input from 15˚ of visual space. Doing a calculation based on the results from Dräger and Hubel (1976), where they estimate that 15˚ of central visual space is represented by 2.5% of the AP collicular axis. The results are therefore relatively consistent since the mean injection site diameter covers 2.8% of the retina. Another complication to this kind of analysis is that the physiological mapping of the SC from electrical recordings indicates that the receptive fields in the superior colliculus are not uniform across the entire structure, but are compressed in the anterior-medial SC and expanded in the posterior-lateral SC (Dräger and Hubel, 1976). However, in analysing the data, I have not observed any consistent changes in size of the label with the location of the injection sites, although due to the relatively few injections in the posterior SC, it is not possible to say anything conclusive on this point.

Chapter 4 Development of Collicular Retinotopic Precision

4.1 Introduction

Topographically precise neural maps are a universal and essential feature of the nervous system that enables the neural networks to convey positional information across different neural systems for parallel processing. Such topographical organisation is found throughout the visual system, where retinal neighbour relationships are preserved in primary and secondary visual structures.

The relative contribution of molecular cues and instructive spontaneous activity during development and whether they are mutually exclusive events or somehow interact is largely unknown. Further, it is not clear that our current understanding of actual molecular components and spontaneous or sensory modulated activity represents the full complement of mechanisms involved at all scales of the constructed circuit (Mrsic-Flogel et al., 2005; Rashid et al., 2005; Cang et al., 2008b).

Although numerous studies have provided an insight into the development of topography in the retinocollicular projection (Hindges et al., 2002; McLaughlin et al., 2003b; Xu et al., 2011) these studies are largely qualitative and as a result there is a lack of quantitative data on the spatiotemporal sequence of development, which is needed for making predictions about which patterns of guidance cues and activity patterns are needed for the general development of spatially precise topographic projections.

In this chapter I provide an in-depth quantitative spatiotemporal description of the post-natal development of topographical organisation in the mouse retino-collicular projection by comparing point-to-point connectivity between the SC and retina. I show that only limited topographical precision is present at P0 and that precise topography only starts to appear between P6-P8 and reaches adult levels by around P16. In the characterisation of the wild-type development of precision along the AP axis (figure 2), the observations from anterograde studies are confirmed (Hindges et al., 2002;

McLaughlin et al., 2003b). The data in this chapter, moreover, provide a quantitative tool for assessing the level of precision in the retinocollicular projection.

4.2 Development of Precision

To investigate the development of topography, paired discrete injections of Retrobeads were made into the SGS of the SC. Typically injections were 5-10nl, as estimated by measuring the level of tracer in the pipette, and thus small enough to label a discrete column in the SGS, while limiting diffusion. Diffusion, continuous uptake by cells and passing axon fibres can be a big problem when using other tracers, e.g. DiI or Dextran-conjugates, especially in neonatal tissue. The Retrobeads overcome this problem as the size of the beads limits diffusion and since the beads coagulate quickly, there is a limited timeframe for uptake (Katz et al., 1984). For example of injections, see Figure 2-4 & 3-6. Injections are of similar sizes to those in the adult, and close injections in young animals also give an area with double-labelled cells on the overlap of the two foci (cf. Figure 3.6E and Figure 4-4, P6). Following a period of 18 hours or more (depending on age), when the Retrobeads have been transported to the RGC soma, the label in the retina can be quantified as described in methods, the retina reconstructed and the locations of labelled RGCs plotted in standard polar coordinates. Since these are all in standard coordinates, it is possible to compare the shape, density, spread and location of the label across multiple animals within an age-group, and after normalising for the changing shape and size of the retina, across ages.

Plotting the data for individual animals for multiple ages gives a good overview of the qualitative sequence of development. It is equivalent to the data from anterograde tracing performed extensively previously (Hindges et al., 2002; McLaughlin et al., 2003b), with the addition that it reveals projection patterns from across the whole retina. In Figure 4-1, are examples of label from injections into the anterior-medial quadrant of the SC. The examples were picked to represent injection sites that are approximately in the same area of the SC in all ages. Examining the P0 retina, we see that at a single discrete injection of Retrobeads done at P0 results in almost the entire retina containing labelled cells. Although the density of labelled cells is not constant. In the example

shown, the 5% isodensity contour encloses the whole ventral hemi-retina (the injection was in medial SC, but the region of highest density, as defined by the 25% KRE isodensity contour is more localised. However, although the label is clearly hemispherical along the DV axis, it is not confined to either nasal or temporal retina, even though it is an anterior injection and might be expected to be in the temporal retina. Another aspect worth noting is that the Karcher mean location of the labelled cells (the yellow diamond) is different from the location of the peak KRE density (yellow square).

For an injection done at P2 it is a very similar picture, and almost the same amount of the retina contains labelled RGCs. If anything, in the example shown the label is more diffuse. By P4, however, although most of the retina still contains labelled cells and the 5% isodensity contour is still hemi-retinal, the focus of labelled ganglion cells is more clearly defined. In the example shown in Figure 4-1, the 25% isodensity contour now no longer spans the entire length of the NT axis, but instead it covers a third of the retina. At this age, the Karcher mean location of the labelled cells and the KRE peak density also converges so that the Karcher mean now is within the 75% isodensity contour.

For injections at P6 there is a clearly defined focus and although the cells outside the focus (50% contour) are still spread out, only a confined part of the retina contains labelled cells. The main difference between P6 and P8 is the removal of most of these "ectopic" projecting cells, which causes the difference between the 5% and 50% isodensity contours to be reduced and leads to a more clearly defined focus. By P12 the continued removal of ectopic cells causes the difference between the 5% and 50% contour to be further reduced, although the 5% contour is still noticeably larger than the 50% contour. For injections done at P16, this difference in area of the 5% contour is reduced to the point that there is little difference between the contours and all of them have the same shape. Consequently, at this age the label looks qualitatively mature.

An interesting observation from this period is that there appears to be three different stages of the refinement, with an initial refinement from P0 to P4 primarily of label

along AP collicular axis, represented by the decrease in the extent of the 5% isodensity contour along the NT retinal axis in Figure 4-1. This is then followed by removal of "ectopic" cells and a resulting reduction in the size of the 5% contour from P4-P8. Finally, there is a noticeable period of fine refinement, seen as a decrease in the size of the focus represented by the 25% isodensity contour from P6 to P12.

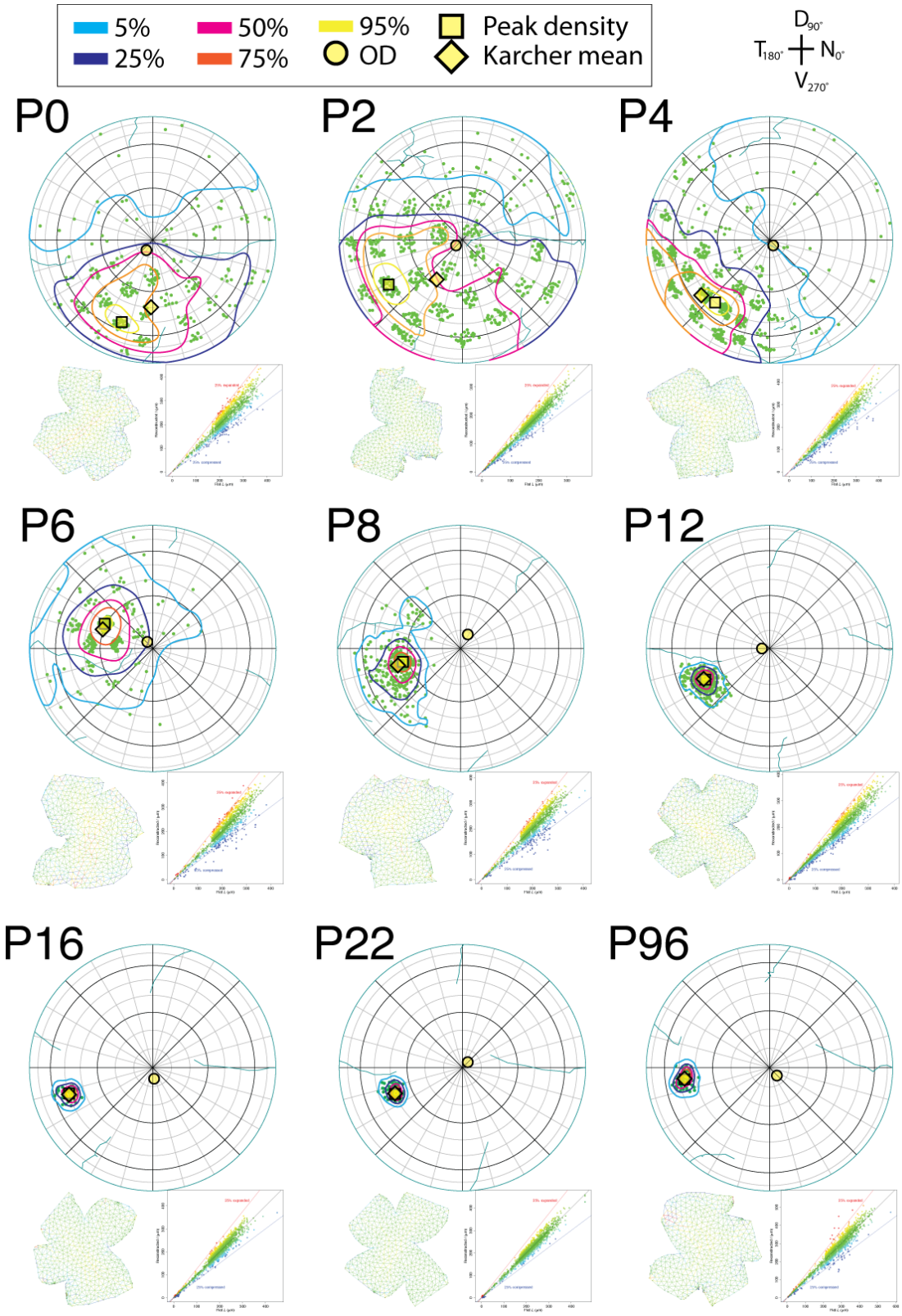

Figure 4-1 Examples of label through development

Figure 4-1 Legend – Examples of label through development (previous page)
Label resulting from single discrete injections of a comparable size into the anterior superior colliculus at different stages of postnatal development. Isodensity contours are plotted by excluding 5% (light blue), 25% (dark blue), 50% (pink), 75% (orange) & 95% (yellow) of the cells with the lowest density using either KR estimates where partial sampling is used or KD estimates where retina is fully sampled (See Section 2.3.1 for details). All plots are Azimuthal equal-area plots using the rim-angle for the respective age (values for φ_0 are given in Table 2-3). Yellow circle is OD, square is the peak density and diamond is the Karcher mean of the label. Small plots for each retina represents the distortions involved in reconstructing the retina. These are the original flat-mounts (left) and scatterplot of reconstructed vs. original segment length (right) colour-coded for expansion (red) and compression (blue)

The representative examples in Figure 4-1 give a good overview of the development, but to really understand the dynamics of the refinement of the projection, it is necessary to thoroughly quantify the distribution of label within an age group to be able to compare the sizes and shapes of the label distribution across ages. Although the examples in Figure 4-1 are picked to be representative there is variability in the label, which reflects both experimental and real biological variation between animals. For this reason, the projections have been characterised by plotting isodensity contours by excluding 5%, 25%, 50%, 75% and 95% of the densest label, as found by kernel density (KD) or kernel regression (KR) estimates (See Methods for details). To enable comparison across ages, the sizes of the contours have been normalised to the size of the retina in degrees squared at the respective age. The data is shown in Table 4-1 and represented in Figure 4-2 (P0 to P8) and Figure 4-3 (P8 to adult). These two figures show the proportion of the retina containing labelled cells (Figure 4-2A) and the sizes of the isodensity contour levels for all injections of all the ages sampled to give an impression of the scatter in the data (Figure 4-2B-F) and also give the mean and standard deviation for each age and contour level. Note that to better represent the scatter in the sizes of the contour-levels, the scales are vastly different for each contour-level. The differences between ages for a given contour level were established by using a two-tailed one-way ANOVA with a Bonferroni post-hoc test. To illustrate the relative changes in the sizes of the isodensity contour levels across all ages, the mean sizes are summarised in Figure 4-3. Also reflecting the vast differences in sizes of the contours, this plot is on a log-scale.

At P0 the entire retina (96.4±2.9%) contains labelled cells (Figure 4-2A). However, since the 5% Isodensity contour covers 45.1±9.8% of the retina (Figure 4-2B), it indicates that the 5% of cells with the lowest density (the difference between the two measures above) are spread out over a large area, covering half the retina, and can therefore be considered as ectopic cells. The 50% isodensity contour covers 10% of the retina, and as can be seen from the P0 example in Figure 4-1, it is mostly possible to identify an area of higher density in the correct half of the retina.

At P2, the ectopic cells are still spread out and occupy 90.3±9.3% of the retina and the size of the 5% isodensity contour also remains constant at P2 (42.7±12.5%). The higher contour-levels similarly remain constant from P0 to P2, reflecting that little changes in the precision of the projection immediately after birth.

By P4, although some animals still have labelled cells throughout the retina, there are also several cases where this is significantly reduced with the result that the average proportion of the retina containing labelled cells is reduced to 76.6±12.4%. Also reflecting the removal of many ectopically projecting cells, is the reduction in the 5% isodensity contour to 35.4±2.5% of the retina. The sizes of the higher contour-levels are also reduced significantly. After P4, there is a further significant decrease ($p<0.0001$) to P6 when 42.8±9.2% of the retina contains labelled cells. This refinement of ectopic cells is also reflected in the reduction from 35.4±2.5% at P5 to 11.1±9.6% of the retina covered by the 5% isodensity contour at P6. These significant differences are seen across all the contours and could therefore also reflect the removal of a significant number of cells across the entire projection. Interestingly, although there is a reduction in the proportion of the retina containing labelled cells from P6 to P8 (from 42.8±9.2% to 25.6±9.4%), the sizes of all the isodensity contours remain constant, indicating that although the shape of the distribution of label is the same, vastly ectopically projecting cells appear to be removed preferentially at this stage.

From P8 to P12 (Figure 4-3), there is a further significant reduction ($p<0.001$) in the amount of retina containing labelled cells to 3.1±1.2%. This is accompanied by a significant decrease in the size of the 5% isodensity contour ($p<0.001$) to 3.2±2.1% of the retina, showing that since these two measures are the same, there are effectively no more ectopic cells from this stage onwards. Also reflecting the mature nature of the precision at P12 is the fact that from this stage there are no more significant refinements across any of the contour-levels to adulthood. There is, however, still a gradual decrease in the size of the 5% contour-level to 1.8±0.92% at P16 and 2.5±1.1% at P22 to the final mature level at 2.2±1.1% of the total retinal area.

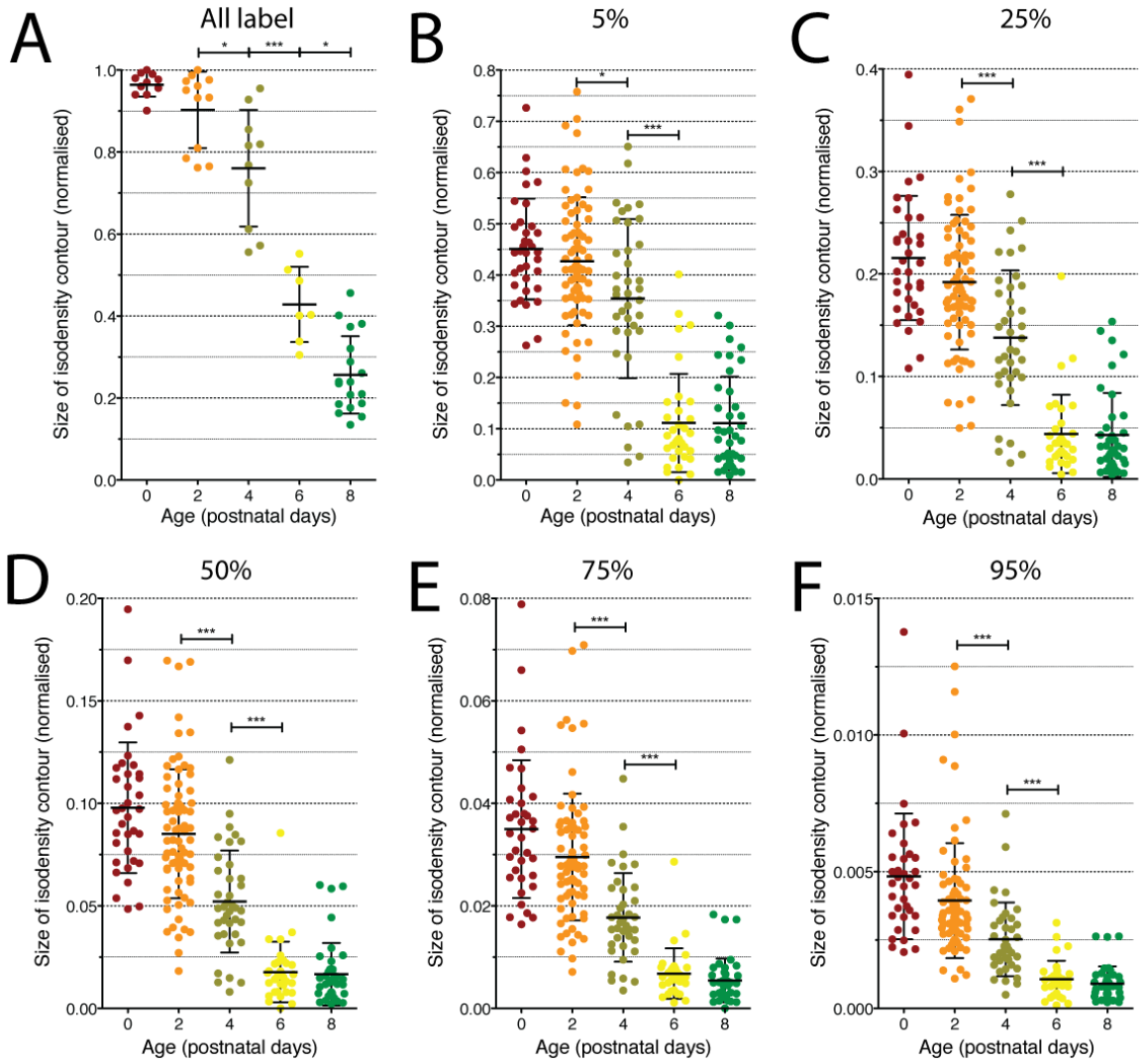

Figure 4-2 Isodensity contour analysis of early (P0-8) development

A, Proportion of retina containing any labelled cells from Systat analysis (see methods), hence why the *n* is lower. **B-F,** Scatterplots with the sizes of the isodensity contours for 5% (A), 25% (B), 50% (C), 75% (D) & 95% (E). Areas have been normalised to the size of the retina in deg^2 (Equation 2-10). Line is the mean and error bars are standard deviation. Significance determined using a one-way ANOVA with a Bonferroni post-hoc test.

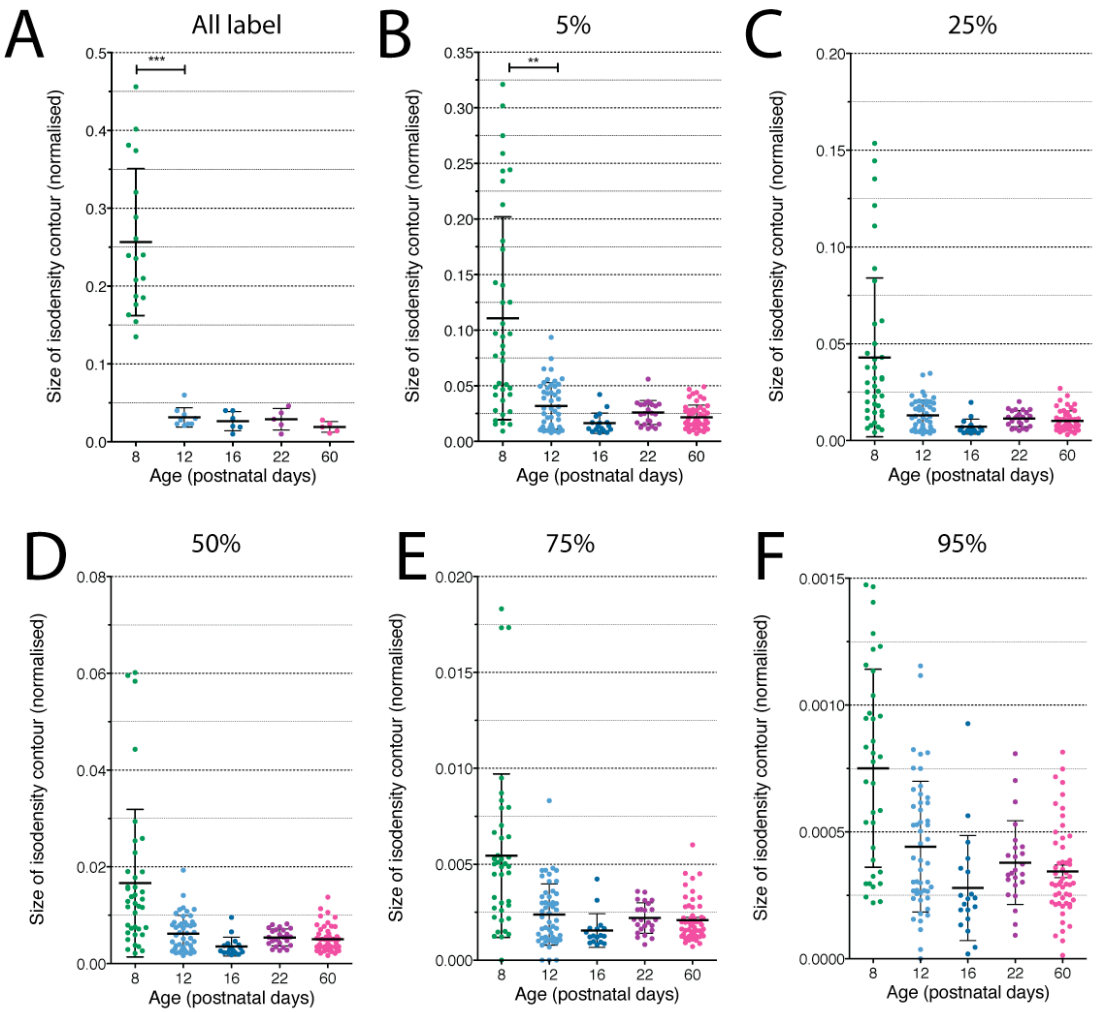

Figure 4-3 Isodensity contour analysis of late (P8-60+) development

A, Proportion of retina containing any labelled cells from Systat analysis (see methods), hence why the *n* is lower. **B -F,** Scatterplots with the sizes of the isodensity contours for 5% (A), 25% (B), 50% (C), 75% (D) & 95% (E). Areas have been normalised to the size of the retina in deg^2 (Equation 2-10). Line is the mean and error bars are SD. Significance determined using a one-way ANOVA with a Bonferroni post-test.

To summarise the isodensity contour analysis, the mean sizes of all the isodensity contours are plotted for all ages in Figure 4-4. This plot shows that the relative changes of any given contour-level with age is similar for all the contour-levels. The only difference is in the amount of retina containing any label, as this measure does not show as large a reduction in size from P4 to P6 as the isodensity contours. This measure instead shows a reduction in size from P4 to P8. The amount of retina containing any labelled cells, moreover, also show a larger decrease in size from P8 to P12 than the isodensity contours. As a result of that difference, this measure is the same as the 5% isodensity contour from P12. The reason why all the label appears to occupy a smaller area than the 5% contour-level in adult animals is that the data are from different datasets. Another aspect of the development that is apparent when plotting the isodensity contours for all ages together is that there are two main periods of refinement of the "broad" projection (5% - 50% contour levels) from P4 to P6 and from P8 to P12 that are not as apparent in the contour-levels describing the focus of label (75% & 95%).

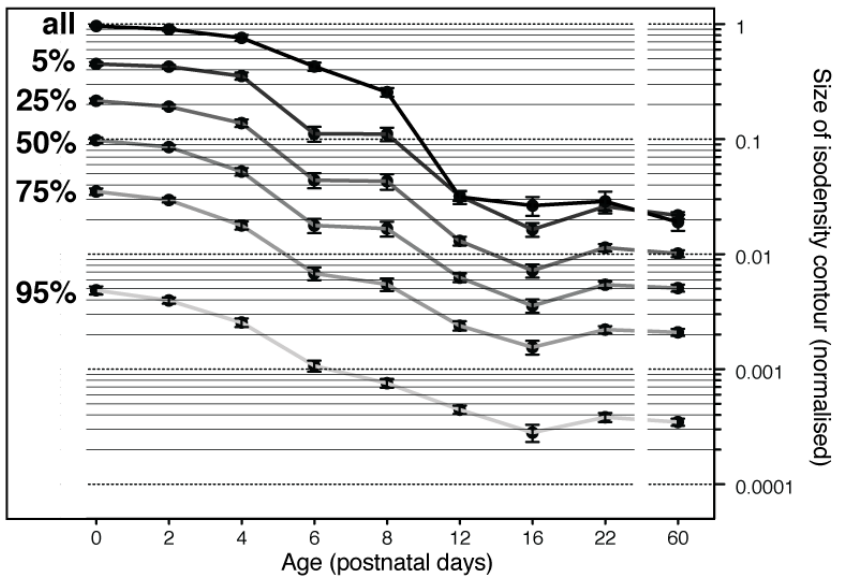

Figure 4-4 Summary of developmental isodensity contour analysis

Mean data from Figures 4-2 and 4-3 plotted on a log scale to illustrate the relative sizes and changes of all the different contours across all ages. Error bars are standard error of the mean.

Age	*n (KRE/KDE)*	Contour	Median size	Mean size	SEM	SD
P0	35 (30/5)	5%	0.445	0.451	0.0166	0.0982
		25%	0.211	0.216	0.0103	0.0607
		50%	0.0966	0.0979	0.00539	0.0319
		75%	0.0341	0.0350	0.00228	0.0135
		95%	0.00458	0.00483	0.000389	0.00230
P2	76 (66/10)	5%	0.413	0.427	0.0143	0.125
		25%	0.185	0.192	0.00753	0.0657
		50%	0.0821	0.0851	0.00361	0.0315
		75%	0.0278	0.0295	0.00142	0.0124
		95%	0.00340	0.00394	0.000241	0.00210
P4	38 (30/8)	5%	0.363	0.354	0.0252	0.155
		25%	0.132	0.138	0.0107	0.0657
		50%	0.0489	0.0521	0.00404	0.0249
		75%	0.0165	0.0177	0.00140	0.00863
		95%	0.00221	0.00253	0.000219	0.00135
P6	33 (10/23)	5%	0.0792	0.111	0.0165	0.0959
		25%	0.0350	0.0439	0.00666	0.0382
		50%	0.0160	0.0177	0.00254	0.0148
		75%	0.00582	0.00678	0.000857	0.00493
		95%	0.00102	0.00106	0.000117	0.000673
P8	35 (6/29)	5%	0.0825	0.111	0.0148	0.0912
		25%	0.0290	0.0430	0.00666	0.0410
		50%	0.0127	0.0166	0.00248	0.0153
		75%	0.00489	0.00545	0.000683	0.00426
		95%	0.000777	0.000751	0.000065	0.000390
P12	49 (4/45)	5%	0.0285	0.0320	0.00301	0.0209
		25%	0.0120	0.0130	0.00114	0.00791
		50%	0.00557	0.00623	0.000539	0.00373
		75%	0.00207	0.00238	0.000223	0.00159
		95%	0.000388	0.000442	0.000036	0.000258
P16	19 (0/19)	5%	0.0136	0.0164	0.00224	0.00923
		25%	0.00580	0.00717	0.000952	0.00392
		50%	0.00292	0.00355	0.000473	0.00195
		75%	0.00127	0.00155	0.000214	0.000880
		95%	0.000237	0.000279	0.000047	0.000207
P22	24 (0/24)	5%	0.0253	0.0260	0.00220	0.0108
		25%	0.0120	0.0114	0.000845	0.00414
		50%	0.00546	0.00541	0.000356	0.00175
		75%	0.00211	0.00220	0.000162	0.000795
		95%	0.000344	0.000379	0.000033	0.000165

Table 4-1 Isodensity contour analysis of the developing projection

Data of the sizes of the isodensity contours in Figure 4-4 from individual injections at various ages from P0 to P22. *n* reflects the number of injections, not the number of animals. Numbers in bracket represent the ratio of KRE vs. KDE contouring used.

4.3 Development of Order

To look at the development of order in the projection, we performed paired injections into the superior colliculus and with varying separations along either the AP or ML axes. Using this data, we then computed the average probability that any cell within the two populations of labelled RGCs had a nearest neighbour of the same colour. (See methods section 2.5.4 for details). As shown for the adult (Figure 3-6J), plotting this nearest neighbour data as a function of the injection site separation for different ages gives the separation needed to obtain separated foci of label in the retina, which has been used here as a measure for the order of the projection. Thinking about this in visuotopic terms, it corresponds to the collicular separation required to obtain non-overlapping receptive fields, although of course at many of the ages investigated, the retina is not visually responsive and the eyelids are still closed.

4.3.1 Development of anterior-posterior order

The preferred fits were found by using a sum of squares F-test with the null-hypothesis being a straight line with $y_{(x=0)} = 0.5$. Having evaluated several naturally-inspired sigmoid, exponential and logistic functions, the result was that the logistic fit used for the adult and described in the Methods is the better fit (P0: p=0.05; P2: p=0.07; P4: p=0.09; P6: p=0.08; P8: p=0.08; P12: p=0.5; P16: p=0.4; P22: p=0.7). These fits can be seen in Figure 4-5 (P0-6) and Figure 4-6 (P8-22). Although the fits for P6 & P8 are not optimal, since R^2=0.655 and R^2=0.552, respectively, because there is such a big scatter inherent in the data, no better fit could be found. However, since the residuals are symmetric around the fitted line and the sum of squared errors is small ($SSE_{(P6)}$=0.110 & $SSE_{(P8)}$=0.177) , the fits still offer reasonable descriptions of the data. The values for these fits are summarised in Table 4-2.

Using this logistic function to describe the nearest neighbor data, we find that in P0 mouse pups, the projection along the AP axis is still very scattered, probably reflecting that the axons have grown along this axis to the posterior edge of the SC and therefore span the entire AP axis (Hindges et al., 2002; McLaughlin et al., 2003b). This means that injections can be separated by the full length of the SC and still have complete

overlap of label. E.g. one pair of injections in a P0 animal were separated by 1720µm and still resulted in an NN value of 0.52 (Figure 4-5). As a result of this, it is not possible to achieve 90% segregation of label at this age, even if injections are at the very anterior and posterior edges of the SC. The SC is approximately at its mature size at birth (AP: 1910±104 µm; ML: 1800±204 µm; See Table 2-4).

As can be seen in Figure 4-5 (P2), the projection is slightly more ordered at P2. At this age the logistic function takes on its characteristic shape with an initially constant section before starting to increase exponentially (here this point is at 700 µm) until the inflection point (which in this case is at 1438µm; Table 4-1) from which point it starts to saturate and finally reaches saturation (y=0.9) at 1831µm. With the result that at separations above 1831 µm, in contrast to injections done in P0 animals, injections at P2 that are at the very anterior and posterior edges of the SC should give completely segregated label in the retina. However, since there is a lot of scatter at this age this is not certain and more injections with separations above 1500 µm would be needed to be confident about this. To exemplify this scatter, we see that a pair of injections separated by 1300µm resulted in an NN value of 0.5, whereas another animal with injections separated by 1384µm resulted in an NN value of 0.72 (arrow). The label from the latter pair of injections is shown in Figure 4-5(P2).

By P4, this scatter is reduced and injections separated by more than 1688 µm can now confidently be predicted to result in completely segregated label. However, considering the 95% confidence intervals, this could be as little as 900 µm. For example, an animal with injections separated by 1572µm resulted in an NN value of 0.91, whereas the example shown had injections separated by 1212 µm and resulted in an NN value of 0.84 (arrow). However, looking at this example, it is clear that the label is segregated, but the NN value is decreased due to the large number of ectopically projecting RGCs at this age (see also the P4 example in Figure 4-1). This function, moreover, can be distinguished from the P2 function, as it starts rising at 100 µm. The reason for the high value of the saturation point is that the slope of the function is less than that of the P2.

For injections done at P6, some real order is present and now injections separated by 850μm result in 90% segregation of label. This is also reflected in the limited size of the label e.g. the 5% isodensity contour for individual injections at P6 covers 11% of the retina, versus 35% at P4 (See Figure 4-2). The example shown in Figure 4-5(P6) illustrates that some order is present even in relatively closely separated injections with low NN values. Although the example retina had injections separated by 105 μm and a resulting NN value of 0.72, the pattern of red-yellow-green (yellow representing double-labeled RGCs) suggests some sub-order is present at P6 already and this age in that respect is already similar to the adult represented in Figure 3-6E. This sub-order is also the reason why the function rises immediately, indicating that even closely spaced injections reveal some order.

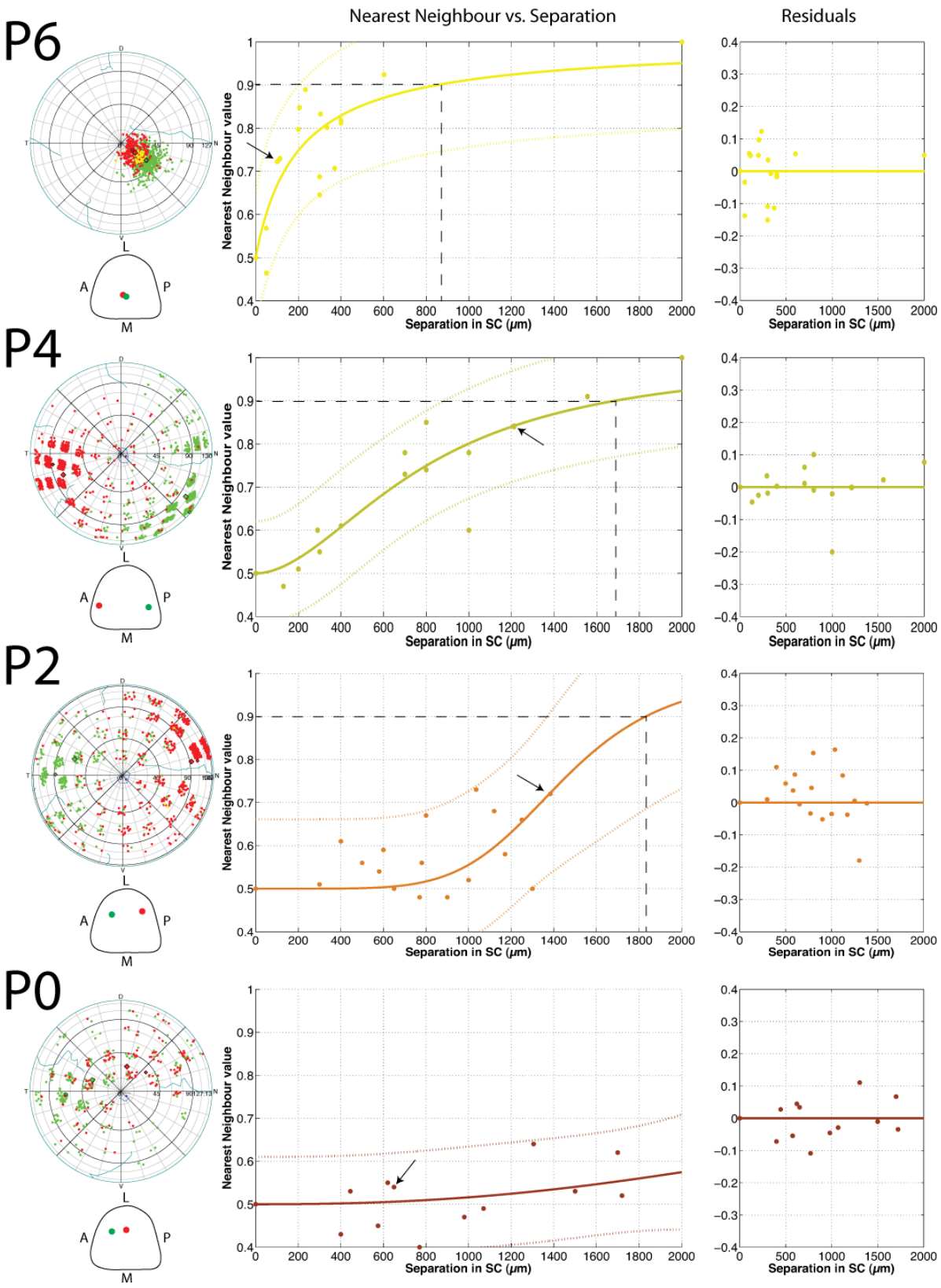

Figure 4-5 Early development of AP order in the projection

Figure 4-5 Legend: Early development of AP order in the projection (previous page)
Overlap of the label measured by nearest neighbour analysis for P0-P6 plotted against separation of injection sites along the AP axis of the SC. The fits are logistic curves defined by Equation 2-13. The black dashed line shows the separation at which label is 90% separate. The right hand plot represents the residuals associated with the fit, which as can be are symmetrical around the zero-line. Dashed line indicates the 95% confidence interval for the fitted curves. The arrow indicates the nearest neighbour value of the associated example retina. Values for the slope, inflection, $x_{(y=0.9)}$ and goodness of fits are in Table 4-2

The order at P8 is very similar to that of P6, as at P8, injections need to be separated by more than 730 µm to get separated foci (Figure 4-6). Although this is slightly lower than the figure for P6, due to the nature of the fits for both) P6 & P8, these curves are almost identical. This is moreover, supported by the slopes being almost the same ($\kappa_{(P6)} = 0.99$ & $\kappa_{(P8)} = 1.11$) and the inflection points being even more similar $x_{(y=0.9)}$ ($\tau_{(P6)} = 203\ \mu m$ & $\tau_{(P8)} = 211\ \mu m$)(Figure 4-7B). The similarity of the curves is also apparent in Figure 4-7A. Although curves are very similar, since there are a couple of examples of injections in P8 animals with separations in the order of 500-550µm resulting in nearest neighbor values >0.9, the actual separation needed for segregated label at P8 may be smaller than the value from the fits.

From P8, there is a significant increase to P12 in the slope of the fitted function (two-tailed F-test; $p<0.05$) from 1.11 at P8 to 2.88 at P12. As a result of this increase in slope and a decrease in the inflection point to 136 µm, the injection separation needed to achieve 90% segregated label is now 222 µm, which is significantly less than at P8. It is, moreover, now possible to achieve a 100% segregation of label at just 280 µm (see P12 example in Figure 4-6). There is little difference in the order of the projection between P12 and P16. The slopes vary only minimally from P12 to P16 at 2.88 and 2.79, respectively. As a result, the inflection points are very similar with 136 at P12 and 128 at P16. The separations needed for 90% segregation are also similar with 222 µm at P12 and 212 µm at P16. The function fitted at P22 is subtly different. It has a shallower slope at 2.19, but since the curve rises earlier, the inflection point is smaller at only 112 µm. However, because of the shallower slope, the threshold for obtaining segregated label at 212 µm is the same as at P16.

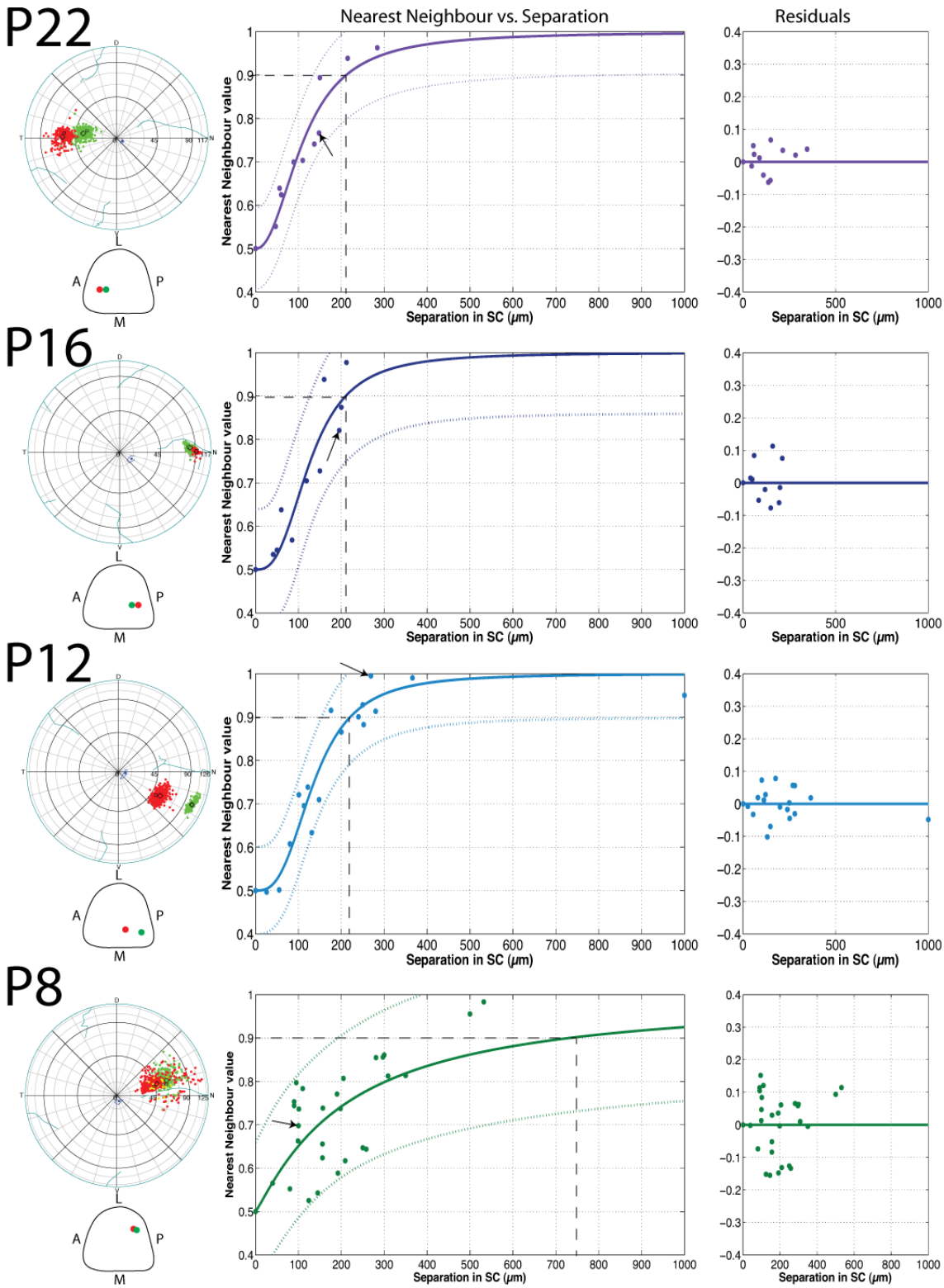

Figure 4-6 late development of AP order in the projection

Figure 4-6 Legend: Late development of AP order in the projection (previous page)
Overlap of the label measured by nearest neighbour analysis for P8-P22 plotted against separation of injection sites along the AP axis of the SC. Line fits are logistic curves defined by Equation 2-13. The black dashed line shows the separation at which label is 90% separate. The right hand plot represents the residuals associated with the fit, which as can be are symmetrical around the zero-line. Dashed line indicates the 95% confidence interval for the fitted curves. The arrow indicates the nearest neighbour value of the associated example retina. Values for the slope, inflection, $x_{(y=0.9)}$ and goodness of fits are in Table 4-1.

		Logistic fit (eqn. 2-13)				
Age	***n***	**slope (κ)**	**inflection (τ)**	**$x_{(y=0.9)}$**	**SSE**	**R^2**
0	12	1.04	4129	*	0.0458	0.141
2	16	1.10	1438	1831	0.146	0.590
4	14	0.87	727	1688	0.0210	0.942
6	16	0.97	203	850	0.110	0.655
8	28	1.12	211	730	0.148	0.552
12	17	2.88	136	222	0.0414	0.928
16	12	2.79	128	210	0.0390	0.883
22	11	2.19	112	212	0.0199	0.940

Table 4-2 Fitting curves to AP nearest neighbour data

Values for fitting of Logistic curve (Equation 2-14) to nearest neighbour data for injections separated along the anterior-posterior axis of the SC. (*) No value is given as it is far beyond the length of the SC, and any value would therefore be meaningless.

Figure 4-7A summarizes the functions fitted to all the different ages in Figure 4-5 and Figure 4-6. Figure 4-7B shows the changes in the inflection point with age. From this plot, it is apparent that there is an initial rapid decrease between P0 to P6 (the inflection point for P0 is not plotted as it is at 4129 μm and thus way beyond the SC) followed by a small decrease from P12 to P16. Notice that there is also a significant decrease P22 to P60+. The plot of the threshold for achieving segregated label (Figure 4-7C) has a similar trend as the inflection point, here there is also no data for P0. Again there are two significant changes in separation between P4 to P6 and P8 to P12. It is also worth noting that although the value for segregation threshold are similar for P2 and P4, these curves are very different as the P2 curve is flat until >700 μm and then rises sharply, whereas the P4 curve rises gradually from >100μm. Again for this measure there is a significant difference between P22 to P60+. Although not significant, there is also a big change from P4 to P6.

An interesting observation from this dataset is that there still appears to be a significant difference between the fits of the P22 and adult (P60+) datasets. For both the inflection point, which is 74.9±8.6 μm for the adult and 112±18 μm for P22 (Figure 4-7B). This difference also reaches significance at y=0.9, where the 95% confidence intervals are non-overlapping (Figure 4-7D, arrow)., which indicates that the separations needed to get 90% segregated label, at 212 μm for P22 mice and 98 μm for adult mice, are also significantly different. (Figure 4-7C; p=0.04; two-tailed test).

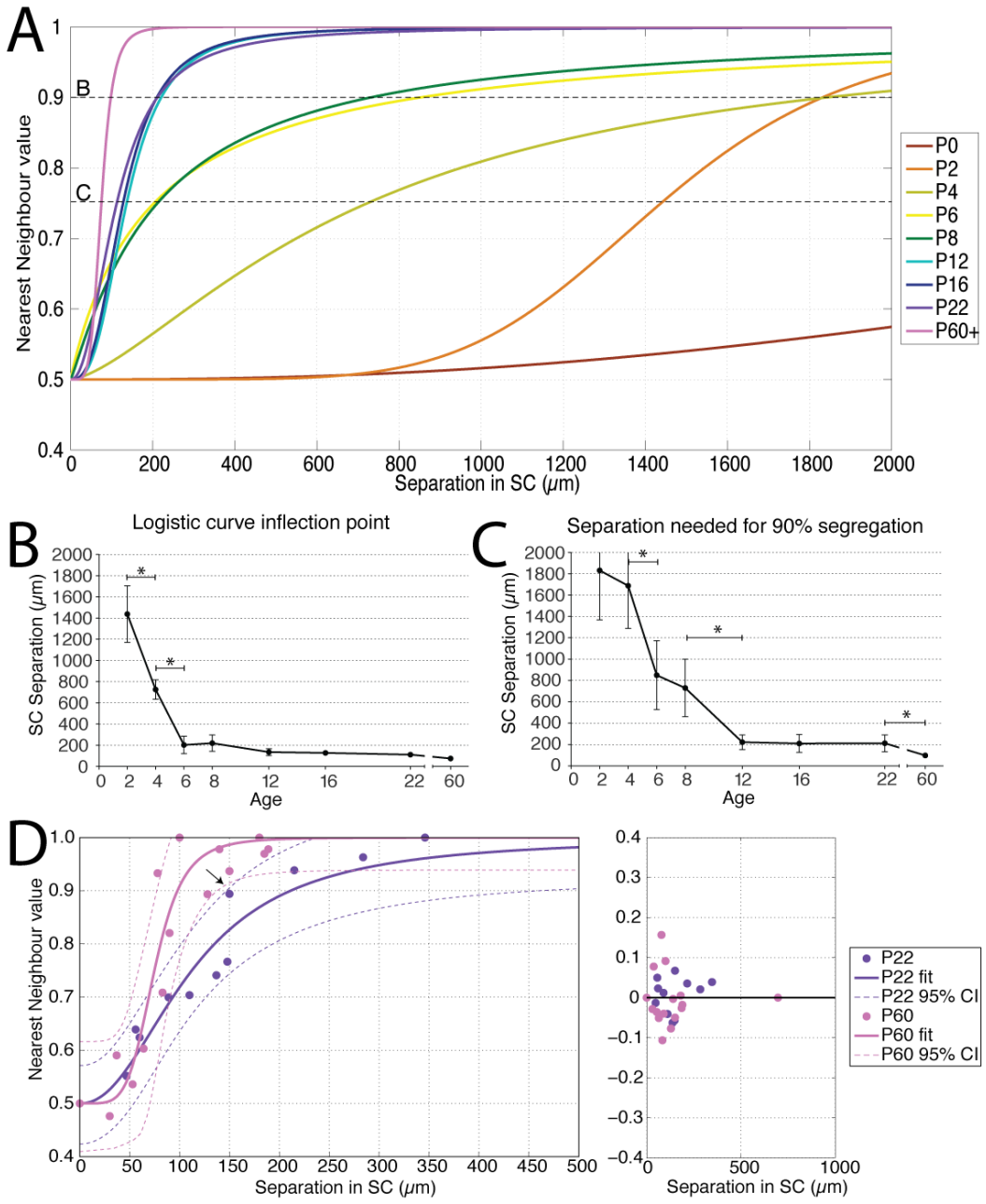

Figure 4-7 Development of AP order in the projection

A, Plot of NN value of retinal label as a function of the SC injection separation along the medial-lateral axis for injections separated along this axis. Curves are from the fits detailed in Figures 4-7 and 4-8. The horizontal dashed lines represent aspects of the curve measured in B & C. **B,** Slope of straight part of logistic curve fit (κ in Equation 2-13) for ages P4-22 plotted as a function of age. **C,** The SC injection separation needed to get 90% segregated foci in the retina according to the fits in A. Error-bars in B-C are represent the 95% CI for the fitted function. **D,** Comparison of fits for P22 and adult (P60). Dashed lines are the 95% confidence intervals for the fits. Arrow indicates the non-overlapping confidence intervals at y=0.9.

4.3.2 Development of medial-lateral order

The development of order along the medial-lateral (ML) is initially quite different from the AP axis described above. The main difference, as can be seen in Figure 4-10 is in the early postnatal projection. In contrast to the AP axis, at P0, there is already a level of order comparable to the P6 AP axis, since injections in a P0 mouse pup separated along the ML axis only need to be separated by 922 μm to result in segregated label. As can also be seen from the P0 example retina in Figure 4-8, a pair of SC injections at P0 separated by 782 μm result in a nearest neighbour value of 0.82. These observations also support previous evidence that axons in the optic tract are bundled according to their approximate DV position in the retina (Chan and Guillery, 1994; Plas et al., 2005). As a result of already being ordered at birth, the ML axis of the projection does not undergo as drastic a development as is the case for the AP axis. In fact, the datasets for P0 and P2 are largely overlapping and consequently, the function describing the P2 data is very similar to the P0 function. The slope for the function fitted to the P2 dataset, at 2.7, is higher than the slope of 1.7 at P0 and the inflection points are also slightly different (P0: 550 μm & P2: 662 μm). However, since the P0 function rises earlier, the threshold for getting segregated retinal label at 922 μm for P0 and 888 μm at P2 are not significantly different.

Paired injections done at P4, need injections to be separated by 615 μm to get segregated label, which although less than that for P0 & P2, due to the spread of the 95% confidence intervals still is not significant. Because of the lower scatter of the residuals in the P4 data, there is, however, still a trend towards it being more refined. In addition, the fitted function at P4 describes the data better than for P0 & P2 (see values for goodness of fit in Table 4-2), which indicates a smaller variability of the data, and could indicate a more ordered projection, or at least a more consistent developmental stage across animals.

At P8, although the slope at 1.4 is similar to P0, since the slope of the function increases from 50 μm, the inflection point is decreased to 229 μm, and the threshold for getting segregated label is similarly decreased to 603 μm. From P8 to P22, the fitted curves all

start rising at the same point, as can be seen in Figure 4-9A, which is also reflected in the slopes gradually increasing from this point (Figure 4-9B), while the inflection point and the threshold for segregated label decreases steadily (Figure 4-9C). At P12, the slope is 1.7, the inflection is at 166 μm and the segregation threshold is at 372 μm. At P22, the slope is 2.0, the inflection point is at 120 μm and the threshold for segregation of label is at 239 μm, which is also illustrated in the example for P22 shown in Figure 4-8, where injections separated by 215 μm results in a nearest neighbour value of 0.92.

Figure 4-10 summarises the development of order along the ML axis. Comparing the fitted curves in Figure 4-10A to the curves fitted to the AP data in Figure 4-7A, it is clear that the ML axis differs significantly from the AP axis, in that the projection along the ML axis starts out more ordered and therefore less refinement is needed to achieve mature precision, as is also seen in anterograde tracing experiments (Hindges et al., 2002; McLaughlin et al., 2003a; Plas et al., 2005). For this reason, the only significant difference seen is in the inflection point for the functions fitted to P4 and P8 data (Figure 4-10B). As a consequence of the slopes being different, however, there are no significant differences for the threshold for achieving segregated label (Figure 4-10C).

Figure 4-10D and 4-10E compare the order in the AP (green) and ML (blue) axes. In these plots it is clear that at birth the ML axis is more refined in both measures and as consequently, we can say that the projection starts out by being asymmetrical. By P6-8, however, both these measures are similar, reflecting that at this age, the projection is symmetrical and the orientation of the paired injections is not as important for determining the order of the projection. From P6 onwards, both the measures remain the same, thus showing that the mature projection is symmetrical.

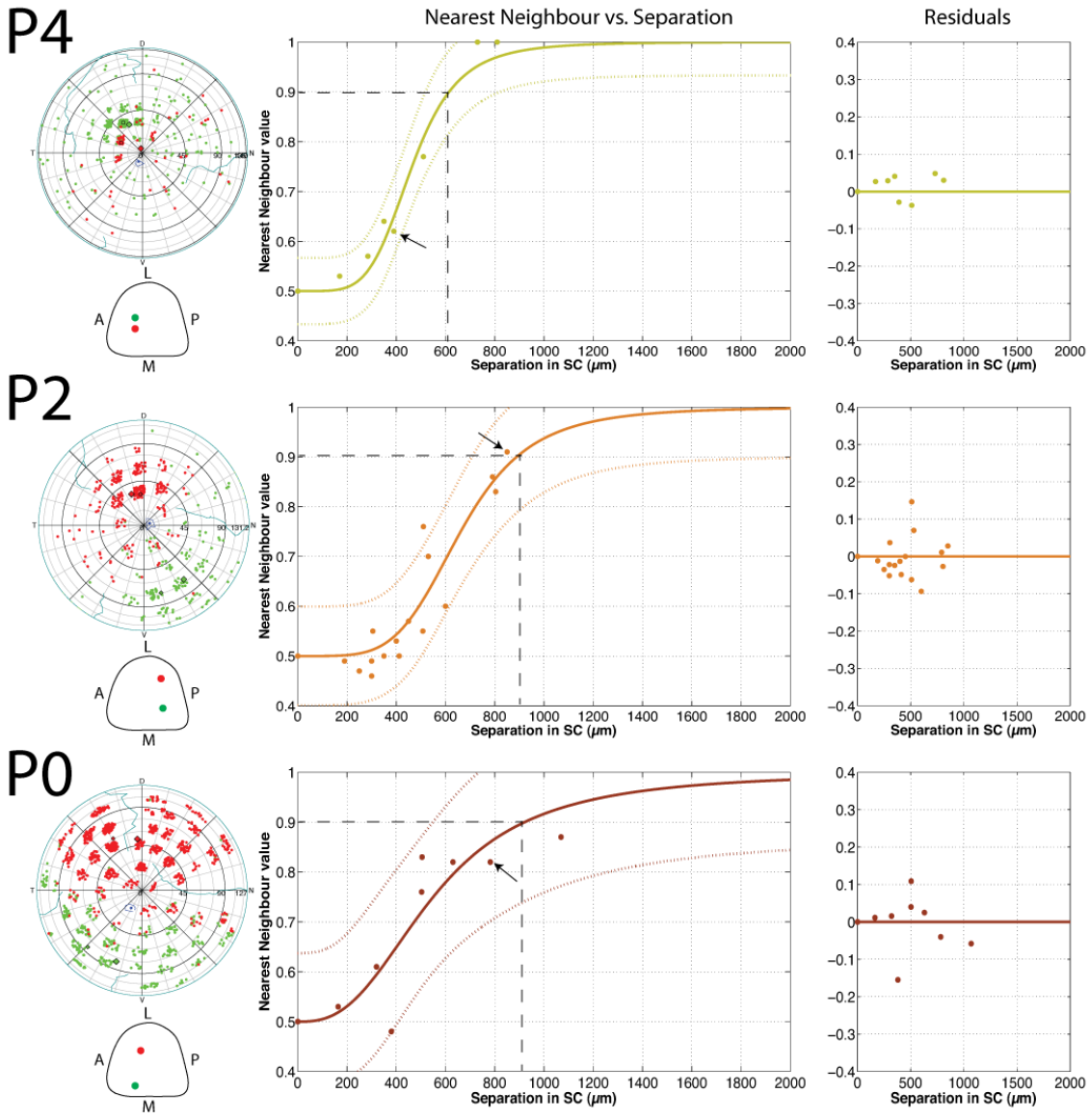

Figure 4-8 Early development of ML order in the projection

Overlap of the label measured by nearest neighbour analysis for P0-P4 plotted against separation of injection sites along the ML axis of the SC. Line fits are logistic curves defined by Equation 2-13. The black dashed line shows the separation at which label is 90% separate. The right hand plot represents the residuals associated with the fit, which as can be are symmetrical around the zero-line. Dashed line indicates the 95% confidence interval for the fitted curves. The arrow indicates the nearest neighbour value of the associated example retina. Values for the slope, inflection, $x_{(y=0.9)}$ and goodness of fits are in Table 4-1

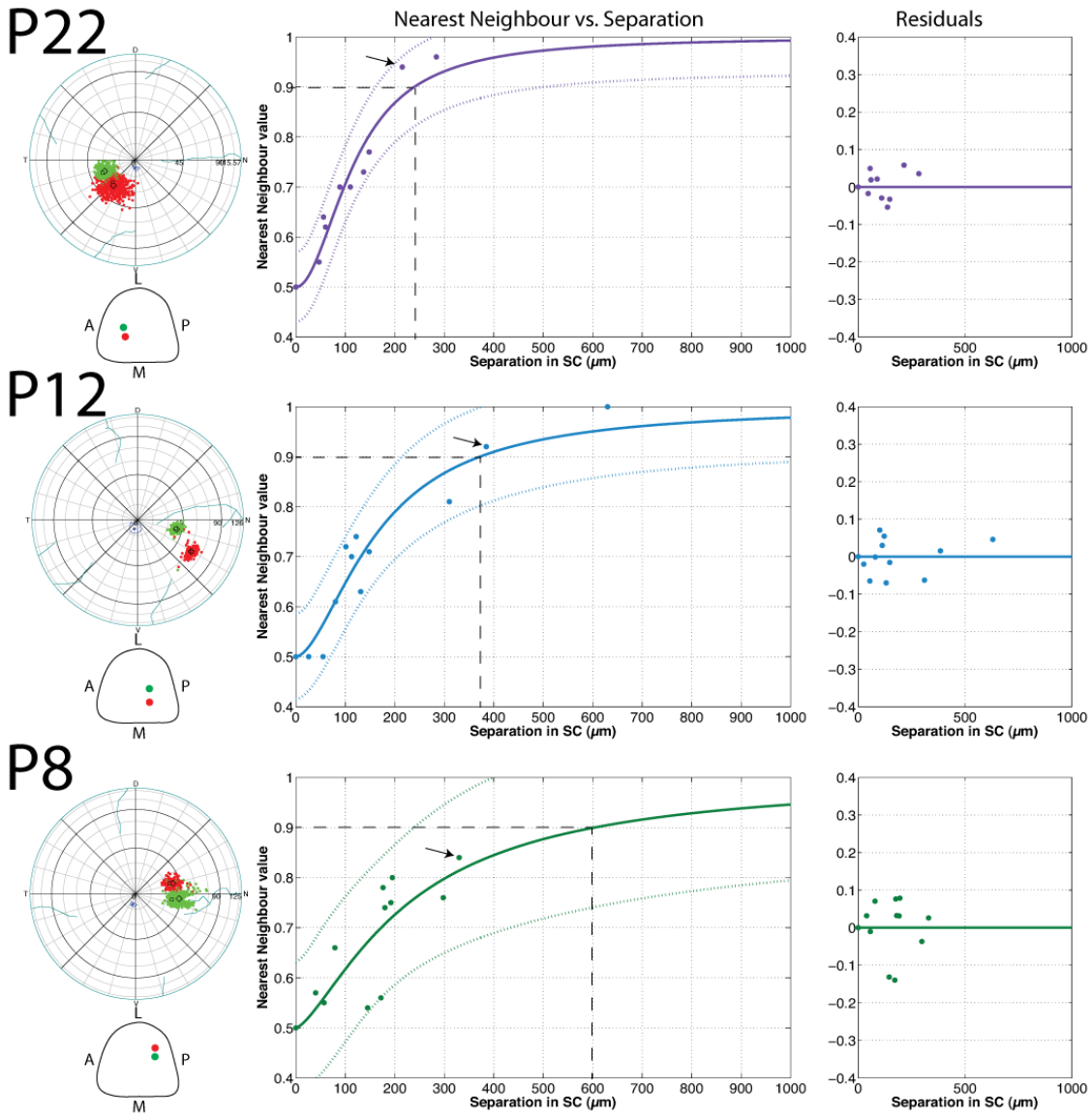

Figure 4-9 Late development of ML order in the projection

Overlap of the label measured by nearest neighbour analysis for P0-P4 plotted against separation of injection sites along the ML axis of the SC. Line fits are logistic curves defined by Equation 2-13. The black dashed line shows the separation at which label is 90% separate. The right hand plot represents the residuals associated with the fit, which as can be are symmetrical around the zero-line. Dashed line indicates the 95% confidence interval for the fitted curves. The arrow indicates the nearest neighbour value of the associated example retina. Values for the slope, inflection, $x_{(y=0.9)}$ and goodness of fits are in Table 4-1

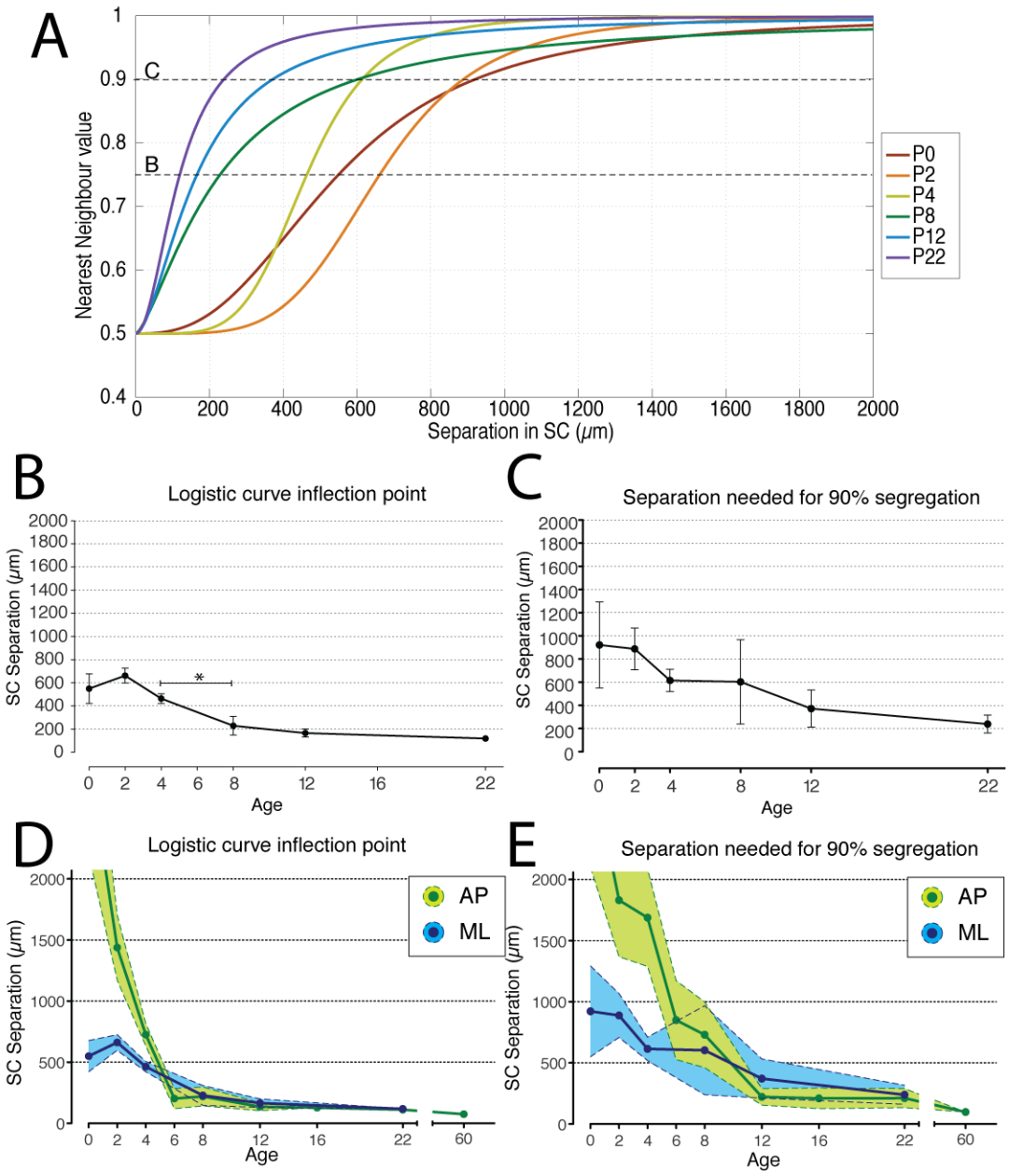

Figure 4-10 Development of ML order in the projection

A, Plot of NN value of retinal label as a function of the SC injection separation along the medial-lateral axis for injections separated along this axis. Curves are from the fits detailed in Figures 4-7 and 4-8 **B,** Slope of straight part of logistic curve fit (κ in Equation 2-13) plotted as a function of age. **C,** The SC injection separation needed to get 90% segregated foci in the retina (Y=0.9) according to the fits in A. **D-E,** Comparisons of slope (D) and 90% segregation threshold for fits (E) to AP (green) and ML (blue) SC axes. Error measurements in B-E are based on the 95% confidence intervals for the fits to each age.

		Logistic fit (eqn. 2-13)				
Age	***n***	**slope (κ)**	**inflection (τ)**	**$x_{(y=0.9)}$**	**SSE**	**R^2**
0	8	1.689	550	922	0.0436	0.830
2	17	2.695	662	888	0.0518	0.882
4	7	2.936	464	615	0.00861	0.973
8	12	1.431	229	603	0.0592	0.751
12	12	1.718	166	372	0.0249	0.927
22	10	1.995	120	239	0.0131	0.948

Table 4-3 Fitting curves to ML nearest neighbour data

Values for fitting of Sigmoid (Equation 2-14) to nearest neighbour data.

4.4 Development of Topography

Topography can be examined in several ways; an example of this is to plot the location of the label according to their respective injection location, such as the plot for adult topography in Figure 3-7. However, since the projection in the neonatal animals is so diffuse, this approach wouldn't work as well. Moreover, because it is not possible to get completely segregated label at P0, we need another way to determine whether any topography is present at birth. For this reason, I have done the vector plots in Figure 4-10 to try and examine the immature topography. The plots are done by connecting the Karcher means or peak densities of the label from paired injections in the same animal with an arrow pointing toward the most anterior of the two injection sites (See examples in Figure 4-11). In this manner, it is possible to investigate whether we can predict the orientation of the label based purely from the orientation of the injection sites. As can be seen for P0 in Figure 4-10, it is indeed possible to predict the orientation of the label from the orientation of the injection sites. Even for relatively closely spaced injections.

It is worth noting that using these plots, it is also possible to estimate the relative distance of the peak densities, but not necessarily the Karcher means, based on the injection site separation. By examining the length of large (brown) and small (orange) separations, we see that the large injection separations result in longer vectors than the small injection separations for the peak densities, but not always for the Karcher means. Generally, for both P0 and P2 this holds true for injection pairs with a difference of more than 400 μm. It is interesting that this is not necessarily the case if using the Karcher mean, which indicates that the peak density is the better way of determining the mature topography from diffuse immature projections.

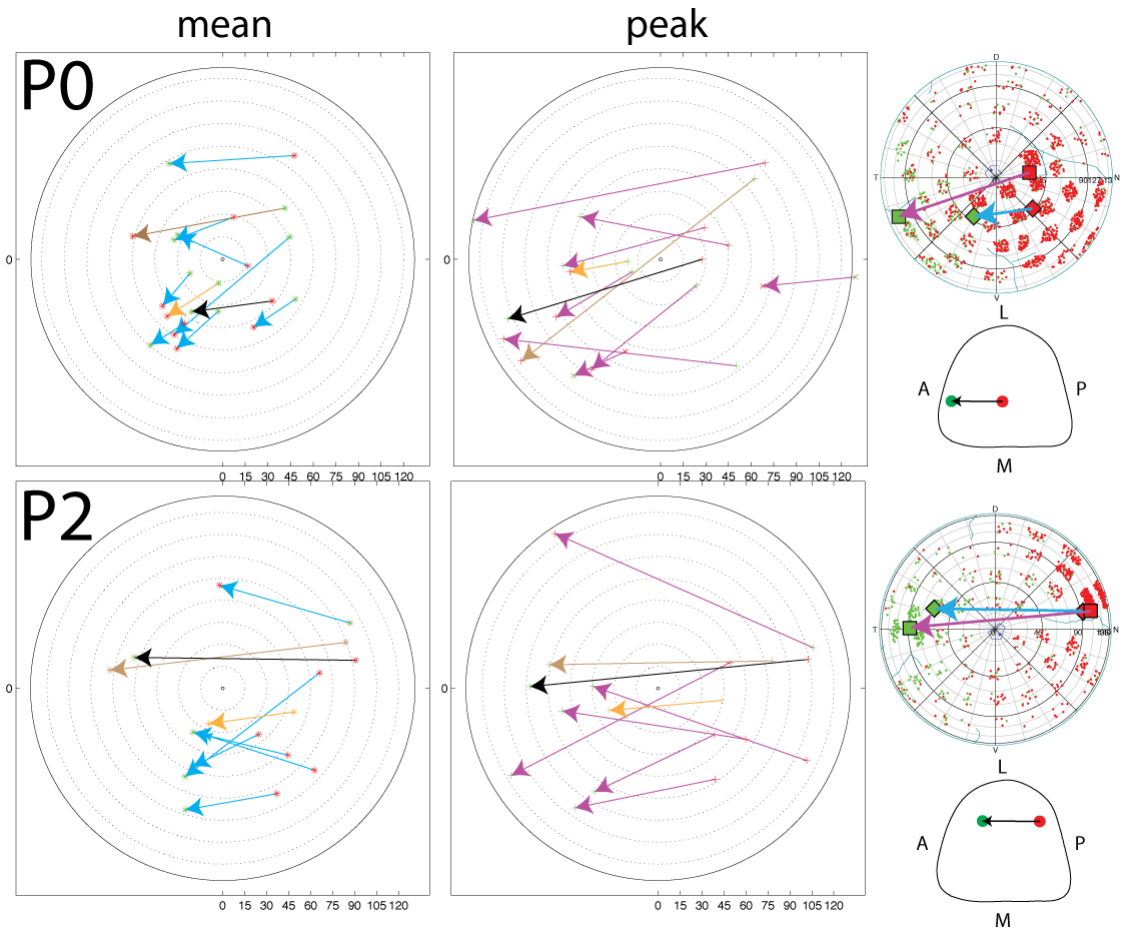

Figure 4-11 Vector analysis of P0-P4

Vectors connecting the Karcher means or Peak kernel density (KDE) of the label from two paired injections in the same animal for P0, & P2. The arrow is pointing towards the more anterior injection site. Plots are Azimuthal equidistant polar plots. The black arrow in the composite plots is the one in the example. The brown arrow is the one representing the largest separations (1720 µm at P0 and 1384 µm at P2) and the orange arrow represents the smallest separations (380 µm at P0 and 300 µm at P2) plotted. In the example plots, the vector connecting the Karcher means is blue and the vector connecting the KR peak densities is magenta. The locations of the respective SC injection sites are plotted underneath

4.5 Discussion

An interesting observation from the neonatal development is that there appears to be different phases of the refinement, with an initial reduction of label chiefly along the NT retinal axis, represented by the decrease in the extent of the 5% isodensity contour along the NT retinal axis for P0 to P6 (Figure 4-1). The functions describing the nearest neighbour measurements for the same neonatal animals also corroborate these observations, as initially there is no real order in the AP axis (Figure 4-6A), while the ML axis is significantly more ordered (Figure 4-9E), but by P6 the two axes are symmetrical. This initial refinement of the AP axis is then followed by a symmetric decrease in the size of the focus represented by the 50% isodensity contour between P4 to P12, as can be seen in Figure 4-1.

This anisotropy is most pronounced at birth, when the projection is much less precise along the AP axis than the ML axis, as injections separated along the ML axis only need to be separated by at least 922 μm to result in segregated label (Figure 4-8), which is not possible along the AP axis. This difference reflects the overshoot of axons along the entire AP length of the SC (Nakamura and O'Leary, 1989) combined with the ML order present in the brachium of the tectum at birth (Plas et al., 2005) due to the bundling of axons in the optic tract according to their approximate DV retinal position (Chan and Guillery, 1994).

As a consequence of this difference, the majority of early refinement occurs along the AP axis to establish the symmetric projection seen from P6 (Figure 4-10 D&E). Preferential refinement along one axis would suggest that different mechanisms could be in play to facilitate the extra AP refinement. These observations are supported by evidence that the characteristics of the nAChR-dependent waves during the first postnatal week are such that they would cause preferential refinement of projections spreading over 800-1000μm along this axis (Stafford et al., 2009).

It is worth keeping in mind that even though the projection at birth covers the entire AP axis, it is still possible to predict the orientation of the retinal label purely from the orientation of the injection sites (Figure 4-10). Increased branching in a discrete area would cause there to be more branches with terminals in this region (Yates et al., 2001) and therefore cause the higher uptake of label in a specific area that we see at P0 and P2 already. This dataset therefore supports the theory that there is preferential branching in approximately the correct target area, which could be caused by axons reaching a threshold for branch promotion regulated by the interaction of P75 and TrkB with ephrin-A5, which at the appropriately low concentration of ephrin-A5 will promote branching (Marler et al., 2008; Lim et al., 2008b; Marler et al., 2010).

Although it is certainly possible to get completely segregated label from paired injections separated along the AP axis at P4 (Figure 4-4). Whether it is possible at P2 is not as certain. Although the fitted function indicates that it is possible, since there is a lot of scatter at this age, i.e. injections separated by 1300µm resulted in an NN value of 0.5, this is not certain. It is possible that this variability is due to inherent variability in the development between animals, and the fact that there is some variation in the actual age of the animals (which may vary by up to 12 hours).

The second phase of the refinement involves the establishment of a clear focus in the topographically appropriate location, represented by the isodensity contour levels of 50% or higher. This phase of development is most apparent between P4 and P8 (Figure 4-1), as is also apparent from anterograde tracing (McLaughlin et al., 2003b) and probably involves further local branch-extension, which would increase the uptake of label in a defined area, as we see in Figure 4-1. The extension and retraction of branches involved in this process has been shown to be mainly activity-dependent (Debski and Cline, 2002; McLaughlin et al., 2003b; Fredj et al., 2010). Similarly for the ML axis, since axons have been reported to extend and stabilise long branches along the ML axis of the SC (Hindges et al., 2002), it is likely that the refinement seen during this period in the nearest neighbour data for the ML axis (Figure 4-10) reflect branching and not redirected growth.

The later development involving the removal of residual ectopic cells is most obvious between P6 to P8, where most of the ectopically projecting cells are removed. In most likelihood, this is a process that takes place throughout the first post-natal week, but just reaches a threshold that makes it more apparent at this more mature stage. The mechanisms behind the removal of these projections is likely to involve a combination of extensive axon branching (Hindges et al., 2002) and cell death; since almost half of RGCs born die during this period (Farah and Easter, 2005). It is possible that apoptosis plays a direct active role in refining the projection by way of removing cells that do not make topographically appropriate projections. Such cells may have a higher probability of activating an apoptotic pathway as a consequence of being outcompeted for sources of neurotrophins or due to direct interactions between receptors in the apoptotic pathway (Lim et al., 2008b; Marler et al., 2010; Vanderhaeghen and Cheng, 2010). It has, however, also been argued that cell-death simply causes the baseline "noise" to be removed, thus causing the area with highest density of appropriately connected cells to remain (Upton et al., 2007). It is possible that these are simply two sides of the same issue and it is just a matter of probability. While there probably are RGCs with topographically appropriate connections that still die due to competition etc., it seems probable that RGCs that have made guidance errors are more likely to be actively removed, especially since spontaneous activity has been shown to promote survival in the SC (Galli-Resta et al., 1993).

Interestingly, even after these initial phases of development have refined the focus to resemble adult sizes, there is still a significant difference in the separation of paired injections needed to get segregated label between P22 and adult mice, that was not picked out by using qualitative nor isodensity contour analysis. Since the post-eye opening critical period is associated with increased synaptogenesis in the cortical projection (Hooks and Chen, 2008), it could suggest a further role for increased synaptogenesis in refining the precision of the collicular retinotopic map. It is, furthermore, possible that the establishment of feedback from the cortico-collicular

projection, which establishes connectivity during this period (Phillips et al., 2011), also influences the precision of the retino-collicular projection enabling further refinement.

Chapter 5 Spontaneous Activity in Retinocollicular Development

5.1 Introduction

The relative contribution of molecular cues and instructive spontaneous activity during development and whether they are mutually exclusive events or somehow interact is largely unknown. Further, it is not clear that our current understanding of actual molecular components and spontaneous or sensory modulated activity represents the full complement of mechanisms involved at all scales of the constructed circuit (Mrsic-Flogel et al., 2005; Rashid et al., 2005; Cang et al., 2008b).

To examine the role of patterned activity in the early development of topography we have utilised a global knockout of the β2 subunit of the nicotinic acetylcholine receptor (nAChR-β2). This mutant has altered spontaneous activity patterns in the retina and the β2-subunit is therefore believed to be crucial for generating the specific pattern of correlated activity waves seen in the retina from P0-P8 (Bansal et al., 2000; Sun et al., 2008b). Moreover, this mutant has also been shown to have mapping defects in the visual system (McLaughlin et al., 2003b; Grubb and Thompson, 2004; Mrsic-Flogel et al., 2005; Shah and Crair, 2008a), as discussed in the introduction.

Importantly, the spatiotemporal characteristics of the nAChR-dependent wave-form activity in wild-type and the gap-junctional wave-form activity in the nAChR-β2 -/- are both well-characterised although there is some disagreement about the details of spiking rates (Sun et al., 2008a; 2008b; Stafford et al., 2009). However, since the general characteristics of the waves are consistent between studies and the differences can be largely accounted for by variations in the *in vitro* experimental setup (Stafford et al., 2009), the data can therefore be used in modelling to make predictions about the patterns of activity needed for the instructive roles of the waves. However, again although the projection patterns to the SC in this mutant have been demonstrated already, previous descriptions are based on anterograde tracing and provide largely

qualitative descriptions. The main reason for undertaking this quantitative analysis of the nAChR-β2-knockout strain is therefore to provide a more detailed quantitative description to inform further modelling studies, which will be discussed in Chapter 6.

5.2 Results

5.2.1 Development of precision in nAChR-β2 knock out animals

Examples of retinae following single discrete injection of Retrobeads into the anterior SC of nAChR-β2 knockout animals at different stages of postnatal development are shown in Figure 5-1. An injection at P0 will result in the entire retina containing labelled cells. The 5% isodensity contour spans most of the retina, with the 25% contour-level covering the entire NT axis and approximately half of the DV axis (Figure 5-1, P0). The distribution of label that is similar to the one in the P0 C57BL6/J wild-type example in Figure 4-1. As in the wild type, the Karcher mean of the label is displaced nasally to the peak density.

When doing a similar injection at P2, the general picture is much the same and is also mostly the same as the wild type. The 25% isodensity contour still spans the entire NT axis and covers approximately 50% of the DV axis. However, there is no longer a single focus enclosed by the higher (50% and above) isodensity contours, but two. Separate areas with higher density is seen in approximately half of anterior injections in nAChR-β2 knockout animals between P0 and P4, but has not been observed in wild-type animals of the same ages. For injections done at P4, the 5% isodensity contour still spans the entire NT axis and the label is generally indistinguishable from injections done at P2.

The example of labelling after an injection at P8, which marks the end of cholinergic spontaneous correlated activity, shows a pattern that might be described as having a focus, although it is still very much larger than the one in wild-type animals. The examples shown of injections made at later ages show a large degree of anisotropy. Although the orientation is not uniform, the general trend is for the label to be wider along the NT axis, suggesting that the projection is elongated along the SC AP axis. However, further analysis is necessary to establish this. As can be seen for the P22 example retina, although the knockout animals often have a somewhat symmetric focus

(represented by the 50% contour-level), the 5% is generally asymmetric and spans a considerably larger area than the 25% isodensity contour, suggesting a differently shaped distribution to the wild-type.

In the knockout the 25% contour covers around 20% of the retina (Figure 5-2B), whereas in the wild type it typically covers less than 5% (See Figure 4-2B). Qualitatively, the label in the P8 nAChR-β2 knock-out animals is more reminiscent of the label at P4 in wild-type animals. There appears to be a steady refinement from P8 to P22 with the focus getting gradually more defined and smaller, although still noticeably larger than age-matched wild-type animals. Not only do the contours remain noticeably larger, but even at P22 the 5% isodensity contour covers a much larger area than the 25% contour, which is in stark contrast to the wild-type animals, where the 5% and 25% isodensity contours converge at P12, after which there is a defined focus. Interestingly, the difference between the 5% and 25% isodensity contour persists into adulthood. In contrast to adult wild-type animals, the 5% isodensity contour in nAChR-β2 knockout animals typically still covers twice the area of the 25% contour.

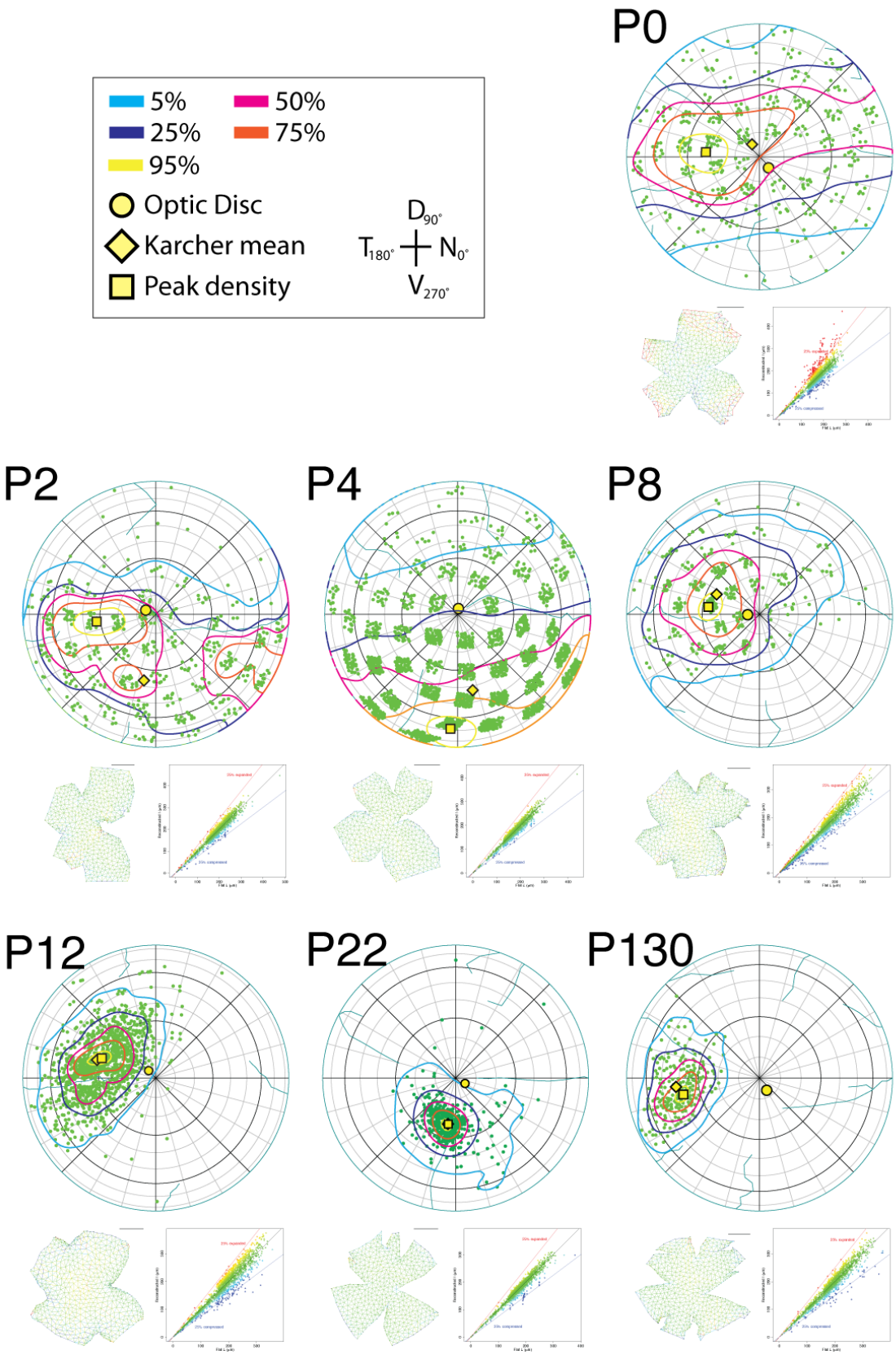

Figure 5-1 Examples of label in the nAChR-β2 -/- during development

Figure 5-1 Legend: Examples of label in the nAChR-β2 -/- during development (previous page)

Label resulting from single discrete injections of a comparable size into the anterior superior colliculus at different stages of postnatal development. Isodensity contours are plotted by excluding 5% (light blue), 25% (dark blue), 50% (pink), 75% (orange) & 95% (yellow) of the cells with the lowest density using either KR estimates where partial sampling is used or KD estimates where retina is fully sampled (See Section 2.3.1 for details). All plots are Azimuthal equal-area plots using the rim-angle for the respective age (values for φ_{95} are given in Table 2-3). Yellow circle is OD, square is the peak density and diamond is the Karcher mean of the label. Small plots for each retina represents the distortions involved in reconstructing the retina. These are the original flat-mounts (left) and scatterplot of reconstructed vs. original segment length (right) colour-coded for expansion (red) and compression (blue)

5.2.2 Measuring isodensity contours in nAChR-β2 knockout animals

Individual examples, such as those in Figure 5-1 are good for gaining an overview of the immediate effects of a mutant. However, to properly understand the effects of any subtle alterations to dynamics of the system, such as the changes in activity patterns evoked by removing the β2 subunit from nicotinic acetylcholine receptors, as is the case in Figure 5-1, it is necessary to quantify as many aspects of the development as possible. To that effect, we have initially plotted isodensity contours as described earlier. The quantification of the projection enabled by these contours enables the comparison of data from multiple animals and by extension the comparison of different groups of animals, such as animals of different ages and with varying genotypes.

In the case of the nAChR-β2 knockout animals, the quantitative contour analysis in Figure 5-2 reveals that a single discrete injection of retrobeads into the SC just after birth (P0) results in almost all the retina containing labelled RGCs (85.0±10.1%) and the 5% isodensity contour covers 61.3±16.5% of the retina (Figure 5-2A). As mentioned in relation to Figure 5-1, it is difficult to pick out a focus of denser label at this age, which is also reflected in the 50% isodensity contour covering 18.3±7.2% of the retina.

The distribution of label is very similar to P0 at both P2 and P4. At P2 89.7±4.1% of the retina contains labelled cells, the 5% contour covers 67.1±11.5% and the 50% contour 21.0±8.1% of the retina. Similarly at P4, 86.1±16.7% of the retina contains labelled cells. Also the 5% and 50% contours, covering 72.1±20.6% and 19.7±9.7% of the retina, respectively. After P4, the amount of retina containing labelled cells is reduced significantly ($p<0.001$) to 63.3±13.4% at P8. There is, moreover, also a significant reduction in the size of the 5% contour level to it covering just 35.9±11.1% of the retina ($p=0.0015$). Additionally, all the higher-level contours are refined at a similar rate, so that the distribution of the label at P8 is still similar to that of P4, albeit covering a smaller proportion of the retina.

Between P8 and P12, there is a significant reduction in the amount of retina containing labelled cells ($p<0.0001$) to 35.2±9.0%. There are, however, no significant reductions in the sizes of any of the contours between P8 and P12. Although there are no reductions in the isodensity contours between P8 and P12, there is, however a significant reduction in the sizes of the 5% ($p=0.0025$) and 25% ($p=0.0035$) isodensity contours from P8 to P22, which indicates that the refinement continues at a slower rate. Furthermore, since there are no significant differences in the higher-level contours, it could indicate that there is a significant refinement purely of the ectopic cells during this period.

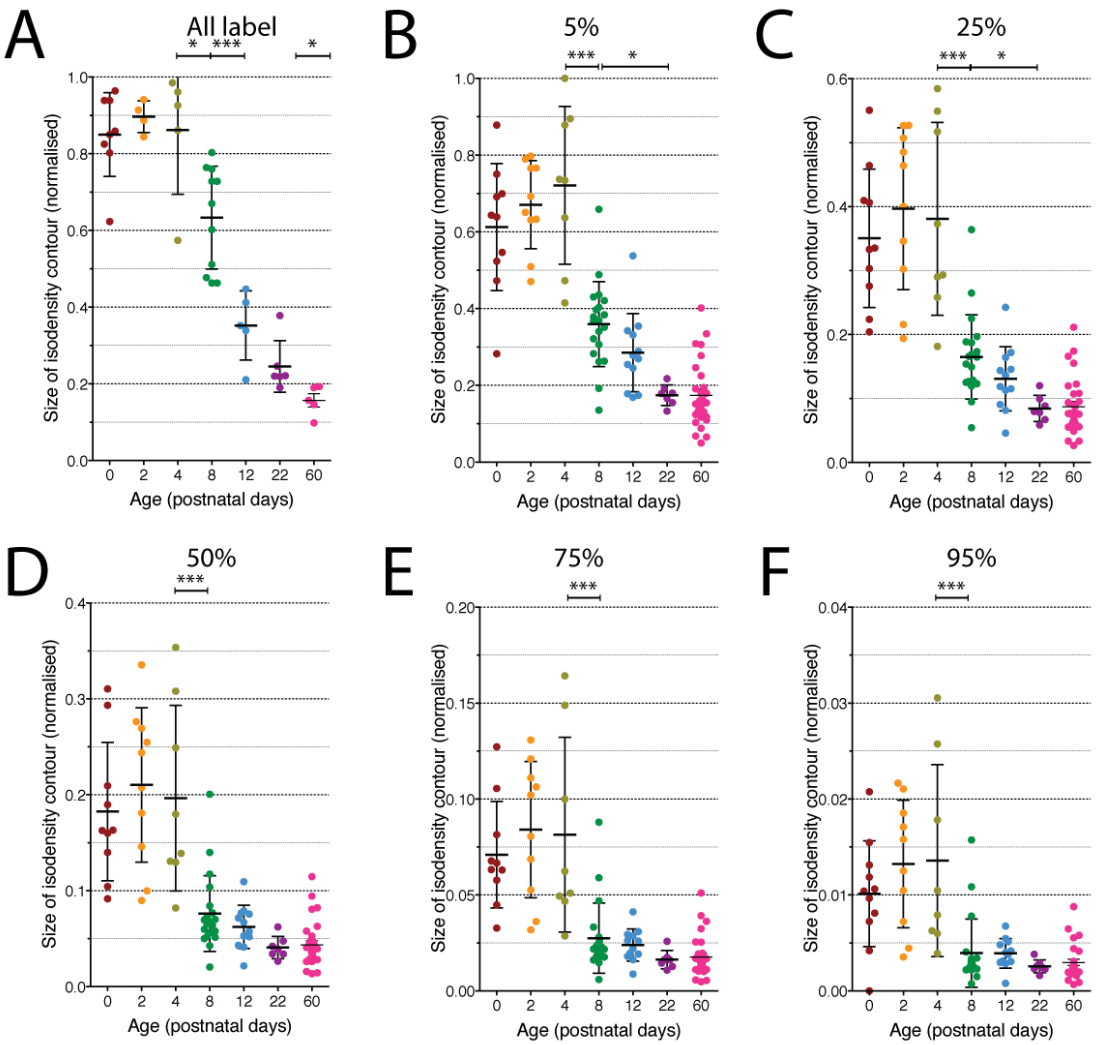

Figure 5-2 nAChR-β2 knock-out isodensity contour analysis.

A, Proportion of retina containing any labelled cells from Systat analysis (see methods), hence why the *n* is lower. **B-F,** Scatterplots with the sizes of the isodensity contours for 5% (A), 25% (B), 50% (C), 75% (D) & 95% (E). Areas have been normalised to the size of the retina in deg^2 (Equation 2-10). Line is the mean and error bars are SD. Significance determined using a one-way ANOVA with a Bonferroni post-hoc test. **F,** Mean data from A-E plotted on a log scale to illustrate that the curves for all contours are of similar shape.

The isodensity contours are summarised in Figure 5-3. When plotting all the contours in one plot, it is apparent that overall the pattern of refinement with age for all the contour-levels is similar, since there is a period of refinement between P4-8 in all the contours. However, although the pattern of refinement appears similar in this plot, for the contour levels above 50%, there are no longer any significant differences in the later development. In Figure 5-3, it is possible to compare the relative sizes of the contour-levels at different ages. The difference between the 5% and the 25% contour levels also remains relatively constant throughout development, as the 5% contour is 2.1 times the size of the 25% contour at P0 and 2.4 times at P22. Interestingly, there are no significant differences between the amount of the retina containing any labelled cells and the 5% isodensity contour. This is different from wild type (Figure 4-4), where there is a difference until P12.

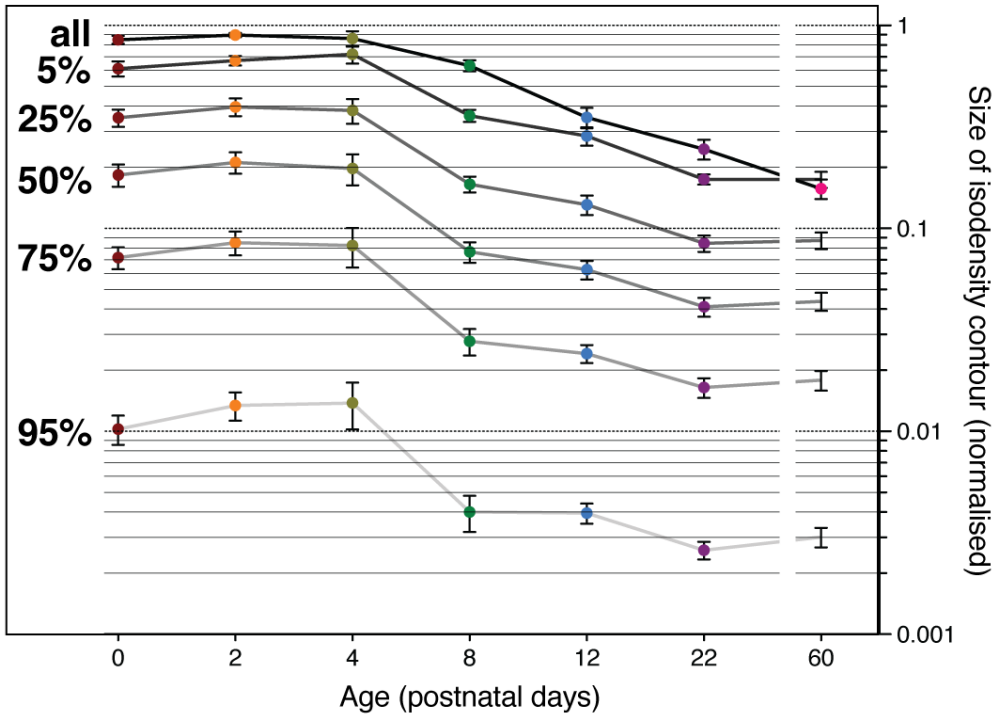

Figure 5-3 nAChR-β2 knock-out isodensity contour analysis.

Mean data from Figure 5-2 plotted on a log scale to illustrate that the curves for all contours are of similar shape.

Age	*n* *(KRE/KDE)*	Contour level	Mean size (normalised)	Median size (normalised)	SEM	SD
0	10 (2/8)	5%	0.6127	0.6412	0.05227	0.1653
		25%	0.3506	0.3341	0.03423	0.1083
		50%	0.1825	0.1629	0.02281	0.07214
		75%	0.07102	0.06494	0.008782	0.02777
		95%	0.01013	0.01040	0.001663	0.005515
2	10 (3/7)	5%	0.6707	0.6716	0.03627	0.1147
		25%	0.3969	0.4322	0.03998	0.1264
		50%	0.2104	0.2257	0.02546	0.08051
		75%	0.08409	0.09133	0.01123	0.03550
		95%	0.01323	0.01415	0.002100	0.006642
4	8 (6/2)	5%	0.7211	0.7355	0.07265	0.2055
		25%	0.3809	0.3331	0.05333	0.1508
		50%	0.1965	0.1595	0.03417	0.09665
		75%	0.08135	0.05663	0.01795	0.05077
		95%	0.01358	0.009191	0.003536	0.01000
8	20 (16/4)	5%	0.3594	0.3681	0.02475	0.1107
		25%	0.1650	0.1593	0.01475	0.06596
		50%	0.07620	0.06656	0.008820	0.03944
		75%	0.02746	0.02239	0.004083	0.01826
		95%	0.003942	0.002733	0.000796	0.003560
12	12 (0/12)	5%	0.2852	0.2738	0.02942	0.1019
		25%	0.1308	0.1276	0.01447	0.05014
		50%	0.06230	0.06233	0.006549	0.02269
		75%	0.02389	0.02406	0.002423	0.008394
		95%	0.003899	0.003890	0.000443	0.001537
22	7 (0/7)	5%	0.1744	0.1785	0.01015	0.02685
		25%	0.08440	0.07968	0.007782	0.02059
		50%	0.04086	0.03909	0.004377	0.01158
		75%	0.01626	0.01625	0.001813	0.004796
		95%	0.002557	0.002429	0.000256	0.000678
60	29 (0/29)	5%	0.1741	0.1548	0.01578	0.08495
		25%	0.08713	0.07641	0.008217	0.04425
		50%	0.04346	0.03743	0.004428	0.02385
		75%	0.01766	0.01552	0.001960	0.01055
		95%	0.002969	0.002650	0.000327	0.001765

Table 5-1 Isodensity contour analysis of the projection in nAChR-β2 -/- animals

Data of the sizes of the isodensity contours in Figure 5-3 from individual injections at various ages from P0 to P22. *n* reflects the number of injection and numbers in brackets represent the ratio of KRE versus KDE contouring.

To establish the effects of removing the beta2 subunit of the Nicotinic Acetylcholine Receptor (nAChR-β2), the whole developmental dataset has been compared to the wild-type data detailed in Chapter 4. An interesting and somewhat surprising aspect of the contour-analysis in Figure 5-3 is that the amount of retina containing labelled cells is smaller in the knockout than the wild type at birth (p=0.02). This is confounded by the fact that the 5% isodensity contours are larger in the nAChR-β2 knockout animals even at birth. From P2 to P4 the same amount of retina contains labelled cells in knockout and wild type, but the 5% isodensity contour remains larger. By P8, more of the retina contains labelled cells in the knockout than the wild type.

A useful measure of the shape of the label is the differences in size between the different contour-levels for each given age. When looking at the relative sizes of the contour-levels at different ages (Figure 5-2), the difference between the 5% and the 25% contour levels remains relatively constant throughout development, as the 5% contour is 2.1 times the size of the 25% contour at P0 and 2.4 times at P22. This is slightly different from the wild type, where the 5% contour is 1.4 times the size of the 25% contour at P0, but 2.1 times at P22. A similar pattern is seen when comparing the higher contour-levels.

Furthermore, comparing the 5% contour-level, signifying the ectopic cells, to the 50% contour-level, representing the size of the focus; it is apparent that the nAChR-β2 knockout animals have a more diffuse projection throughout development than the wild-type animals, as the mean contour size ratio in nAChR-β2 knockout animals for P0-4 is 5.8±0.6 (SD) compared to 3.0±0.3 in wild-type animals; and for older animals (P8 to P22) the ratio for nAChR-β2 -/- animals is 6.4±0.5 compared to 4.4±0.3 in wild type animals. Another aspect that is noticeably different between knockout and wild type animals is the variability of the label. For the knockout animals, there is greater variability in the young animals (P0 to P4) than in the older animals, but the even in older animals, the variability is greater than the wild type. On average, the standard deviation of the knockout animals is 3 times that of the wild type, which may be due to the correlated information in the wild type reducing noise in the system.

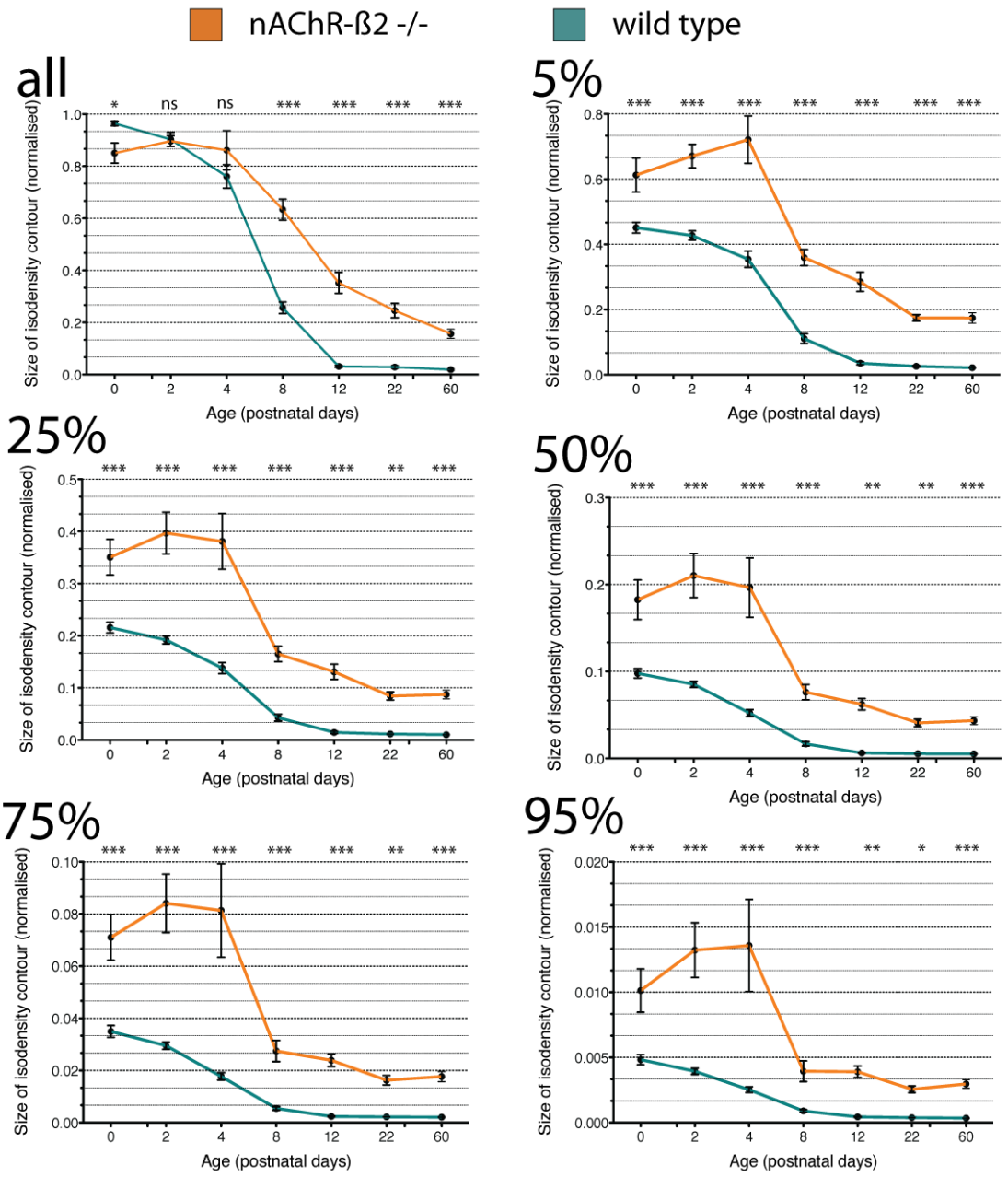

Figure 5-4 Comparison of isodensity contours for nAChR-β2 -/- and +/+

Plots of the proportion of the retina containing labelled cells (all) and the normalised mean retinal area enclosed by each of the 5%, 25%, 50%, 75% & 95% isodensity contours in Figure 5-2. nAChR-β2 knockout animals are in orange and age-matched wild-type animals are in green (Figures 4-2 & 4-3). Error bars represent the standard error of the mean. Significance is determined with a two-tailed one-way ANOVA with a Bonferroni post-hoc test (*** $p<0.0001$; ** $p<0.001$; * $p<0.05$)

5.2.3 Measuring order in nAChR-β2 knockout animals

Although the isodensity contours have proven to be a good method for observing phenotypes in the precision of the projection, the nearest neighbour analysis provides an additional insight into the topographic order in the projection.

In Figure 4-7, we saw that for the wild type animals, the required separation between two injections to ensure non-overlapping retinal label varied with age (Figure 4-7). Figures 5-5 (P0-P4) and 5-6 (P8-P60+) illustrate the results of this analysis in the nAChR-β2-knockout line. The study was confined to anterior-posterior axis, as this is where the greatest phenotype might be expected considering previous reports (McLaughlin et al., 2003b). The individual animals (Figure 5-1) and population data shown in Figure 5-3 show that, in contrast to wild type animals, in this line there is no difference between the spread of labelled cells following injections at P0, P2 and P4.

The nearest neighbour analysis in Figure 5-5 confirms that the observed similarities between the early ages in the contour analysis are also reflected in this analysis. At P0, a pair of injections separated by 1500μm resulted in a nearest neighbour value of 0.55. As can be seen in the P0 example in Figure 5-5, both the red and green label covers the entire retina and therefore this example where injections are separated by 642μm results in a similar nearest neighbour value of 0.52. This is similar for the P2 example, where injections at 1480μm also result in a nearest neighbour value of 0.55 and the entire retina still contains labelled cells, although in this case dorsal retina is less heavily labelled which is consistent with the medial location of the injections. Unlike the wild type example, the pattern in the P4 case is indistinguishable from that at P2: injection separations of 1536μm here resulted in a nearest neighbour value of 0.50 (Figure 5-5). Moreover, at this age the entire retina also still contains labelled cells (Figure 5-5). As a result of the scattered projection patterns at these early ages, the logistic functions fitted to the data do not show the classical S-shape within the bounds of the SC and the given NN value predicted from these fits is less than 0.6 for the whole of the SC.

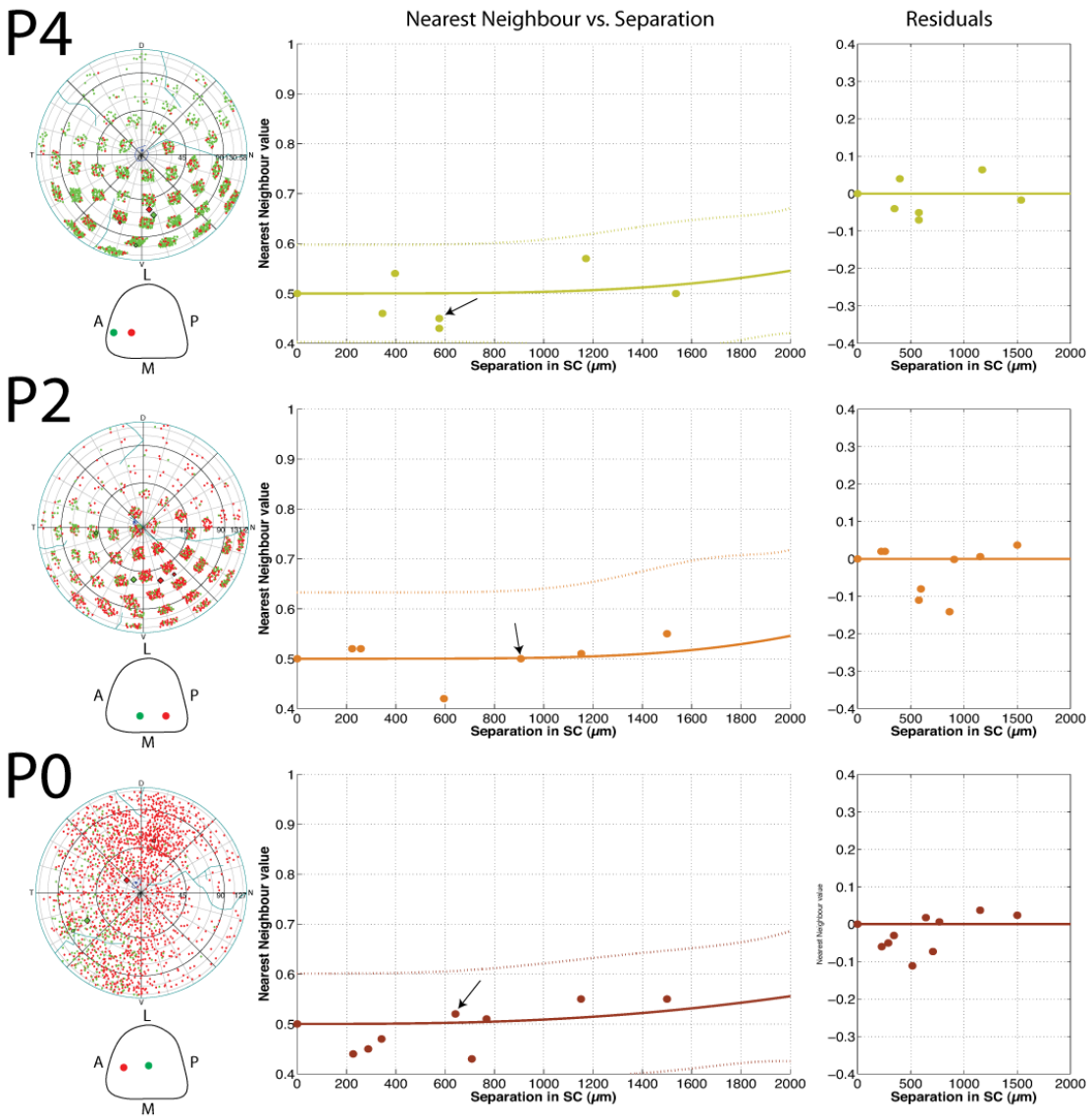

Figure 5-5 Lack of order in the early projection in the absence of nAChR-β2

Segregation of the label measured by nearest neighbour analysis for P0-P4 plotted against separation of injection sites along the AP axis of the SC. The fits are logistic curves defined by Equation 2-13. The black dashed line shows the separation at which label is 90% separate. The right hand plot represents the residuals associated with the fit, which as can be are symmetrical around the zero-line. Dashed line indicates the 95% confidence interval for the fitted curves. The arrow indicates the nearest neighbour value of the associated example retina. Values for the slope, inflection, $x_{(y=0.9)}$ and goodness of fits are in Table 5-2

Not surprisingly given the data shown in Figure 5-2, the projection becomes more ordered with age in older nAChR-β2 -/- animals (Figure 5-6). At P8, towards the end of the stage II nAChR-dependent waves, we find, as mentioned previously that 63.3±13.4% of the retina contains labelled cells, which can also be seen in the P8 example in Figure 5-6. The result of this is that the logistic function fitted to the nearest neighbour data shows that it might just be possible to achieve segregated label (y=0.9), albeit only at separations of 1989 µm, which approximately corresponds to the length of the SC. However, due to the lack of data for separations above 800µm, it is uncertain whether this is actually the case. It could be both that it is not possible to achieve segregated label and that it is possible to get segregated label from injections separated by 1000µm. More injections would be needed to determine this, however, even if it would be possible to get segregated label with injections of 1000µm, this is still significantly more than P12 nAChR-β2 -/- animals where injection separations of 640±126 µm are sufficient to get segregated label.

Although it is possible to get segregated label at P12, as can also be gleaned from the example in Figure 5-6, where 35.2±9.0% of the retina still contains labelled cells, it is still not a very precise projection. From P12 to P22, there are no significant changes in any of the aspects describing the fitted functions, as the functions for P12 and P22 animals have similar inflection points (409 and 453µm, respectively; Table 5-2) and slopes (3.1 and 3.7, respectively) and as a result, injections done at P22 still need to be separated by 662±265 µm to get segregated label. For adult animals, although the examples in Figure 5-6 look very similar to P22, the fitted function has a steeper slope (5.47) and as a result, in adult animals, injection separations of 518±122µm are needed in adult animals to get segregated label.

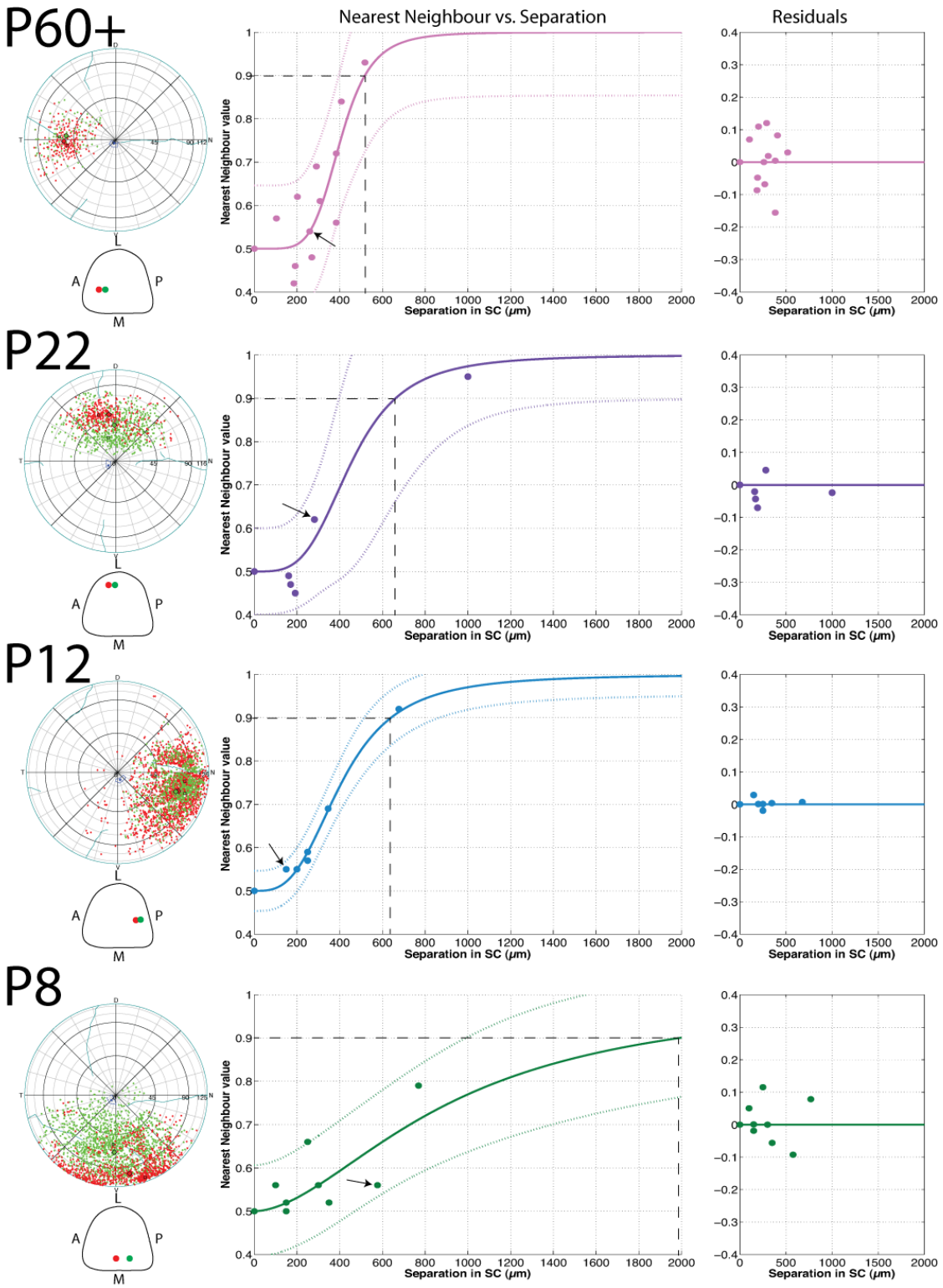

Figure 5-6 Order in the late projection in the absence of nAChR-β2

Figure 5-6 Legend: Order in the late projection in the absence of nAChR-β2

(previous page)

Segregation of the label measured by nearest neighbour analysis for P8-60+ plotted against separation of injection sites along the AP axis of the SC. The fits are logistic curves defined by Equation 2-13. The black dashed line shows the separation at which label is 90% separate. The right hand plot represents the residuals associated with the fit, which as can be are symmetrical around the zero-line. Dashed line indicates the 95% confidence interval for the fitted curves. The arrow indicates the nearest neighbour value of the associated example retina. Values for the slope, inflection, $x_{(y=0.9)}$ and goodness of fits are in Table 5-2

As can be seen from the plot of the nearest neighbour contours for all the sampled ages in Figure 5-7A, there is no order in the projection along the AP axis before P8. It is possible that order appears by P6, but this dataset has not yet been obtained. The logistic functions fitted to the data for P0, P2 and P4 all show an almost flat line at less than 0.6 for the entire length of the SC. It is only by P8 that some order emerges, as is also apparent from the fact that less than half of the retina contains labelled cells (Figure 5-1). Since the function now increases steadily it is more similar to wild type P2 or P4 than wild type P8. With the inflection points at 915±376 μm for P8 nAChR-β2 -/- and 726±92.5 for P4 wild type (Figure 5-7B); and the threshold for saturation of the function at 1989 μm and 1685, respectively (Figure 5-7C), the 95% confidence intervals for the functions fitted to the P8 nAChR-β2 -/- and wild type P4 data are nearly completely overlapping. Moreover, since the slopes of the two curves at 1.78 and 1.87 are also similar, we can say that the distribution is also similar, at least for the AP axis.

Although it is possible to get segregated label in the nAChR-β2 -/- animals at P12, it is still not a very precise projection and is more equivalent to P6 or P8 wild type animals. The main difference between the knockout and wild type animals, however, is that from P12 onwards, there is no significant refinement and as a result, injections done at P22 still need to be separated by 662±265 μm to get segregated label. The order is not even rescued in adult animals, since injection separations of at least 518±122μm are still needed in adult animals to get segregated label.

Interestingly, some of the differences between P22 and adult (P60+) animals that were observed for the wild type (Figure 4-7D) are also seen in the nAChR-β2 knockout data. At P22 the threshold for ordered label is at 662 μm, whereas it is at 518 in the adult population. However, since this difference is caused by an increase in the slope of the function from 3.67 to 5.47, the inflection points are more similar at 453 for P22 and 404 for adult. Although there may be an increase in the order of the projection from P22 to adult in the nAChR-β2 -/- animals, more data would be needed to establish this. Despite the smaller difference between P22 and adult, the adult projection is still significantly

less ordered in the knockout than in wild type. In adult wild type animals, SC injection separations of just 98 μm are sufficient to give separate foci of label in the retina, whereas in in the nAChR-β2 knockout animals separation of 518 μm are needed.

		Logistic fit (eqn. 2-13)				
Age	***n***	**slope (κ)**	**inflection (τ)**	**x $_{(y=0.9)}$**	**SSE**	**R^2**
0	11	1.81	4193	-	0.0273	0.00350
2	10	1.62	3287	-	0.0407	0.123
4	8	1.92	3599	-	0.0151	0.0221
8	12	1.78	915	1989	0.0345	0.788
12	8	3.10	409	641	0.00345	0.981
22	8	3.67	453	662	0.0123	0.951
60	15	5.47	404	518	0.0803	0.828

Table 5-2 Fitting curves to nAChR-β2 -/- nearest neighbour data.

Values for fitting of Logistic curve (Equation 2-14) to nearest neighbour data for injections separated along the anterior-posterior axis of the SC. (*) No value is given as it is far beyond the length of the SC, and any value would therefore be meaningless.

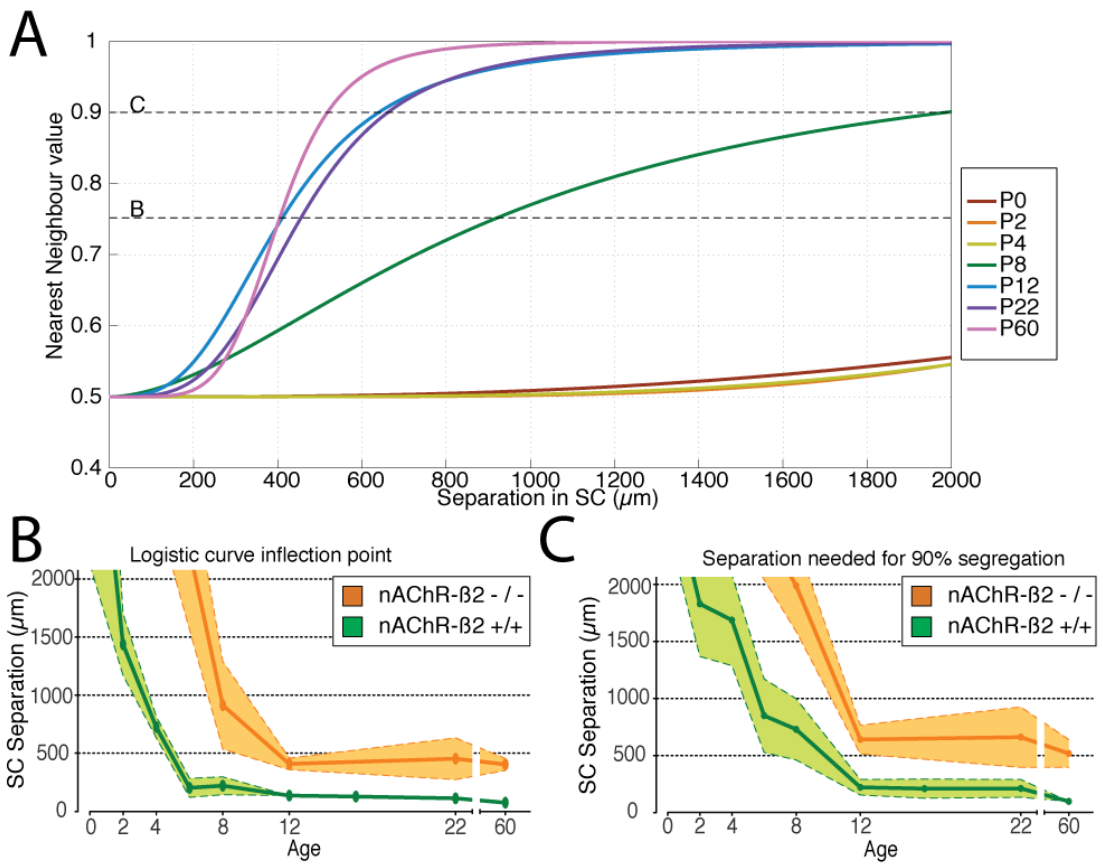

Figure 5-7 Summary of nAChR-β2 -/- order and comparison to wild type

A, Plot of NN value of retinal label as a function of the SC injection separation along the anterior-posterior axis. Curves are from the fits detailed in Figures 5-4 and 5-5. Dashed lines represent the data shown in B & C. **B**, Inflection point of the fitted curves in A plotted as a function of age for nAChR-β2 -/- (orange) and +/+ (green). **C,** The SC injection separation needed to get 90% segregated foci in the retina according to the fits in A. Error-bars in B-C are represent the 95% CI for the fitted function.

5.2.4 Comparing the nAChR-β2 genotypes

Throughout this chapter, I have compared the nAChR-β2 knockout animals to wild type animals on the same C57BL6/J background. However, to determine whether this is a reasonable comparison, the nAChR-β2 knockout animals have also been compared to heterozygous and wild type littermates (Figure 5-7). In Figure 5-7A, the sizes of the various isodensity contour levels have been plotted in histograms to show that there are no significant differences between the heterozygous (-/+) and wild type (+/+) littermates for P12, P22 and adult across all the contour levels. These two groups are, however, very significantly different (p<0.0001) from the homozygous (-/-) animals at all three ages and across all the contour levels. This can also be seen in the examples in Figure 5-7B, where the homozygous (-/-) retina has a significantly larger area with labelled cells than the heterozygous (-/+) and wild type (+/+) littermates.

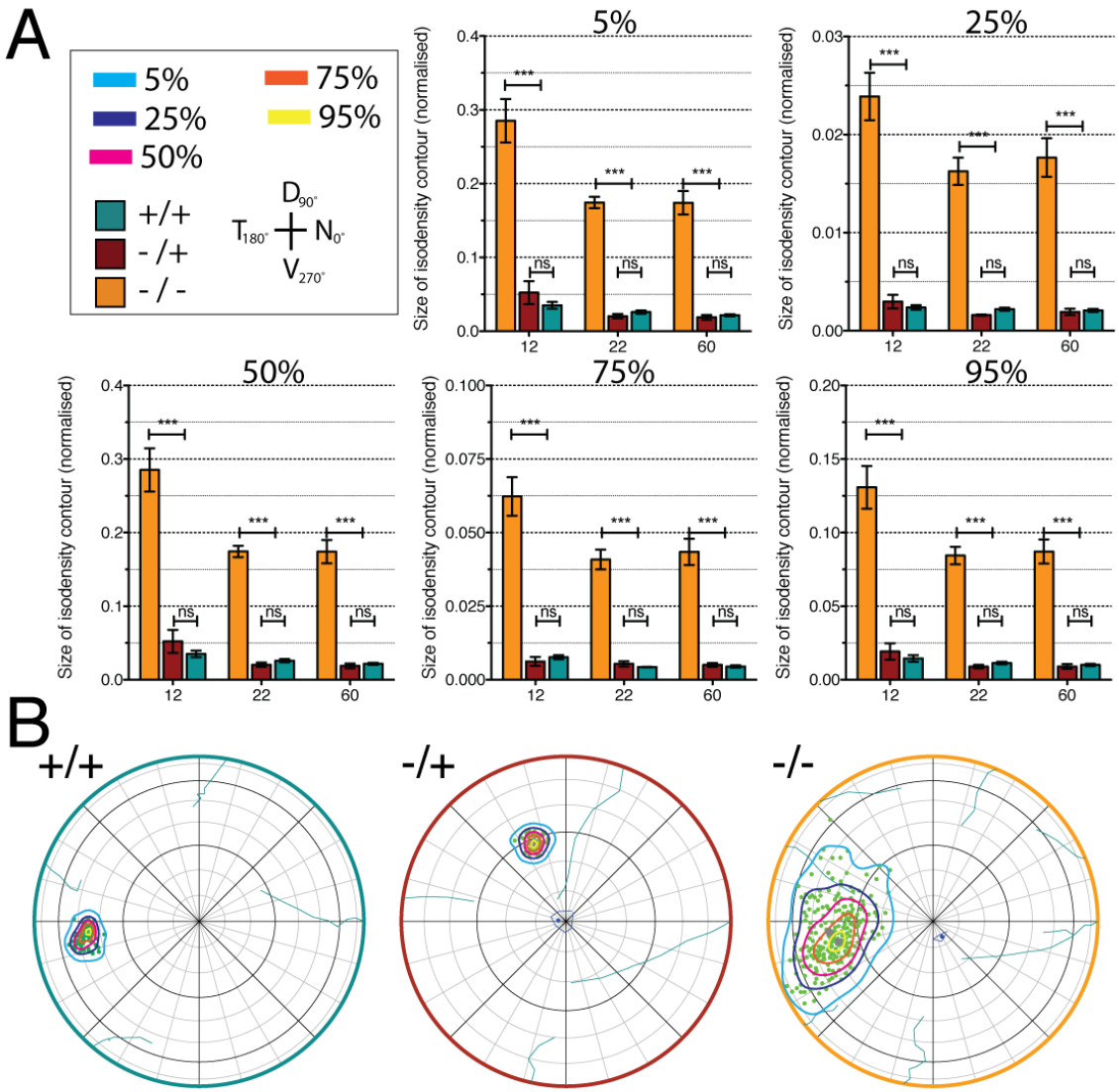

Figure 5-8 Comparing nAChR-β2 genotypes

The mean proportion of the retina covered by the 5%, 25%, 50%, 75% & 95% isodensity contours for injections done at P12, P22 and adult (P60+) for animals that are nAChR-β2 homozygotes (orange), heterozygotes (red) and wild-type (green). . Significance is determined with a two-tailed one-way ANOVA with a Bonferroni post-hoc test (*** p<0.0001; ** p<0.001; * p<0.05; ns= not significant)

Even though the nAChR-β2 strain has been back-crossed to a C57BL6/J background, I still wanted to check whether using wild type animals as a framework for comparison was reasonable. For this reason, the nearest neighbour plot for C57BL6/J mice (Figure 3-6J) was compared to the plots of nAChR-β2 -/- (Figure 5-6) and nAChR-β2 +/- & +/+

In Figure 5-9B it can clearly be seen from the plot that the function fitted to nAChR-β2 heterozygote and wild type littermates are the same as the C57BL6/J strain. This is both due to the almost complete overlap of the 95% confidence interval of the fit and the similar shape of the two curves. In contrast, the function fitted to nAChR-β2 homozygotes is significantly different from both of the above ($p<0.0001$, two-tailed F-test). This indicates that using the C57BL6/J strain as a framework for establishing the phenotype of the nAChR-β2 knockout strain is reasonable.

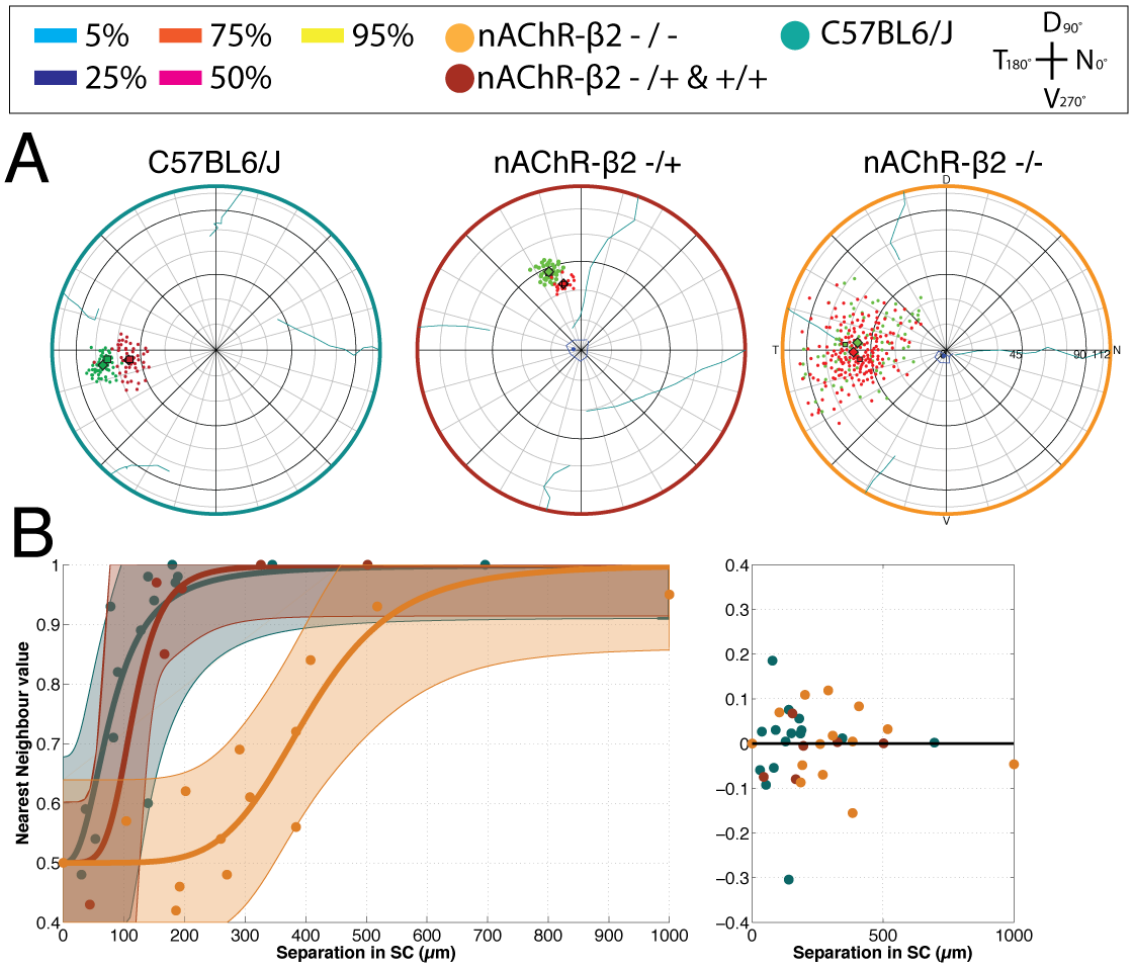

Figure 5-9 Comparing nAChR-β2 and C57BL6/J strains

A, Label resulting from single discrete injections of a comparable size into the anterior superior colliculus in adult (P60+) animals for C57BL6/J (green), nAChR-β2 +/- (brown) and -/- (orange). Isodensity contours are plotted by excluding 5% (light blue), 25% (dark blue), 50% (pink), 75% (orange) & 95% (yellow) of the cells with the lowest density using KD estimates. Plots are Azimuthal equal-area plots using a rim-angle of $\varphi_0 = 111.6^{\circ}$. Square is the peak density and diamond is the Karcher mean of the label. **B,** Segregation of the label measured by nearest neighbour analysis for C57BL6/J (green), nAChR-β2 +/- & +/+ (brown) and nAChR-β2 -/- (orange). NN value is plotted against separation of injection sites along the AP axis of the SC. The fits are logistic curves defined by Equation 2-13. The shaded area is the 95% confidence interval of the fits. The right-hand plot represents the residuals of the fits.

5.2.5 Neonatal topography in nAChR-β2 knockout animals

Since no apparent order is present in the neonatal (P0-4) animals, as measured by the nearest neighbour plots in Figure 5-7, the vector plots used to analyse the wild-type neonatal animals in Figure 4-11 have been repeated for the nAChR-β2 knockout animals to investigate whether there is any order observable in these animals. The plots are done by connecting the Karcher means or peak densities of the label from paired injections in the same animal with an arrow pointing toward the most anterior of the two injection sites. Using this method, it is possible to investigate whether we can predict the orientation of the label based purely from the orientation of the injection sites.

As can seen from the P0 vectors in Figure 5-10, it is generally possible to predict the orientations of both the Karcher means and the peak density locations from the orientation of the injection sites for injection pairs with large separations. However, it is no longer possible to confidently predict the length of the vectors from the separations of the injection sites, as can also be seen from the large difference in length between the Karcher mean and the peak density vectors for both P0 and P2. For close separations, it is not consistently possible to predict the orientation, as indicated by the shortest vector in the P0 plots pointing the correct way in the plots of the Karcher mean, but the wrong way in the plots of the peak densities. Incidentally, the injection sites resulting in this vector are separated by 516μm and therefore might be expected to be further apart. For P2, the length of the vectors still cannot be consistently predicted and it also appears that there is more scatter in the orientation of the vectors. However, to be able to conclude whether there are any differences between P0 and P2, more data would be needed.

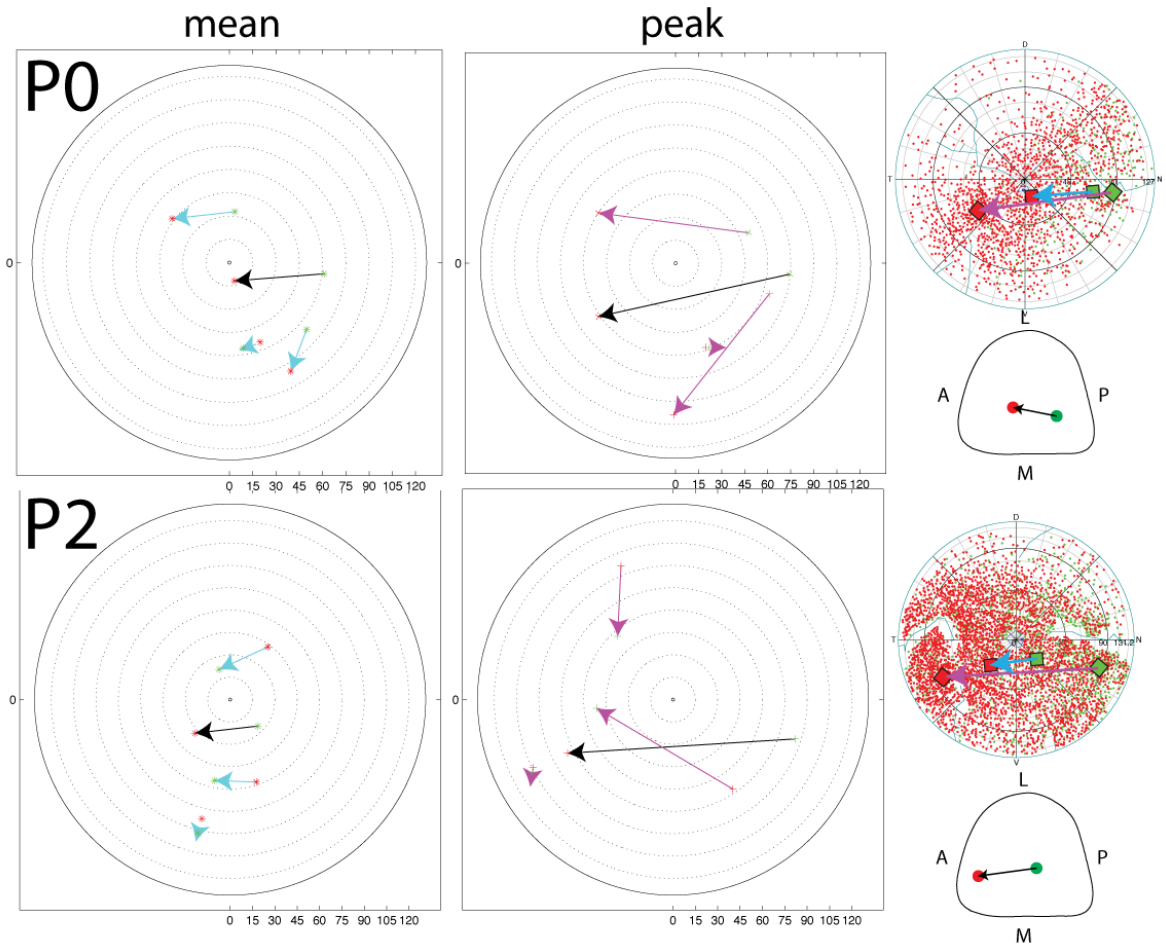

Figure 5-10 Vector analysis of neonatal nAChR-β2 -/- animals

Vectors connecting the Karcher means or Peak kernel density (KDE) of the label from two paired injections in the same animal for P0, & P2. The arrow is pointing towards the more anterior injection site. Plots are Azimuthal equidistant polar plots. The black arrow in the composite plots is the one in the example. In the example plots, the vector connecting the Karcher means is blue and the vector connecting the KDE peak densities is magenta. The locations of the respective SC injection sites are plotted underneath. The small *n* in these plots is due to not all the data having been analysed in this manner.

5.3 Discussion

To summarise the results, the experiments have revealed that discrete injections of tracer in nAChR-β2 knockout animals results in a significantly larger area of the retina containing labelled cells than in age-matched wild type animals from P8. However, with different distribution of label from birth, indicating a less precise projection from birth. Moreover, as a consequence of the less precise projections, less order was also observed along the AP axis for all ages. Moreover, in contrast to the wild type there is no refinement at all before P4. However, although the projection is less precise it is still possible to predict the location of the label from the injection sites at P0. Although the projection is less precise, a normal rate of refinement was observed from P8 to P22, indicating that the most severe effects of the knockout is in the first 8 days after birth.

Interestingly, nAChR-β2 -/- animals also exhibited an altered distribution of label, indicative of a less precise projection than wild type animals at P0. This difference probably reflects that the nAChR-dependent waves actually starts just before birth (Syed et al., 2004). The results therefore indicate that the waves may already have had an effect on the refinement of the projection at the time of birth.

After P4, there is a significant reduction in the size of the 5% contour level to 35.9±11.1% of the retina, indicating that there is a significant amount of refinement during this period. An interesting parallel to this timescale of the early refinement seen in this study is the varying patterns of stage 2 Acetylcholinergic spontaneous retinal activity at these time points. Between P0 and P3, the majority of the spontaneous events are isolated and waves are therefore infrequent and do not travel far (Hennig et al., 2009). Around P4, however, these spontaneous events start to become more correlated and bigger waves start propagating across the whole retina, persisting until around P8 (Bansal et al., 2000; Hennig et al., 2009) . It is therefore possible that the different modes of activity influence the different temporal patterns of refinement we see in the wild-type development in figure 4-2 and that this could account for the lack of refinement before P4 in the nAChR-β2 knockout animals. It is, moreover, likely that the

observed changes in the patterns of activity (Hennig et al., 2009) are due to homeostatic mechanisms that have been described as causing a restoration of gap-junction mediated activity by P4 when Acetylcholinergic activity is disrupted by removing choline acetyltransferase (ChAT), which is the sole enzyme synthesising Acetylcholine (Stacy et al., 2005).

The nAChR-β2 knock out animals clearly have a severe phenotype that is not recovered even in adulthood. It is therefore possible that there is a defined developmental time-window where specific patterns of activity are needed for forming a precise connection, and if these activity-patterns are disrupted, the projection never fully refines. The reason why such inferences can be made from the nAChR-β2 knock out is that it has been shown to only affect a defined period, which in the mouse is during the first postnatal week (from P0 to P7/8) (Bansal et al., 2000) after which normal activity is resumed since this is mediated by Glutamatergic activity in the bipolar cells (Wong et al., 2000). As a result of this normal activity not being able to rescue the phenotype, but merely resume the normal rate of refinement, it also offers up the possibility that the patterns of the Stage III Glutamatergic waves (Kerschensteiner and Wong, 2008) has different effects than that of the Stage II Cholinergic waves. This is also supported by the results in Figure 5-2, showing that after P8, there is only a significant refinement in the size of the 5% and 25% isodensity contours, but in the higher contour levels, above 50% density, there is no longer any significant differences in the later development. This is probably because these contour levels describe the focus of label, which is not recovered with the resumption of normal activity, due to the different spatiotemporal characteristics of Glutamatergic activity (Kerschensteiner and Wong, 2008). The later refinement of the broader projection of the wild type is also supported by data from individual RGC axonal arbours by Dhande et al. (2011), as they show that in the wild type, there is a significant increase in both length and complexity of the axonal arbours from P8 to P14, but no change in the area covered by the arbour. Interestingly, for the nAChR-β2 knockout animals, they report a significant increase in arbour length and size for individual axons accompanied by a decrease in the complexity, which appears

to be contradictory to our data showing that there is a decrease in the size of the 5% isodensity contour, but not in the 50% isodensity contour.

The refinement between P8 and P12 in the nAChR-β2 -/- mice is probably be due to the onset of stage 3 Glutamatergic activity and a restoration of normal activity (Bansal et al., 2000; Sernagor et al., 2000; Zhou and Zhao, 2000). Although it would be interesting if the transition in waves could compensate for the developmental defects and rescue them, dependent on whether the absolute or the ratio of refinement between P8 and P12 was compared, it could be argued that it is either rescue or that it is merely resumption of normal development. A way to get a handle on this question would be to manipulate the Glutamatergic waves, e.g. by removing the vesicular Glutamate transporter-1 (vGlut-1), which is necessary for the Glutamatergic waves (Blankenship et al., 2009). However, this manipulation also causes the period of Cholinergic waves to be extended (Blankenship et al., 2009), which may cause other phenotypes.

Another factor in the debate of the later refinement of the projection is whether visual experience plays a role in further sculpting the projection, or whether such evoked activity merely aids in maintaining the projection (Carrasco et al., 2005). It is likely that the activity has some effects on the alignment of the cortical input to the SC as changes in this connectivity are occurring around the time of eye opening at P13 (Phillips et al., 2011; Triplett et al., 2012). Whether it has any direct effects on the retinocollicular projection, however, remains to be established. A way of addressing this question would be to inhibit or remove visual cortex and thereby eliminate this activity and see whether it has any effects on the refinement.

One potentially confounding factor on the nAChR-β2 -/- is that it is a global knockout, and therefore could potentially have local effects in the SC. However, since it has been possible to rescue the phenotype in the contralateral projection by a retinal-specific knock-in of the nAChR-β2 subunit (Xu et al., 2011), which restores the same spatial, but not temporal properties of the waves. This caused a rescue of the monocular, but not

binocular projection, suggesting that the specific spatial patterns of activity are very important for achieving correct wiring within the contralateral projection.

Regarding the anisotropy of the label in the nAChR-β2 knockout animals that can be seen in Figure 5-1, such differences in the distribution of label for the axes has been reported along the AP axis of the SC (Chandrasekaran et al., 2005; Mrsic-Flogel et al., 2005), as well as in dLGN (Grubb et al., 2003) and V1 (Cang et al., 2005). It has, moreover, been demonstrated that one of the major effects on the wave-characteristics when removing nAChR-β2 is that the waves no longer have a preference for NT axis (Stafford et al., 2009), which could explain this phenotype. For this reason, it would be interesting to do this analysis for the present dataset. An additional factor related to the anisotropy, which would be interesting to investigate in more depth is whether the expansion in anterior SC and compression in posterior SC is also reflected in the anatomy. The problem with this is the difficulty of making injections in the posterior medial SC, as discussed earlier, which is also why nothing can be concluded about this from the present dataset. When looking at the injections, which are mostly in the anterior half of the SC, there is, however, a trend towards the more anterior injections being slightly larger in adult animals.

Both molecular and activity-based cues have been clearly shown to influence and direct the development of anatomical and functional retinotopic maps. Nevertheless, it has remained controversial whether activity is required for the read-out of molecular gradients. Recently, however, there is emerging evidence for the requirement of activity in topographic mapping (Hanson and Landmesser, 2004; Nicol et al., 2007). To support this, our data from the nAChR-β2-/- mice show that the structured activity is crucial for the large-scale refinement. It may also be that the structured activity is involved in the read-out and maintenance of the ephrin gradients and Eph counter gradients (Kastanenka and Landmesser, 2010) that are established around E15 and persist throughout development in wild-type mice (Rashid et al., 2005; Marler et al., 2008).

Chapter 6 General Discussion

This thesis deals with the development of anatomical precision in the retinocollicular projection, a topic that has been the subject of study for the past 50 years since the mechanisms of chemoaffinity for guidance of axons from the frog retina to the optic tectum was first proposed by Sperry (1963). However, although numerous studies have addressed the question, as described in the introduction, few have provided detailed quantitative data on the development of the contralateral retinocollicular projection.

Here we have provided a framework in the form of a thorough quantitative description of the developmental sequence (Chapter 4), and in doing so have confirmed and quantified many of the previous observations of different phases of development while using new metrics of order to provide some new preliminary evidence pointing toward a role for plasticity concurrent with later developmental critical periods of cortical plasticity. Moreover, by providing a thorough examination of the changes in this framework associated with changes in activity (Chapter 5), we hope to better understand the relation between activity-based and molecular guidance cues in map formation by providing quantitative data for computational models.

6.1 Development of retinocollicular precision and the role of activity: wild type

It is interesting to speculate about what causes the different phases of development observed in Chapter 4. The refinement starts with an initial slow decrease in the size of the spread of the label (Figure 4-2) caused mainly by restriction of label along the NT axis from P0 to P4 (Figure 4-1). This is then followed by a rapid change in the spread of the projection between P4-6 and a change in the size of the focus from P6 to P8 (Figure 4-2).

Interestingly, these timings correspond to the timings of changes in the frequency of the waves reported by Sun et al (2008a). They found that the wave frequency at P1-3 was between 1.5-2 waves per minute, whereas they found that the frequency at P5-8 was between 0.4-0.7 waves per minute with the shift occurring around P4. It has, moreover, earlier been suggested that the early (P0-P4) spontaneous activity may be influenced by gap junction-mediated activity and as a result may exhibit different characteristics than the later waves after P4 (Stacy et al., 2005). Similar changes in wave frequency have also been observed in the turtle (Sernagor et al., 2003; Hennig et al., 2011) and was ascribed to the shift from excitatory to inhibitory $GABA_A$ signalling. It is, however, worth noting that the results by Sun et al. (2008a) have been questioned in Stafford et al. (2009) due to the medium used previously having been shown to affect spiking rates. Stafford et al. found that the wave frequency in P6 wild type retinae at 37˚C was 1.6 waves per minute. However, although the spiking rates may have had an effect on the absolute value, it is probable at the difference in wave frequency between P0-3 and P5-8 found by Sun et al (2008a) is real.

Consequently, we can say that the frequent waves are coincident with the slow early refinement observed in the retrograde labelling experiments therefore might be involved in the refinement of large projection errors. In contrast, since the later less frequent waves are coincident with the tightening of the focus, we can therefore speculate that they may be involved in stabilising branches.

6.2 Development of retinocollicular precision and the role of activity: nAChR-β2

The experiments in Chapter 5 have revealed that discrete injections of tracer in nAChR-β2 knockout animals result in a significantly different distribution of retinal label from birth, indicating a less precise projection from birth. Moreover, due the a lack of refinement in the first 4 postnatal days, injections done at P8 in nAChR-β2 knockout animals result in a larger area of the retina containing labelled cells than in age-matched wild type animals from P8. However, although the projection is less precise it is still possible to predict the location of the label from the injection sites at P0, indicating that topographically appropriate branching may still be present. Although the projection is less precise in early development, a normal rate of refinement was observed from P4 to P8, indicating that the most severe effects of the knockout is in the first 4 days after birth.

An interesting observation is that in the nAChR-β2 knockout animals at birth, the 5% isodensity contour is larger than the wild type, indicating that the projection is less defined, which one might speculate is due to more non-specific branching. However, the amount of retina containing labelled cells is smaller in the knockout and the 5% of cells with the lowest density therefore occupy a smaller area. Such a distribution could indicate that although the changes in activity pattern causes there to be more non-specific branching, these branches might be shorter than the wild type. However, whether the changes in activity associated with the lack of cholinergic activity could cause such a phenotype is unclear and this therefore remains speculative.

If we consider the data from the retrograde transport in the nAChR-β2 knockout animals, where we see that before P4, there is no refinement in the isodensity contours (Figure 5-3) or in the nearest neighbour analysis (Figure 5-5). It is apparent that the most severe effects of the knockout is in disrupting the early waves before P4, as it appears from both the isodensity contour analysis and the nearest neighbour analysis like normal levels of refinement is resumed after P4.

Looking at the nAChR-β2 knockout mice, there is a similar discrepancy as in the wild type data between recordings of waves from different research groups. The frequency of the waves have been reported as 2.7 waves/min at P4 by Sun et al (2008b) and 0.8 waves/min at P6 by Stafford et al. (2009). This discrepancy (increase of wave frequency by Sun et al. and decrease in waves by Stafford et al.) could be down to the difference in age of the animals, but since Sun et al. only looked at P4, while Stafford et al. only looked at P6, this remains to be resolved. It is, however, a distinct possibility that such a change in waves could account for some of the phenotype observed in the retrograde tracing experiments.

The elongated retinocollicular receptive fields along the AP axis that have been reported in the nAChR-β2 knockout (Chandrasekaran et al., 2005) and the elongation of RGC axonal arbours along this axis (Dhande et al., 2011), suggest that the effect of activity-dependent refinement could be stronger along the AP axis, a theory also supported by the preference of the waves for the NT retinal axis (Stafford et al., 2009). An observation that is supported by evidence showing that specific oscillations in RGC cAMP levels is permissive for ephrinA5-mediated repulsion along the SC AP axis (Nicol et al., 2007). Moreover, since the levels of cAMP has been shown to be involved in establishing and strengthening synapses (Munno et al., 2003), it is possible that such changes in cAMP levels could further affect the stability of synapses, which consequently may affect the refinement of the projection.

One theory regarding the activity-dependent refinement argues that the refinement of topography is facilitated by mechanisms that are LTP-like in nature, which implies that RGCs initially contact and form synapses on all target cells, and then the active synapses are selectively strengthened through the recruitment of further synaptic machinery and enlargement of the active dense zone, whereas inactive synapses are weakened and eventually disappear (Willshaw and Malsburg, 1976; Cline, 2001; Chandrasekaran et al., 2007; Hooks and Chen, 2007; Shah and Crair, 2008b). The implications of these LTP-like mechanisms is that the axonal arbour is reduced in size

to form only the most relevant connections, resulting in a more refined map than had been obtainable with the exclusive involvement of molecular gradients. Moreover, the characteristics of the cholinergic waves fit the paradigms needed for these mechanisms (Butts, 2002).

When used in combination with axon-axon competition (Gosse et al., 2008; Triplett et al., 2011) such roles of activity provides a strong model for retinotopic map refinement. For these reasons, it would be interesting to examine the relative differences in synapse-density on RGC axons between anterior and posterior SC in wild type and nAChR-β2 knockout animals to see whether the changes observed in the projection as a consequence of altered activity patterns may be caused by changes in synapse density.

If it is the case that the axes are offset from the midline throughout development, it may explain some of the increased scatter in the nearest neighbour data for large separations (See Figures 4-4 and 4-5). An increase in scatter is what would be expected if projections were offset from the midline while injections are aligned with the midline since there is a distinct AP anisotropy in early development in both wild type and nAChR-β2 -/- animals.

A final surprising element of the wild type data revealed by the nearest neighbour data is the difference between P22 and adult in the wild type animals for the AP axis (Figure 4-7D). This subtle difference might be caused by synaptic remodelling as is the case in dLGN during this period (Hooks and Chen, 2008). It is noticeable that this effect spans the critical period for ocular dominance plasticity around P28 (Gordon and Stryker, 1996) which is also reflected in large-scale changes in the anatomical connectivity (Antonini et al., 1999). Interestingly, this phenotype is less pronounced in the nAChR-β2 knockout strain, which could reflect that the changes in fine topography are masked by the gross imprecisions in this strain along the AP axis. For this reason it may be interesting to see if there is a difference in the nearest neighbour order between P22 and adult animals along the ML axis in the nAChR-β2 strain.

6.3 Modelling development

One of the initial aims of this thesis was to provide a quantitative description of the spatiotemporal development of the retinocollicular projection to enable the creation of a modelling environment that was informed and constrained by data. This resulted in a collaboration with Johannes Hjorth, Stephen Eglen (both University of Cambridge) David Sterratt and David Willshaw (University of Edinburgh) to create a model capable of simulating the developing wild type dataset incorporating all the known aspects of molecular and activity-dependent guidance and refinement.

The idea is to create a model that predicts the wild type data, in which we could then manipulate the factors influencing the formation of the map and thereby start to tease apart the mechanisms. The resultant model will be based on an existing model by Triplett *et al.* (2011), the basic premises of which are illustrated in Figure 6-1 (A & B). Briefly, a random RGC and a random unconnected SC neuron are selected, then for every iteration of the model the probability of making a new connection is calculated and the connection is either made or not. This probability is determined by the matching of the molecular cues of the cells, how correlated their activity is and by adding in a factor controlling the competition between RGC axons (Figure 6-1A). Likewise, for strengthening or weakening (and possible removal) of connections the probability is calculated for all existing connections with each iteration of the model and the connections are strengthened or weakened accordingly (Figure 6-1B). The model is based on the probabilistic sorting principles according to Eph/ephrin gradients and counter gradients (Tsigankov and Koulakov, 2006), but rather than treating connections as binary, it employs weakening and strengthening of connections by addition of synapses akin to Willshaw *et al*. (2006). The model, moreover, also uses more recent data from *in vitro* multi-electrode array recordings of the characteristics of the spontaneous waves in the first week from Stafford et al. (2009) to define the activity-correlation between RGCs for both wild-type and nAChR-beta2 knockout animals.

The aim is that modifying this model to incorporate the latest knowledge of Eph/ephrin interactions and activity-patterns through development, will eventually enable us to

simulate the retrobeads injections throughout development. An example of such a simulated experiment using the existing model is shown in Figure 6-1C, where the label resulting from a pair of injections is simulated. Iterations shown represent stages where the distribution of label resembles the label that would be obtained experimentally, such that the label at 100 iterations might resemble P0, 500 iterations might resemble P2, 1000 iterations resembles P4 and 2000 iterations resembles P8. This, however, is merely an estimate and will need more analysis to determine and verify how the iterations of the model relate temporally to the actual development.

As can be seen in Figure 6-1D, although the label from the simulations qualitatively resembles the experimental label at defined stages, quantitatively, this is not the case. The model therefore still needs fine-tuning to match the timings of the experimental data. However, even if the timings were matched, the shape of the curve still does not quite reflect the shape of the curve for the observed data indicating that the model doesn't account for the different phases of refinement observed experimentally (in Chapter 4). The model shows a rapid refinement early in development, which is not reflected in the experimental P0 and P2 data. This might suggests that the mechanisms in the model more closely resemble that of the refinement from P4 onwards, as the initial refinement is more similar to the observed refinement after P4.

The reason for this apparent disparity could arise from the fact that the correlation data for the RGCs used in the model is from recordings in P6 retinae from Stafford et al (2009). Considering the earlier discussion about the differences in frequency between the early and later waves, this would explain why the model has an initial rapid refinement in the simulations that is not seen in experimental data. It is therefore possible that the model actually only simulates the later stages of the nAChR-dependent refinement after P6

The other obvious discrepancy between the data from the simulations which is especially apparent if comparing the simulated data to the experimental data from the spread of all the label in the experiments, as this shows an initial spread covering 98%

of the retina, whereas the label in the model starts out covering just 52% of the retina. The main reason for this is that in the model the ML extent of axon arbours are limited to 25% of the extent of the SC and therefore will never label the entire retina. This constraint was implemented to maintain the initial ML order from Plas et al. (2005) and to replicate the order in the nearest neighbour analysis of the ML data (Figure 4-10). However, considering the ability of axons to extend and stabilise branches across half the ML extent of the SC (Hindges et al., 2002), this may need to be revisited. It just so happens that the initial spread of the projection in the model is approximately the same as the P6 experimental data (Figure 6-1D). These observations could suggest that a two-component model would be better for describing development.

Interestingly, the model as is accurately predicts the wild-type order in the adult using the nearest neighbour analysis for the AP axis (Figure 6-1E).

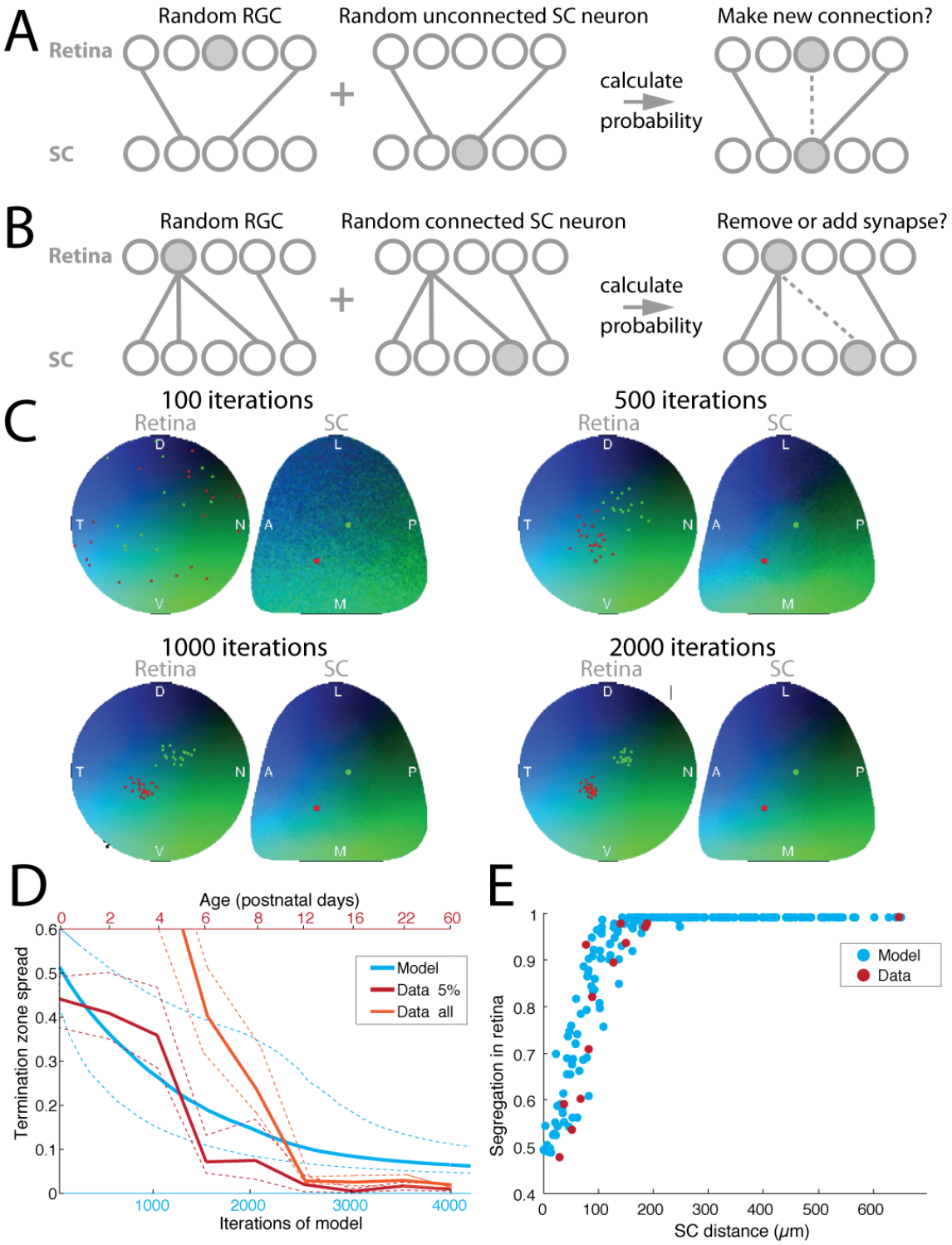

Figure 6-1 Comparison of Data to Theoretical Model

Figure 6-1 Legend: Comparison of Data to Theoretical Model (previous page)

A, Framework of model. If a random SC neuron is paired with a random RGC, the probability of a new connection being made is determined by the differences in chemical guidance cues and activity correlations between the two neurons. **B,** Similarly, for existing connections a balance of guidance molecules and correlated activity determines the probability of strengthening, weakening or ultimately removing a connection by addition or removal of synapses onto the same neuron. **C,** Examples of retinal label resulting from simulated injections into the SC at four different stages of the simulation. The smoothness of the blue-green gradient in the SC represents the order in the map. **D,** Nearest neighbour analysis of data from end-point of model simulation (blue) and P60+ data from Figure 3-6J (red). **E,** Spread of label of simulations of model (blue) and data from the 5% isodensity contour sizes (red). Lines represent the median and error is the interquartile range.

Taking the modelling one step further, we find that by purely changing the correlation index of the cells in the retina according to the observations by Stafford et al. (2009) (Figure 6-2A), there is a phenotype of reduced precision in the more mature animals for the spread of the termination zone (Figure 6-2B), which analogous to the isodensity contour analysis, and less order in the projection for the nearest neighbour data throughout development (Figure 6-2C). Having said that, the model still does not emulate the distribution of label in the experimental data, neither for the isodensity contour analysis (cf. Figure 5-3) nor for the nearest neighbour data (cf. Figure 5-7).

This could again be due to the correlation indices used not accurately representing the early waves due to the discrepancies between the observations of Sun et al. (2008a) and Stafford et al. (2009), causing the phenotype in the model to be less severe than the one observed in the data (cf. Figure 5-4).

To summarise, the creation of a realistic modelling environment of precision in collicular retinotopic development would require a better handle on the effects of specific activity-patterns in axon guidance and refinement. Such information could come either from a consistent examination of the changes in nAChR-dependent spontaneous activity during the first postnatal week and the precise effects of the nAChR-β2 mutant during this week as well. Moreover, the examination of how different patterns of activity affects the development either by examining different mutants, e.g. the nAChR-α3 knockout (Bansal et al., 2000), or by manipulating activity, e.g. by using Channelrhodopsin-2 to manipulate activity in the retina and subsequently examine the effects on mapping (Zhang et al., 2011). Additionally, it is apparent that it is crucial to establish a better understanding of the role of Eph/ephrin reverse signalling on the branching and refinement of axonal arbours and the role of patterned activity in these mechanisms. However, in the lack of such a mechanistic understanding, detailed frameworks of normal and altered development, such as the one presented here, provide a powerful method for attempting to elucidate these mechanisms.

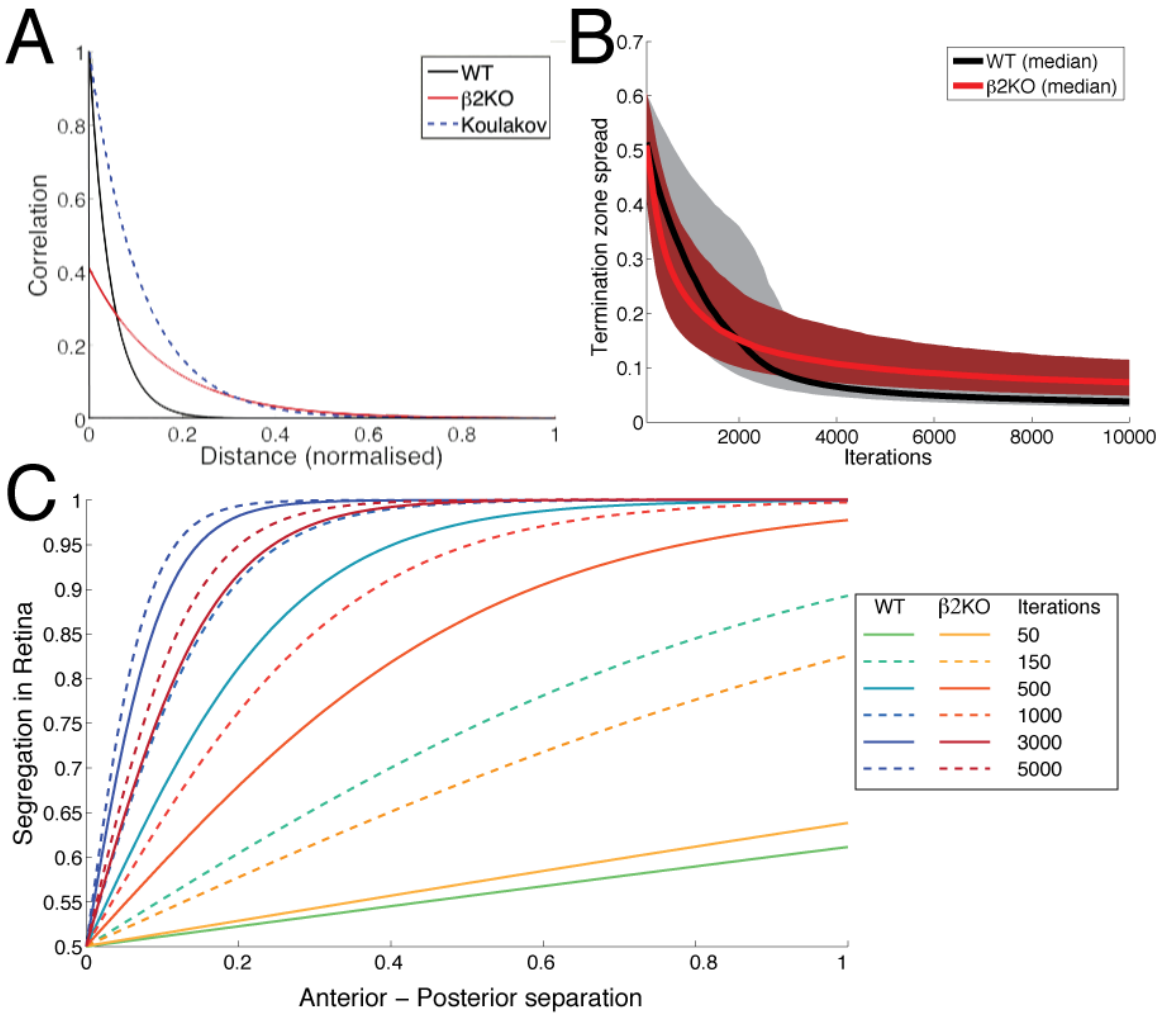

Figure 6-2 Modelling the effects of the nAChR-β2 knockout

A, the correlation of the spontaneous activity in wild type (black) and nAChR-β2 knockout (red) from Stafford et al. (2009) and those used by Koulakov (Tsigankov and Koulakov, 2006) (blue, dashed curve) plotted as a function of distance. **B,** the size of the termination zone as a function of time (iterations of the model) for wild type (black) and nAChR-β2 -/- animals (red) using the model detailed in Figure 4-11 and with the correlation indices in A. Shaded grey area is the 95% confidence interval for the wild type and dashed red line is the same for the nAChR-β2 knockout. Note that the function fitted here is not the same as the one used in the analysis of the data. This is a sigmoid function of the form:

$$Y = \frac{1}{1 + e^{-x/\kappa}}$$

6.4 Future Directions

What has been lacking in the field are ways of reliably and systematically manipulating both the levels and spatiotemporal properties of activity in the early developing visual system. If followed up by careful examination both anatomically and physiologically, such methodology could provide vital in improving our understanding of the underlying mechanisms of *in vivo* axon guidance and refinement

One approach for elucidating the relative contributions of activity in development is the use of optogenetic methods to manipulate activity in neurons (Boyden et al., 2005). Combined with the ability to image activity in specific cell types (Borghuis et al., 2011) or even cell compartments (Mao et al., 2008), this offers the possibility to start mapping the development of neural connectivity in projections such as the retinocollicular projection. Although such techniques have been used extensively in studying the fish and frog tectum, they have hardly been employed in studying the development of the mouse retinocollicular projection. One of the few studies starting to address questions regarding the activity-dependent formation of retinocollicular projection is looking at the development of eye segregation in the SC by using Channelrhodopsin-2 in RGCs to manipulate activity and thereby elucidate the effects on the projection by imaging activity in the SC (Zhang et al., 2011). Moreover, the ability to label cells genetically and the appearance of more reliable activity markers in many different colours (Zhao et al., 2011) will enable the study of both inputs to and outputs of circuits.

An outstanding issue is the precise mechanisms by which the spontaneous correlated activity facilitates refinement in the SC and other retino-recipient areas. Initial steps into investigating this question in the rodent has been made by Ackman *et al.* (2012). By labelling RGCs with Calcium-sensitive dye, they determined the nature of the waveform activity patterns in the axon arbours and compared these to separate movies of this activity in collicular cells. By doing this they show that the activity in vivo are in agreement with previous data measured in retinal in vitro preparations (Stafford et al., 2009). A further elaboration to this line of investigation could be to label both the RGC axon arbours and the Collicular cells with Calcium dyes of different wavelengths (e.g.

R-GECO and G-GECO) (Zhao et al., 2011). Such data could give an indication of the exact nature of the waves and would enable us to address another key unanswered question of understanding the role of Hebbian plasticity in the establishment of precise connectivity and whether this changes with age.

A separate question is precisely which patterns of activity facilitate the development of map formation and consequently, whether it is possible to disrupt the wild-type map or rescue e.g. the nAChR-β2 -/- map phenotype by synchronising separate cell-types or retinal areas, respectively. Using such a paradigm it would, moreover, also be possible to address the question of the role of competition by selectively silencing or activating subsets of RGCs to see if this gives them respectively a competitive disadvantage or advantage.

Bibliography

Ackman JB, Burbridge TJ, Crair MC (2012) Retinal waves coordinate patterned activity throughout the developing visual system. Nature 490:219–225.

Akerman CJ, Smyth D, Thompson ID (2002) Visual experience before eye-opening and the development of the retinogeniculate pathway. Neuron 36:869–879.

Antonini A, Fagiolini M, Stryker MP (1999) Anatomical correlates of functional plasticity in mouse visual cortex. J Neurosci 19:4388–4406.

Applebury MLM, Antoch MPM, Baxter LCL, Chun LLL, Falk JDJ, Farhangfar FF, Kage KK, Krzystolik MGM, Lyass LAL, Robbins JTJ (2000) The murine cone photoreceptor: a single cone type expresses both S and M opsins with retinal spatial patterning. Neuron 27:513–523.

Badea TC, Nathans J (2004) Quantitative analysis of neuronal morphologies in the mouse retina visualized by using a genetically directed reporter. J Comp Neurol 480:331–351.

Bansal A, Singer JH, Hwang BJ, Xu W, Beaudet A, Feller MB (2000) Mice lacking specific nicotinic acetylcholine receptor subunits exhibit dramatically altered spontaneous activity patterns and reveal a limited role for retinal waves in forming ON and OFF circuits in the inner retina. J Neurosci 20:7672–7681.

Birgbauer E, Cowan CA, Sretavan DW, Henkemeyer M (2000) Kinase independent function of EphB receptors in retinal axon pathfinding to the optic disc from dorsal but not ventral retina. Development 127:1231–1241.

Birgbauer E, Oster SF, Severin CG, Sretavan DW (2001) Retinal axon growth cones respond to EphB extracellular domains as inhibitory axon guidance cues. Development.

Bishop PO, Kozak WW, Vakkur GJ (1962) Some quantitative aspects of the cat's eye: axis and plane of reference, visual field co-ordinates and optics. J Physiol 163:466–502.

Blankenship AG, Ford KJ, Johnson J, Seal RP, Edwards RH, Copenhagen DR, Feller MB (2009) Synaptic and extrasynaptic factors governing glutamatergic retinal waves. Neuron 62:230–241.

Blankenship AG, Hamby AM, Firl A, Vyas S, Maxeiner S, Willecke K, Feller MB (2011) The role of neuronal connexins 36 and 45 in shaping spontaneous firing patterns in the developing retina. J Neurosci 31:9998–10008.

Bonhoeffer F, Huf J (1982) In vitro experiments on axon guidance demonstrating an anterior-posterior gradient on the tectum. EMBO J 1:427–431.

Borghuis BG, Tian L, Xu Y, Nikonov SS, Vardi N, Zemelman BV, Looger LL (2011) Imaging Light Responses of Targeted Neuron Populations in the Rodent Retina. J Neurosci 31:2855–2867.

Boyden ES, Zhang F, Bamberg E, Nagel G, Deisseroth K (2005) Millisecond-timescale, genetically targeted optical control of neural activity. Nat Neurosci 8:1263–1268.

Brown A, Yates PA, Burrola P, Ortuño D, Vaidya A, Jessell TM, Pfaff SL, O'Leary DDM, Lemke G (2000) Topographic mapping from the retina to the midbrain is controlled by relative but not absolute levels of EphA receptor signaling. Cell 102:77–88.

Bunt SM, Lund RD, Land PW (1983) Prenatal development of the optic projection in albino and hooded rats. Brain Res 282:149–168.

Butts DA (2002) Retinal waves: implications for synaptic learning rules during development. Neuroscientist 8:243–253.

Butts DA, Kanold PO, Shatz CJ (2007) A burst-based "Hebbian" learning rule at retinogeniculate synapses links retinal waves to activity-dependent refinement. PLoS Biol 5:e61.

Cancedda L, Putignano E, Sale A, Viegi A, Berardi N, Maffei L (2004) Acceleration of visual system development by environmental enrichment. J Neurosci 24:4840–4848.

Cang J, Niell CM, Liu X, Pfeiffenberger C, Feldheim DA, Stryker MP (2008a) Selective disruption of one Cartesian axis of cortical maps and receptive fields by deficiency in ephrin-As and structured activity. Neuron 57:511–523.

Cang J, Rentería RC, Kaneko M, Liu X, Copenhagen DR, Stryker MP (2005) Development of precise maps in visual cortex requires patterned spontaneous activity in the retina. Neuron 48:797–809.

Cang J, Wang L, Stryker MP, Feldheim DA (2008b) Roles of ephrin-as and structured activity in the development of functional maps in the superior colliculus. J Neurosci 28:11015–11023.

Carrasco MM, Razak KA, Pallas SL (2005) Visual experience is necessary for maintenance but not development of receptive fields in superior colliculus. J Neurophysiol 94:1962–1970.

Carvalho RF, Beutler M, Marler KJM, Knöll B, Becker-Barroso E, Heintzmann R, Ng T, Drescher U (2006) Silencing of EphA3 through a cis interaction with ephrinA5. Nat Neurosci 9:322–330.

Cepko CL, Austin CP, Yang X, Alexiades M, Ezzeddine D (1996) Cell fate determination in the vertebrate retina. Proc Natl Acad Sci 93:589–595.

Chan SO, Guillery RW (1994) Changes in fiber order in the optic nerve and tract of rat embryos. J Comp Neurol 344:20–32.

Chandrasekaran AR, Plas DT, Gonzalez E, Crair MC (2005) Evidence for an instructive role of retinal activity in retinotopic map refinement in the superior colliculus of the mouse. J Neurosci 25:6929–6938.

Chandrasekaran AR, Shah RD, Crair MC (2007) Developmental homeostasis of mouse retinocollicular synapses. J Neurosci 27:1746–1755.

Chen S, Li W (2012) A color-coding amacrine cell may provide a blue-Off signal in a mammalian retina. Nat Neurosci 15:954–956.

Cheng HJ, Nakamoto M, Bergemann AD, Flanagan JG (1995) Complementary gradients in expression and binding of ELF-1 and Mek4 in development of the topographic retinotectal projection map. Cell 82:371–381.

Cline HT (2001) Dendritic arbor development and synaptogenesis. Curr Opin Neurobiol 11:118–126.

Coleman JE, Law K, Bear MF (2009) Anatomical origins of ocular dominance in mouse primary visual cortex. Neuroscience 161:561–571.

Colonnese MT, Constantine-Paton M (2001) Chronic NMDA receptor blockade from birth increases the sprouting capacity of ipsilateral retinocollicular axons without disrupting their early segregation. J Neurosci 21:1557–1568.

Colonnese MT, Constantine-Paton M (2006) Developmental period for N-methyl-D-aspartate (NMDA) receptor-dependent synapse elimination correlated with visuotopic map refinement. J Comp Neurol 494:738–751.

Colonnese MT, Kaminska A, Minlebaev M, Milh M, Bloem B, Lescure S, Moriette G, Chiron C, Ben-Ari Y, Khazipov R (2010) A conserved switch in sensory processing prepares developing neocortex for vision. Neuron 67:480–498.

Cook JE, Becker DL (2009) Gap-junction proteins in retinal development: new roles for the "nexus". Physiology 24:219–230.

Coombs J, van der List D, Wang G-Y, Chalupa LM (2006) Morphological properties of mouse retinal ganglion cells. Neuroscience 140:123–136.

Cowan WM, Fawcett J, O'Leary DDM, Stanfield B (1984) Regressive Events in Neurogenesis. Science 225:1258–1265.

Dalva MB, Takasu MA, Lin MZ, Shamah SM, Hu L, Gale NW, Greenberg ME (2000) EphB receptors interact with NMDA receptors and regulate excitatory synapse formation. Cell 103:945–956.

Davy A, Gale NW, Murray EW, Klinghoffer RA, Soriano P, Feuerstein C, Robbins SM (1999) Compartmentalized signaling by GPI-anchored ephrin-A5 requires the Fyn tyrosine kinase to regulate cellular adhesion. Genes Dev 13:3125–3135.

Dean PP, Redgrave PP, Westby GWG (1989) Event or emergency? Two response systems in the mammalian superior colliculus. Trends Neurosci 12:137–147.

Debski EA, Cline HT (2002) Activity-dependent mapping in the retinotectal projection. Curr Opin Neurobiol 12:93–99.

Demas J, Eglen SJ, Wong ROL (2003) Developmental loss of synchronous spontaneous activity in the mouse retina is independent of visual experience. J Neurosci 23:2851–2860.

Dhande OS, Hua EW, Guh E, Yeh J, Bhatt S, Zhang Y, Ruthazer ES, Feller MB, Crair MC (2011) Development of single retinofugal axon arbors in normal and β2 knock-out mice. J Neurosci 31:3384–3399.

Dorris MC, Paré M, Munoz DP (1997) Neuronal activity in monkey superior colliculus related to the initiation of saccadic eye movements. J Neurosci 17:8566–8579.

Dräger UC (1975) Receptive fields of single cells and topography in mouse visual cortex. J Comp Neurol 160:269–290.

Dräger UC (1978) Observations on monocular deprivation in mice. J Neurophysiol 41:28–42.

Dräger UC (1985) Birth dates of retinal ganglion cells giving rise to the crossed and uncrossed optic projections in the mouse. Proc R Soc Lond 224:57–77.

Dräger UC, Hubel DH (1975) Responses to visual stimulation and relationship between visual, auditory, and somatosensory inputs in mouse superior colliculus. J Neurophysiol 38:690–713.

Dräger UC, Hubel DH (1976) Topography of visual and somatosensory projections to mouse superior colliculus. J Neurophysiol 39:91–101.

Dräger UCU, Olsen JFJ (1980) Origins of crossed and uncrossed retinal projections in pigmented and albino mice. J Comp Neurol 191:383–412.

Drescher U, Kremoser C, Handwerker C, Löschinger J, Noda M, Bonhoeffer F (1995) In vitro guidance of retinal ganglion cell axons by RAGS, a 25 kDa tectal protein related to ligands for Eph receptor tyrosine kinases. Cell 82:359–370.

Dudanova II, Kao T-JT, Herrmann JEJ, Zheng BB, Kania AA, Klein RR (2012) Genetic evidence for a contribution of EphA:ephrinA reverse signaling to motor axon guidance. J Neurosci 32:5209–5215.

Ecker JL, Dumitrescu ON, Wong KY, Alam NM, Chen S-K, LeGates T, Renna JM, Prusky GT, Berson DM, Hattar S (2010) Melanopsin-expressing retinal ganglion-cell photoreceptors: cellular diversity and role in pattern vision. Neuron 67:49–60.

Edwards SB, Ginsburgh CL, Henkel CK, Stein BE (1979) Sources of subcortical projections to the superior colliculus in the cat. J Comp Neurol 184:309–329.

Elstrott J, Feller MB (2009) Vision and the establishment of direction-selectivity: a tale of two circuits. Curr Opin Neurobiol 19:293–297.

Fagiolini M, Hensch TK (2000) Inhibitory threshold for critical-period activation in primary visual cortex. Nature 404:183–186.

Farah MH, Easter SS (2005) Cell birth and death in the mouse retinal ganglion cell layer. J Comp Neurol 489:120–134.

Foster DH, Bischof WF (1987) Bootstrap variance estimators for the parameters of small-sample sensory-performance functions. Biol Cybern 57:341–347.

Foster DH, Bischof WF (1997) Bootstrap estimates of the statistical accuracy of thresholds obtained from psychometric functions. Spat Vis 11:135–139.

Fredj N, Hammond S, Otsuna H, Chien C-B, Burrone J, Meyer MP (2010) Synaptic Activity and Activity-Dependent Competition Regulates Axon Arbor Maturation, Growth Arrest, and Territory in the Retinotectal Projection. J Neurosci 30:10939–10951.

Frisen J, Yates PA, McLaughlin T, Friedman GC, O'Leary DDM, Barbacid M (1998) Ephrin-A5 (AL-1/RAGS) Is Essential for Proper Retinal Axon Guidance and Topographic Mapping in the Mammalian Visual System. Neuron 20:235–243.

Galli L, Maffei L (1988) Spontaneous impulse activity of rat retinal ganglion cells in prenatal life. Science 242:90–91.

Galli-Resta L, Ensini M, Fusco E, Gravina A, Margheritti B (1993) Afferent spontaneous electrical activity promotes the survival of target cells in the developing retinotectal system of the rat. J Neurosci 13:243–250.

Gandhi NJ, Katnani HA (2011) Motor Functions of the Superior Colliculus. Annu Rev Neurosci 34:205–231.

Gandhi SP, Yanagawa Y, Stryker MP (2008) Delayed plasticity of inhibitory neurons in developing visual cortex. Proc Natl Acad Sci 105:16797–16802.

Godement P, Salaün J, Imbert M (1984) Prenatal and postnatal development of retinogeniculate and retinocollicular projections in the mouse. J Comp Neurol 230:552–575.

Gordon JA, Stryker MP (1996) Experience-dependent plasticity of binocular responses in the primary visual cortex of the mouse. J Neurosci 16:3274–3286.

Gosse NJ, Nevin LM, Baier H (2008) Retinotopic order in the absence of axon competition. Nature 452:892–895.

Grinvald A, Lieke E, Frostig RD, Gilbert CD, Wiesel TN (1986) Functional architecture of cortex revealed by optical imaging of intrinsic signals. Nature 324:361–364.

Grubb MS, Rossi FM, Changeux J-P, Thompson ID (2003) Abnormal functional organization in the dorsal lateral geniculate nucleus of mice lacking the beta 2 subunit of the nicotinic acetylcholine receptor. Neuron 40:1161–1172.

Grubb MS, Thompson ID (2004) Visual response properties in the dorsal lateral geniculate nucleus of mice lacking the beta2 subunit of the nicotinic acetylcholine receptor. J Neurosci 24:8459–8469.

Hanson MG, Landmesser LT (2004) Normal patterns of spontaneous activity are required for correct motor axon guidance and the expression of specific guidance molecules. Neuron 43:687–701.

Harris WA (1980) The effects of eliminating impulse activity on the development of the retinotectal projection in salamanders. J Comp Neurol 194:303–317.

Haverkamp S, Wassle H, Duebel J, Kuner T, Augustine G, Feng G, Euler T (2005) The Primordial, Blue-Cone Color System of the Mouse Retina. J Neurosci 25:5438.

Hebb DO (1949) The organization of behavior: A neuropsychological approach. New York: John Wiley & Sons.

Henkemeyer M, Itkis OS, Ngo M, Hickmott PW, Ethell IM (2003) Multiple EphB receptor tyrosine kinases shape dendritic spines in the hippocampus. J Cell Biol 163:1313–1326.

Hennig MH, Adams C, Willshaw D, Sernagor E (2009) Early-stage waves in the retinal network emerge close to a critical state transition between local and global functional connectivity. J Neurosci 29:1077–1086.

Hennig MH, Grady J, van Coppenhagen J, Sernagor E (2011) Age-dependent Homeostatic Plasticity of GABAergic Signaling in Developing Retinal Networks. J Neurosci 31:12159–12164.

Hensch TK, Fagiolini M, Mataga N, Stryker MP, Baekkeskov S, Kash SF (1998) Local GABA circuit control of experience-dependent plasticity in developing visual cortex. Science 282:1504–1508.

Hess DT (1987) A retinal whole-mount method useful in detecting retrogradely-labeled ganglion cells. Vision Res 18:581–584.

Hindges R, McLaughlin T, Genoud N, Henkemeyer M, O'Leary DDM (2002) EphB forward signaling controls directional branch extension and arborization required for dorsal-ventral retinotopic mapping. Neuron 35:475–487.

Hofbauer A, Dräger UC (1985) Depth segregation of retinal ganglion cells projecting to mouse superior colliculus. J Comp Neurol 234:465–474.

Hofer SB, Ko H, Pichler B, Vogelstein J, Ros H, Zeng H, Lein E, Lesica NA, Mrsic-Flogel TD (2011) Differential connectivity and response dynamics of excitatory and inhibitory neurons in visual cortex. Nat Neurosci 14:1045–1052.

Holash JAJ, Soans CC, Chong LDL, Shao HH, Dixit VMV, Pasquale EBE (1997) Reciprocal Expression of the Eph Receptor Cek5 and Its Ligand(s) in the Early Retina. Dev Biol 182:14–14.

Holt CE, Harris WA (1983) Order in the initial retinotectal map in Xenopus: a new technique for labelling growing nerve fibres. Nature 301:150–152.

Hong YK, Kim I-J, Sanes JR (2011) Stereotyped axonal arbors of retinal ganglion cell subsets in the mouse superior colliculus. J Comp Neurol 519:1691–1711.

Hooks BM, Chen C (2007) Critical periods in the visual system: changing views for a model of experience-dependent plasticity. Neuron 56:312–326.

Hooks BM, Chen C (2008) Vision triggers an experience-dependent sensitive period at the retinogeniculate synapse. J Neurosci 28:4807–4817.

Hornberger MR, Dütting D, Ciossek T, Yamada T, Handwerker C, Lang S, Weth F, Huf J, Wessel R, Logan C, Tanaka H, Drescher U (1999) Modulation of EphA receptor function by coexpressed ephrinA ligands on retinal ganglion cell axons. Neuron 22:731–742.

Hu EH, Pan F, Völgyi B, Bloomfield SA (2010) Light increases the gap junctional coupling of retinal ganglion cells. J Physiol 588:4145–4163.

Hubel DH, Wiesel TN (1963) Shape and arrangement of columns in cat's striate cortex. J Physiol 165:559–568.

Huberman AD, Feller MB, Chapman B (2008a) Mechanisms underlying development of visual maps and receptive fields. Annu Rev Neurosci 31:479–509.

Huberman AD, Manu M, Koch SM, Susman MW, Lutz A, Ullian EM, Baccus SA, Barres BA (2008b) Architecture and Activity-Mediated Refinement of Axonal Projections from a Mosaic of Genetically Identified Retinal Ganglion Cells. Neuron 59:425–438.

Huberman AD, Wei W, Elstrott J, Stafford B, Feller MB, Barres BA (2009) Genetic identification of an On-Off direction-selective retinal ganglion cell subtype reveals

a layer-specific subcortical map of posterior motion. Neuron 62:327–334.

Hughes A (1971) Topographical relationships between the anatomy and physiology of the rabbit visual system. Doc Ophthalmol 30:33–159.

Ikeda T, Hikosaka O (2003) Reward-dependent gain and bias of visual responses in primate superior colliculus. Neuron 39:693–700.

Jhaveri S, Edwards MA, Schneider GE (1991) Initial stages of retinofugal axon development in the hamster: evidence for two distinct modes of growth. Exp Brain Res 87:371–382.

Kao T-J, Kania A (2011) Ephrin-mediated cis-attenuation of Eph receptor signaling is essential for spinal motor axon guidance. Neuron 71:76–91.

Kastanenka K, Landmesser LT (2010) In Vivo Activation of Channelrhodopsin-2 Reveals That Normal Patterns of Spontaneous Activity Are Required for Motoneuron Guidance and Maintenance of Guidance Molecules. J Neurosci 30:10575–10585.

Katz LC, Burkhalter A, Dreyer WJ (1984) Fluorescent latex microspheres as a retrograde neuronal marker for in vivo and in vitro studies of visual cortex. Nature 310:498–500.

Katz LC, Iarovici DM (1990) Green fluorescent latex microspheres: a new retrograde tracer. Neuroscience 34:511–520.

Kayser MS, Nolt MJ, Dalva MB (2008) EphB receptors couple dendritic filopodia motility to synapse formation. Neuron 59:56–69.

Kerr JND, Denk W (2008) Imaging in vivo: watching the brain in action. Nat Rev Neurosci 9:195–205.

Kerr JND, Greenberg D, Helmchen F (2005) Imaging input and output of neocortical networks in vivo. Proc Natl Acad Sci 102:14063–14068.

Kerschensteiner D, Wong ROL (2008) A precisely timed asynchronous pattern of ON and OFF retinal ganglion cell activity during propagation of retinal waves. Neuron 58:851–858.

Kim I-J, Zhang Y, Meister M, Sanes JR (2010) Laminar restriction of retinal ganglion cell dendrites and axons: subtype-specific developmental patterns revealed with transgenic markers. J Neurosci 30:1452–1462.

Klein R (2009) Bidirectional modulation of synaptic functions by Eph/ephrin signaling. Nat Neurosci 12:15–20.

Kullander K, Klein R (2002) Mechanisms and functions of Eph and ephrin signalling.

Nat Rev Mol Cell Biol 3:475–486.

Levelt CN, Hübener M (2012) Critical-period plasticity in the visual cortex. Annu Rev Neurosci 35:309–330.

Liets LC, Olshausen BA, Wang G-Y, Chalupa LM (2003) Spontaneous activity of morphologically identified ganglion cells in the developing ferret retina. J Neurosci 23:7343–7350.

Lim BK, Cho S-J, Sumbre G, Poo M-M (2010) Region-specific contribution of ephrin-B and Wnt signaling to receptive field plasticity in developing optic tectum. Neuron 65:899–911.

Lim BK, Matsuda N, Poo M-M (2008a) Ephrin-B reverse signaling promotes structural and functional synaptic maturation in vivo. Nat Neurosci 11:160–169.

Lim Y-S, McLaughlin T, Sung T-C, Santiago A, Lee K-F, O'Leary DDM (2008b) p75(NTR) mediates ephrin-A reverse signaling required for axon repulsion and mapping. Neuron 59:746–758.

Lo L, Anderson DJ (2011) A Cre-Dependent, Anterograde Transsynaptic Viral Tracer for Mapping Output Pathways of Genetically Marked Neurons. Vision Res 72:938–950.

Lovejoy LP, Krauzlis RJ (2010) Inactivation of primate superior colliculus impairs covert selection of signals for perceptual judgments. Nat Neurosci 13:261–266.

Lu W, Constantine-Paton M (2004) Eye opening rapidly induces synaptic potentiation and refinement. Neuron 43:237–249.

Ma YT, Hsieh T, Forbes ME, Johnson JE, Frost DO (1998) BDNF injected into the superior colliculus reduces developmental retinal ganglion cell death. J Neurosci 18:2097–2107.

Maffei L, Galli-Resta L (1990) Correlation in the discharges of neighboring rat retinal ganglion cells during prenatal life. Proc Natl Acad Sci 87:2861–2864.

Mann F, Ray S, Harris W, Holt CE (2002) Topographic Mapping in Dorsoventral Axis of the Xenopus Retinotectal System Depends on Signaling through Ephrin-B Ligands. Neuron 35:13–13.

Mao T, O'Connor DH, Scheuss V, Nakai J, Svoboda K (2008) Characterization and subcellular targeting of GCaMP-type genetically-encoded calcium indicators. PLoS ONE 3:e1796.

Marcus RC, Gale NW, Morrison ME, Mason CA, Yancopoulos GD (1996) Eph family receptors and their ligands distribute in opposing gradients in the developing mouse retina. Dev Biol 180:786–789.

Marler KJM, Becker-Barroso E, Martínez A, Llovera M, Wentzel C, Poopalasundaram S, Hindges R, Soriano E, Comella JX, Drescher U (2008) A TrkB/EphrinA Interaction Controls Retinal Axon Branching and Synaptogenesis. J Neurosci 28:12700–12712.

Marler KJM, Poopalasundaram S, Broom ER, Wentzel C, Drescher U (2010) Pro-neurotrophins secreted from retinal ganglion cell axons are necessary for ephrinA-p75NTR-mediated axon guidance. Neural Dev 5:30.

Marquardt TT, Shirasaki RR, Ghosh SS, Andrews SES, Carter NN, Hunter TT, Pfaff SLS (2005) Coexpressed EphA Receptors and Ephrin-A Ligands Mediate Opposing Actions on Growth Cone Navigation from Distinct Membrane Domains. Cell 121:13–13.

McLaughlin T, Hindges R, Yates PA, O'Leary DDM (2003a) Bifunctional action of ephrin-B1 as a repellent and attractant to control bidirectional branch extension in dorsal-ventral retinotopic mapping. Development 130:2407–2418.

McLaughlin T, Torborg CL, Feller MB, O'Leary DDM (2003b) Retinotopic map refinement requires spontaneous retinal waves during a brief critical period of development. Neuron 40:1147–1160.

Meister M, Wong ROL, Baylor D, Shatz CJ (1991) Synchronous Bursts of Action Potentials in Ganglion Cells of the Developing Mammalian Retina. Science 252:939–943.

Morgan JL, Schubert T, Wong RO (2008) Developmental patterning of glutamatergic synapses onto retinal ganglion cells. Neural Dev 3:8.

Mrsic-Flogel TD, Hofer SBS, Creutzfeldt CC, Cloëz-Tayarani II, Changeux J-PJ, Bonhoeffer TT, Hübener MM (2005) Altered map of visual space in the superior colliculus of mice lacking early retinal waves. J Neurosci 25:6921–6928.

Mrsic-Flogel TD, Hofer SBS, Ohki KK, Reid RCR, Bonhoeffer TT, Hübener MM (2007) Homeostatic regulation of eye-specific responses in visual cortex during ocular dominance plasticity. Neuron 54:961–972.

Munno DW, Prince DJ, Syed NI (2003) Synapse number and synaptic efficacy are regulated by presynaptic cAMP and protein kinase A. J Neurosci 23:4146–4155.

Müller JR, Philiastides MG, Newsome WT (2005) Microstimulation of the superior colliculus focuses attention without moving the eyes. Proc Natl Acad Sci 102:524–529

Nakagawa SS, Brennan CC, Johnson KGK, Shewan DD, Harris WAW, Holt CEC (2000) Ephrin-B Regulates the Ipsilateral Routing of Retinal Axons at the Optic Chiasm. Neuron 25:12–12.

Nakamura H, O'Leary DDM (1989) Inaccuracies in initial growth and arborization of chick retinotectal axons followed by course corrections and axon remodeling to develop topographic order. J Neurosci 9:3776–3795.

Nicol X, Voyatzis S, Muzerelle A, Narboux-Nême N, Südhof TC, Miles R, Gaspar P (2007) cAMP oscillations and retinal activity are permissive for ephrin signaling during the establishment of the retinotopic map. Nat Neurosci 10:340–347.

O'Leary DD, Fawcett JW, Cowan WM (1986) Topographic targeting errors in the retinocollicular projection and their elimination by selective ganglion cell death. J Neurosci 6:3692–3705.

Oommen BS, Stahl JS (2008) Eye orientation during static tilts and its relationship to spontaneous head pitch in the laboratory mouse. Brain Res 1193:57–66.

Perry VH, Henderson Z, Linden R (1983) Postnatal changes in retinal ganglion cell and optic axon populations in the pigmented rat. J Comp Neurol 219:356–368.

Phillips MA, Colonnese MT, Goldberg J, Lewis LD, Brown EN, Constantine-Paton M (2011) A Synaptic Strategy for Consolidation of Convergent Visuotopic Maps. Neuron 71:710–724.

Picciotto MR, Zoli M, Léna C, Bessis A, Lallemand Y, LeNovère N, Vincent P, Pich EM, Brulet P, Changeux J-P (1995) Abnormal avoidance learning in mice lacking functional high-affinity nicotine receptor in the brain. Nature 374:65–67.

Plas DT, Lopez JE, Crair MC (2005) Pre-target sorting of retino-collicular axons in the mouse. J Comp Neurol 491:305–319.

Rashid T, Upton AL, Blentic A, Ciossek T, Knöll B, Thompson ID, Drescher U (2005) Opposing gradients of ephrin-As and EphA7 in the superior colliculus are essential for topographic mapping in the mammalian visual system. Neuron 47:57–69.

Remtulla S, Hallett PE (1985) A schematic eye for the mouse, and comparisons with the rat. Vision Res 25:21–31.

Rice DSD, Williams RWR, Goldowitz DD (1995) Genetic control of retinal projections in inbred strains of albino mice. J Comp Neurol 354:459–469.

Rodieck RW (1979) Visual Pathways. Annu Rev Neurosci 2:193–225.

Rubin CM, van der List DA, Ballesteros JM, Goloshchapov AV, Chalupa LM, Chapman B (2011) Mouse mutants for the nicotinic acetylcholine receptor ß2 subunit display changes in cell adhesion and neurodegeneration response genes. PLoS ONE 6:e18626.

Sakurai T, Wong E, Drescher U, Tanaka H, Jay DG (2002) Ephrin-A5 restricts topographically specific arborization in the chick retinotectal projection in vivo.

Proc Natl Acad Sci 99:10795–10800.

Scanziani M, Häusser M (2009) Electrophysiology in the age of light. Nature 461:930–939.

Schmucker C, Schaeffel F (2004) A paraxial schematic eye model for the growing C57BL/6 mouse. Vision Res 44:1857–1867.

Sernagor E, Eglen SJ, O'Donovan MJ (2000) Differential effects of acetylcholine and glutamate blockade on the spatiotemporal dynamics of retinal waves. J Neurosci 20:RC56.

Sernagor E, Eglen SJ, Wong ROL (2001) Development of retinal ganglion cell structure and function. Prog Ret Eye Res 20:139–174.

Sernagor E, Young C, Eglen SJ (2003) Developmental modulation of retinal wave dynamics: shedding light on the GABA saga. J Neurosci 23:7621–7629.

Shah RD, Crair MC (2008a) Retinocollicular synapse maturation and plasticity are regulated by correlated retinal waves. J Neurosci 28:292–303.

Shah RD, Crair MC (2008b) Mechanisms of response homeostasis during retinocollicular map formation. J Physiol 586:4363–4369.

Shatz CJ, Stryker MP (1978) Ocular dominance in layer IV of the cat's visual cortex and the effects of monocular deprivation. J Physiol 281:267–283.

Shatz CJ, Stryker MP (1988) Prenatal tetrodotoxin infusion blocks segregation of retinogeniculate afferents. Science 242:87–89.

Sher A, DeVries SH (2012) A non-canonical pathway for mammalian blue-green color vision. Nat Neurosci 15:952–953.

Simon DK, O'Leary DDM (1992) Development of topographic order in the mammalian retinocollicular projection. J Neurosci 12:1212–1232.

Smith SL, Häusser M (2010) Parallel processing of visual space by neighboring neurons in mouse visual cortex. Nat Neurosci 13:1144–1149.

Song S, Miller KD, Abbott LF (2000) Competitive Hebbian learning through spike-timing-dependent synaptic plasticity. Nat Neurosci 3:919–926.

Sperry RW (1943) Optic nerve regeneration with return of vision in anurans. J Neurophysiol 7:57–69.

Sperry RW (1963) Chemoaffinity in the orderly growth of nerve fiber patterns and connections. Proc Natl Acad Sci 50:703–710.

Sretavan DW, Shatz CJ, Stryker MP (1988) Modification of retinal ganglion cell axon morphology by prenatal infusion of tetrodotoxin. Nature 336:468–471.

Stacy RC, Demas J, Burgess RW, Sanes JR, Wong ROL (2005) Disruption and recovery of patterned retinal activity in the absence of acetylcholine. J Neurosci 25:9347–9357.

Stafford B, Sher A, Litke AM, Feldheim DA (2009) Spatial-temporal patterns of retinal waves underlying activity-dependent refinement of retinofugal projections. Neuron 64:200–212.

Sterratt DC, Lyngholm D, Willshaw D, Thompson ID (n.d.) Standard anatomical and visual space for the mouse retina: computational reconstruction and transformation of flattened retinae with the Retistruct package. PLoS Comput Biol. *Submitted*.

Stone J (1981) The Whole Mount Handbook: A Guide to the Preparation and analysis of retinal whole mounts. Sydney: Maitland Publications.

Stryker MP, Harris WA (1986) Binocular impulse blockade prevents the formation of ocular dominance columns in cat visual cortex. J Neurosci 6:2117–2133.

Stuermer CA (1988) Retinotopic organization of the developing retinotectal projection in the zebrafish embryo. J Neurosci 8:4513–4530.

Sun C, Speer C, Wang G-Y, Chapman B, Chalupa LM (2008a) Epibatidine application in vitro blocks retinal waves without silencing all retinal ganglion cell action potentials in developing retina of the mouse and ferret. J Neurophysiol.

Sun C, Warland D, Ballesteros J, van der List D, Chalupa LM (2008b) Retinal waves in mice lacking the {beta}2 subunit of the nicotinic acetylcholine receptor. Proc Natl Acad Sci 105:13638–13643.

Suzuki S, Numakawa T, Shimazu K, Koshimizu H, Hara T, Hatanaka H, Mei L, Lu B, Kojima M (2004) BDNF-induced recruitment of TrkB receptor into neuronal lipid rafts: roles in synaptic modulation. J Cell Biol 167:1205–1215.

Syed MM, Lee S, Zheng J, Zhou ZJ (2004) Stage-dependent dynamics and modulation of spontaneous waves in the developing rabbit retina. J Physiol 560:533–549.

Szél AA, Csorba GG, Caffé ARA, Szél GG, Röhlich PP, Van Veen TT (1994) Different patterns of retinal cone topography in two genera of rodents, Mus and Apodemus. Cell Tissue Res 276:143–150.

Szél AA, Röhlich PP, Caffé ARA, Juliusson BB, Aguirre GG, Van Veen TT (1992) Unique topographic separation of two spectral classes of cones in the mouse retina. J Comp Neurol 325:327–342.

Thompson ID, Holt CE (1989) Effects of intraocular tetrodotoxin on the development

of the retinocollicular pathway in the Syrian hamster. J Comp Neurol 282:371–388.

Thong IG, Dreher B (1986) The development of the corticotectal pathway in the albino rat. Vision Res 25:227–238.

Triplett JW, Pfeiffenberger C, Yamada J, Stafford BK, Sweeney NT, Litke AM, Sher A, Koulakov AA, Feldheim DA (2011) Competition is a driving force in topographic mapping. Proc Natl Acad Sci 108:19060–19065.

Triplett JW, Phan A, Yamada J, Feldheim DA (2012) Alignment of multimodal sensory input in the superior colliculus through a gradient-matching mechanism. Journal of Neuroscience 32:5264–5271.

Tsigankov DN, Koulakov AA (2006) A unifying model for activity-dependent and activity-independent mechanisms predicts complete structure of topographic maps in ephrin-A deficient mice. J Comput Neurosci 21:101–114.

Upton AL, Cordery PM, Thompson ID (2007) Emergence of topography in the developing hamster retinocollicular projection: axial differences and the role of cell death. Eur J Neurosci 25:2319–2328.

Van Essen DC (1979) Visual Areas of the Mammalian Cerebral Cortex. Annu Rev Neurosci 2:227–261.

Vanderhaeghen P, Cheng H-J (2010) Guidance molecules in axon pruning and cell death. Cold Spring Harb Perspect Biol 2:a001859.

Völgyi B, Abrams J, Paul DL, Bloomfield SA (2005) Morphology and tracer coupling pattern of alpha ganglion cells in the mouse retina. J Comp Neurol 492:66–77.

Völgyi B, Chheda S, Bloomfield SA (2009) Tracer coupling patterns of the ganglion cell subtypes in the mouse retina. J Comp Neurol 512:664–687.

Wang B-S, Sarnaik R, Cang J (2010a) Critical Period Plasticity Matches Binocular Orientation Preference in the Visual Cortex. Neuron 65:246–256.

Wang L, Sarnaik R, Rangarajan K, Liu X, Cang J (2010b) Visual Receptive Field Properties of Neurons in the Superficial Superior Colliculus of the Mouse. J Neurosci 30:16573.

Weisstein EW (2012a) Azimuthal Equidistant Projection. MathWorld--A Wolfram Web Resource Available at: http://mathworld.wolfram.com/AzimuthalEquidistantProjection.html [Accessed July 20, 2012a].

Weisstein EW (2012b) Lambert Azimuthal Equal-Area Projection. MathWorld--A Wolfram Web Resource Available at: http://mathworld.wolfram.com/LambertAzimuthalEqual-AreaProjection.html

[Accessed July 20, 2012b].

Weisstein EW (2012c) Orthographic Projection Weisstein EW, ed. MathWorld--A Wolfram Web Resource Available at: http://mathworld.wolfram.com/OrthographicProjection.html [Accessed July 20, 2012c].

Weisstein EW (2012d) Sinusoidal Projection. MathWorld--A Wolfram Web Resource Available at: http://mathworld.wolfram.com/SinusoidalProjection.html [Accessed July 20, 2012d].

Weisstein EW (2012e) Logistic Equation. MathWorld--A Wolfram Web Resource Available at: http://mathworld.wolfram.com/LogisticEquation.html [Accessed July 15, 2012e].

Wiesel TN, Hubel DH (1963) Effects of visual deprivation on morphology and physiology of cells in the cats lateral geniculate body. J Neurophysiol 26:978–993.

Wilks TA, Rodger J, Harvey AR (2010) A role for ephrin-As in maintaining topographic organization in register across interconnected central visual pathways. Eur J Neurosci 31:613–622.

Willshaw D (2006) Analysis of mouse EphA knockins and knockouts suggests that retinal axons programme target cells to form ordered retinotopic maps. Development 133:2705–2717.

Willshaw DJ, Malsburg CVD (1976) How Patterned Neural Connections Can Be Set Up by Self-Organization. Proc R Soc Lond 194:431–445.

Wong ROL, Chernjavsky A, Smith SJ, Shatz CJ (1995) Early functional neural networks in the developing retina. Nature 374:716–718.

Wong ROL, Ghosh A (2002) Activity-dependent regulation of dendritic growth and patterning. Nat Rev Neurosci 3:803–812.

Wong WT, Myhr KL, Miller ED, Wong ROL (2000) Developmental changes in the neurotransmitter regulation of correlated spontaneous retinal activity. J Neurosci 20:351–360.

Wu G, Malinow R, Cline HT (1996) Maturation of a central glutamatergic synapse. Science (New York, NY) 274:972–976.

Xu H-P, Furman M, Mineur YS, Chen H, King SL, Zenisek D, Zhou ZJ, Butts DA, Tian N, Picciotto MR, Crair MC (2011) An Instructive Role for Patterned Spontaneous Retinal Activity in Mouse Visual Map Development. Neuron 70:1115–1127.

Yang QH, Snyder JP, Tobler WR (1999) Map Projection Transformation. London:

Taylor & Francis.

Yates PA, Roskies AL, McLaughlin T, O'Leary DDM (2001) Topographic-specific axon branching controlled by ephrin-As is the critical event in retinotectal map development. J Neurosci 21:8548–8563.

Yoo S, Kim Y, Noh H, Lee H, Park E, Park S (2011) Endocytosis of EphA receptors is essential for the proper development of the retinocollicular topographic map. EMBO J. 30(8):1593-607

Yoshii A, Constantine-Paton M (2007) BDNF induces transport of PSD-95 to dendrites through PI3K-AKT signaling after NMDA receptor activation. Nat Neurosci 10:702–711.

Yoshii A, Sheng MH, Constantine-Paton M (2003) Eye opening induces a rapid dendritic localization of PSD-95 in central visual neurons. Proc Natl Acad Sci 100:1334–1339.

Zénon A, Krauzlis RJ (2012) Attention deficits without cortical neuronal deficits. Nature 489:434–437.

Zhang J, Ackman JB, Xu H-P, Crair MC (2011) Visual map development depends on the temporal pattern of binocular activity in mice. Nat Neurosci.

Zhang LI, Tao HW, Holt CE, Harris WA, Poo M (1998) A critical window for cooperation and competition among developing retinotectal synapses. Nature 395:37–44.

Zhang Y, Kim I-J, Sanes JR, Meister M (2012) The most numerous ganglion cell type of the mouse retina is a selective feature detector. Proc Natl Acad Sci 109:E2391–E2398.

Zhao Y, Araki S, Wu J, Teramoto T, Chang YF, Nakano M, Abdelfattah AS, Fujiwara M, Ishihara T, Nagai T, Campbell RE (2011) An Expanded Palette of Genetically Encoded Ca2+ Indicators. Science 333:1888–1891.

Zhou ZJ, Zhao D (2000) Coordinated transitions in neurotransmitter systems for the initiation and propagation of spontaneous retinal waves. J Neurosci 20:6570–6577.